Summer 2021

Multiple generations of phlogopite in an alnöite diatreme: Insights into the petrogenesis of the Avon Alkaline Igneous Province, Missouri

Nathan Gregory Limbaugh

Department:

MULTIPLE GENERATIONS OF PHLOGOPITE IN AN ALNÖITE DIATREME: INSIGHTS INTO THE PETROGENESIS OF THE AVON ALKALINE IGNEOUS PROVINCE, MISSOURI

by

NATHAN GREGORY LIMBAUGH

A THESIS

Presented to the Graduate Faculty of the

MISSOURI UNIVERSITY OF SCIENCE AND TECHNOLOGY

In Partial Fulfillment of the Requirements for the Degree

MASTER OF SCIENCE

in

GEOLOGY AND GEOPHYSICS

2021

Approved by:

Dr. John P. Hogan, Advisor
Dr. Willis E. Hames
Dr. David J. Wronkiewicz
Dr. David M. Borrok

PUBLICATION THESIS OPTION

This thesis consists of the following article, formatted in the style used by the Missouri University of Science and Technology:

Paper I, found on pages 6 – 57, is intended for submission to LITHOS.

ABSTRACT

Alkaline Ultramafic Carbonatite (AUC) complexes, although rare, are valued for diamonds and REEs, and as windows into subcontinental and mantle processes as recorded by rock fabrics, mineral spatial relationships, and mineral compositions. We report specifically on olivine and phlogopite petrographic relationships and compositions from the Devonian alnöite diatreme-facies of the Avon Alkaline Igneous Province, Missouri. The diatreme alnöite is a mixture of domains of olivine magmaclasts (OM) set in a crystal-rich melilite matrix. OM are highly fractured, serpentinized olivine pseudomorphs with variable amounts of pristine olivine fragments. Larger olivine domains typically exhibit clear crystal faces and irregular "channels" indicative of a skeletal morphology due to rapid growth. Islands of unaltered olivine are homogeneous, Mg-rich ($Fo_{86.9}$-$Fo_{89.9}$) and exhibit variation in trace element (e.g., Ni, Cr, Co, Ti, P) abundances consistent with limited fractional crystallization and origin from a metasomatized fertile peridotite partial melt. Three textural varieties of phlogopite are recognized. Tabular, euhedral phlogopite (phl-Ia) crystals occur along the margins of OM and within the melilite matrix. Small (mm-size) euhedral to subhedral phlogopite (phl-Ib) phenocrysts occur inside the "channels" of skeletal olivine. Phlogopite (phl-II) crystals occur as anhedral, oxide-rich, palmate porphyroblast clusters, rimming serpentinized olivine and scattered throughout the matrix. These phlogopite populations are geochemically distinct, showing ion substitution enrichments (i.e. Ba, Al, Ti). These mineral and geochemical relationships enable the development of a comprehensive petrogenetic model of the Avon Alkaline Igneous Province AUC diatreme complex.

ACKNOWLEDGEMENTS

I would like to thank my advisor, Dr. John P. Hogan, for his dedicated mentorship and guidance throughout my research endeavors. He is responsible for equipping me with the necessary and fundamental skills required to leap into the unknown with unbridled curiosity. Additionally, Dr. Hogan helped forge and refine my passion for igneous petrology, geochemistry, and scientific writing throughout the course of this project. In addition, I would like to thank Dr. Willis E. Hames, especially for his role in collecting microprobe data which elevated the significance of our findings, and Dr. David J. Wronkiewicz for taking the time to serve on my thesis committee and review my work, in addition to contributions regarding the application and education of geochemistry throughout my academia. I would also like to thank my mother, Jessica, for supporting my academic endeavors and for enduring endless conversations about igneous petrology and geochemistry. I would especially like to dedicate an honorary tribute to my father, Greg, who passed away during the composition of my master's thesis, who guided me through my youth and inspired me to pursue a career in geology from our many adventures through the Colorado Rockies. Lastly, I would like to thank my brothers of Delta Sigma Phi fraternity, Delta Epsilon chapter, here at the Missouri University of Science and Technology for helping me strive to become a better man in all ways, including the dedication to the geosciences, and for lending good company throughout my graduate studies. Your continued support propelled me to ever convince the world of the sincerity of our purpose and to push the boundaries of scientific understanding for the betterment of all lives.

TABLE OF CONTENTS

LIST OF ILLUSTRATIONS

SECTION Page

LIST OF TABLES

PAPER I Page

1. INTRODUCTION

Diatremes and maars have been of longstanding and increasing interest within the geoscience community. Additionally, the growing economic demand for rare earth elements (REEs) and diamonds associated with kimberlitic diatremes, has sparked further curiosity in unraveling the origin of diatreme formation. Studying diatreme petrographic mineral textures and geochemical characteristics can further scientific understanding of mantle magmatic evolution processes involved in diatreme petrogenesis within igneous complexes.

Diatremes are subterranean pipes that fed shallower magmatic eruptions caused by volatile degassing upon interaction between one or more rising magmas and a fluid interface (Mitchell et al., 1986; Lorenz, 2003). The resulting eruptions propels rising magma aggressively upward through the "diatreme facies" via explosive boring through overlying strata up to the surface (Kostrovitsky, 1967; Mitchell, 1986; Wilson and Head, 2007). Ideal diatreme morphology consists of a deep, underlying feeder dike to which the primary conduit is connected at the root zone (Figure 1.1.; Mitchell, 1986; Wilson and Head, 2007). The propagating magma rises through the cylindrical conduit into the shallow hypabyssal facies below the fluid interface. Above this pipe is the post-eruption, adiabatic-expansion zone, or diatreme facies. The diatreme facies conically widens upward, leading up to the top (maar) crater facies lined with a tuff ring from ejecta at the surface (Figure 1.1; Mitchell, 1986; Wilson and Head, 2007). As diatremes host a complex suite of magmatic and hydrothermal events throughout their development, it can

be difficult to analyze diatreme rocks without having contextualized primitive material rarely preserved from the earliest stages of diatreme formation.

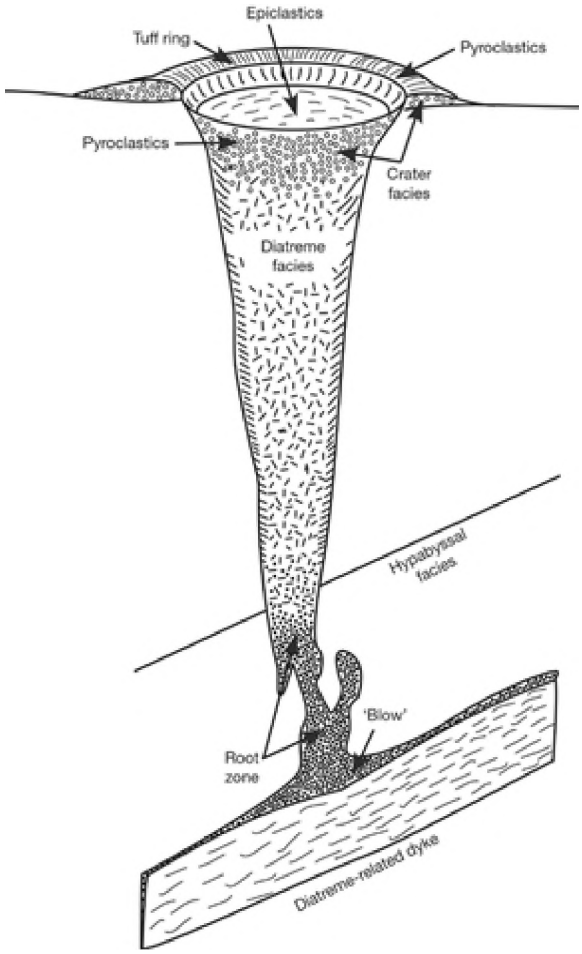

Figure 1.1: A conceptual model illustrating distinct facies zones for a standard diatreme complex from Mitchell, 1986, and Wilson and Head, 2017. The K-24 alnöite sample investigated for this study is interpreted to represent the lower diatreme facies.

The Avon Alkaline Igneous Province (AAIP) in southwest Ste. Genieve County, Missouri hosts over eighty of the only known Devonian-age (386 +/- 1 Ma) ultramafic

igneous bodies in the Midwestern United States (Kidwell, 1947; Zartman et al, 1967; Freeman, 2016). Magmatic activity resulting in the formation of the AAIP is determined to originate from mid-continental North American plate rifting during the Acadian orogeny as a result of Andean-style flat slab subduction around 395-380 Ma (Murphy and Keppie, 2005, Shavers et al., 2017). Low-angle subduction has been shown to coincide with kimberlite magmatism and, if hydrous minerals become destabilized, generated fluids can percolate through the mantle and trigger continental lithosphere metasomatism in some cases (Currie and Beaumont, 2011). Igneous activity from the Precambrian established relic fractures in felsic bedrock due to failed rifting of the early North American Plate, resulting in high-angle dip-slip uplifting (Shavers et al. 2017, Marshak and Paulsen, 1996). The significance of these high angle faults in the AAIP provides potential conduits for magmatic ascension upon decompression.

A lower diatreme facies derived alnöite from the AAIP, the focus of this study, was first noted by Singewald and Milton, 1930, and further detailed by Kidwell, 1947 (sample K-24) and later by Mansker, 1973. The samples of K-24 and corresponding thin sections (BHF-01-24) examined in this study were prepared and petrologically characterized by Freeman, 2016, who analyzed the mineral chemistry of olivine phenocrysts and established and the diatreme emplacement age via $^{40}Ar/^{39}Ar$ geochronology of biotite (386 $\pm$ 1 ma). Shavers et al., 2016, presented results of a geochemical and stable carbon and oxygen isotopic study of a variety of rock-types associated with the AAIP which include the diatreme facies (K-24). They concluded that a mafic, carbonate-rich melt source intrinsic to the mantle carrying pristine olivine phenocrysts constituted the kimberlite magma that formed the diatreme and crater facies.

The K-24 alnöite supports intriguing olivine-phlogopite spatial relationships, textures, and alteration characteristics potentially unique and indicative of the magmatic evolution of the AAIP and AUC diatreme petrogenesis in general. Olivine geothermometry of K-24 rocks performed by Freeman, 2016, indicate that crystallization temperatures of olivine range from 1500-1750°C at pressures between 1.6 and 5.4 GPa.

The olivine macrocrysts that define the distinctive ovoid domains and phlogopite crystals within the melilite and carbonate matrix of the diatreme facies are suggestive of several possible petrogenetic processes including: mingling of distinct mantle magmas (Brooker and Kjarsgaard, 2010; Sparks, 2013; Freeman, 2016; Morgavi et al., 2017), liquid-magma immiscibility (Brooker and Kjarsgaard, 2010; Potter et al., 2017), assimilation (Russel et al., 2012, Sparks, 2013), and formation of an aerosol during emplacement (Gernon et al., 2012). The complexity of this rock fabric, the presence of multiple textural and mineralogical domains, and the intimate spatial association of olivine, in various degrees of serpentinization, and phlogopite indicated that a detailed petrographic and mineral compositional investigation is needed to provide insight into the magmatic and post-magmatic processes, as well as the nature of the mantle sources, that contributed to the formation of this diatreme.

The focus of this study aims to identify the peculiar textural and spatial relationships of two major minerals within the K-24 samples (olivine and phlogopite) and unravel the sequential magmatic history resulting in these petrographic features. Petrographic and geochemical analysis of individual mineral species in thin sections are performed to develop and constrain petrogenetic models depicting the evolution of the K-24 diatreme in the AAIP. These observations are bound within the diatreme-facies of the

K-24 alnöite, which provides a vital snapshot of the magmatic origins of the unique textures linked to the petrogenesis of this alkaline ultramafic carbonatite (AUC) diatreme leading up to and including the emplacement and secondary alteration of the K-24 alnöite specifically. Through this study, the nature of mantle sources involved in the generation of these undersaturated alkaline igneous rocks found in the AAIP will be constrained.

PAPER

I. MULTIPLE GENERATIONS OF PHLOGOPITE IN AN ALNÖITE DIATREME: INSIGHTS INTO THE PETROGENESIS OF THE AVON ALKALINE IGNEOUS PROVINCE, MISSOURI

Nathan G. Limbaugh, John P. Hogan, and Willis E. Hames

ABSTRACT

Alkaline Ultramafic Carbonatite (AUC) complexes, although rare, are valued for diamonds and REEs, and as windows into subcontinental and mantle processes as recorded by rock fabrics, mineral spatial relationships, and mineral compositions. We report specifically on olivine and phlogopite petrographic relationships and compositions from the Devonian alnöite diatreme-facies of the Avon Alkaline Igneous Province, Missouri. The diatreme alnöite is a mixture of domains of olivine magmaclasts (OM) set in a crystal-rich melilite matrix. OM are highly fractured, serpentinized olivine pseudomorphs with variable amounts of pristine olivine fragments. Larger olivine domains typically exhibit clear crystal faces and irregular "channels" indicative of a skeletal morphology due to rapid growth. Islands of unaltered olivine are homogeneous, Mg-rich ($Fo_{86.9}$-$Fo_{89.9}$) and exhibit variation in trace element (e.g., Ni, Cr, Co, Ti, P) abundances consistent with limited fractional crystallization and origin from a metasomatized fertile peridotite partial melt. Three textural varieties of phlogopite are recognized. Tabular, euhedral phlogopite (phl-Ia) crystals occur along the margins of OM and within the melilite matrix. Small (mm-size) euhedral to subhedral phlogopite (phl-Ib)

phenocrysts occur inside the "channels" of skeletal olivine. Phlogopite (phl-II) crystals occur as anhedral, oxide-rich, palmate porphyroblast clusters, rimming serpentinized olivine and scattered throughout the matrix. These phlogopite populations are geochemically distinct, showing ion substitution enrichments (i.e. Ba, Al, Ti). These mineral and geochemical relationships enable the development of a comprehensive petrogenetic model of the Avon Alkaline Igneous Province AUC diatreme complex.

1. INTRODUCTION

Diatremes and maars have been of longstanding and increasing interest within the geoscience community. Additionally, the growing economic demand for rare earth elements (REEs) and diamonds associated with kimberlitic diatremes, has sparked further curiosity in unraveling the origin of diatreme formation. Studying diatreme petrographic mineral textures and geochemical characteristics can further scientific understanding of mantle magmatic evolution processes involved in diatreme petrogenesis within igneous complexes.

Diatremes are subterranean pipes that fed shallower magmatic eruptions caused by volatile degassing upon interaction between one or more rising magmas and a fluid interface (Mitchell et al., 1986; Lorenz, 2003). The resulting eruptions propels rising magma aggressively upward through the "diatreme facies" via explosive boring through overlying strata up to the surface (Kostrovitsky, 1967; Mitchell, 1986; Wilson and Head, 2007). Ideal diatreme morphology consists of a deep, underlying feeder dike to which the primary conduit is connected at the root zone (Figure 1.; Mitchell, 1986; Wilson and

Head, 2007). The propagating magma rises through the cylindrical conduit into the shallow hypabyssal facies below the fluid interface. Above this pipe is the post-eruption, adiabatic-expansion zone, or diatreme facies. The diatreme facies conically widens upward, leading up to the top (maar) crater facies lined with a tuff ring from ejecta at the surface (Figure 1; Mitchell, 1986; Wilson and Head, 2007). As diatremes host a complex suite of magmatic and hydrothermal events throughout their development, it can be difficult to analyze diatreme rocks without having contextualized primitive material rarely preserved from the earliest stages of diatreme formation.

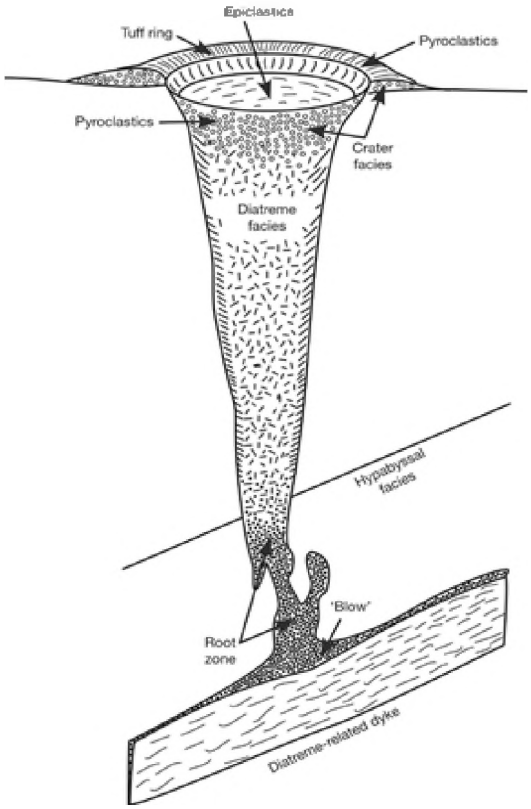

Figure 1: A conceptual model illustrating distinct facies zones for a standard diatreme complex from Mitchell, 1986, and Wilson and Head, 2017. The K-24 alnöite sample investigated for this study is interpreted to represent the lower diatreme facies.

The Avon Alkaline Igneous Province (AAIP) in southwest Ste. Genieve County, Missouri hosts over eighty of the only known Devonian-age (386 +/- 1 Ma) ultramafic igneous bodies in the Midwestern United States (Kidwell, 1947; Zartman et al, 1967; Freeman, 2016). Magmatic activity resulting in the formation of the AAIP is determined to originate from mid-continental North American plate rifting during the Acadian orogeny as a result of Andean-style flat slab subduction around 395-380 Ma (Murphy and Keppie, 2005, Shavers et al., 2017). Low-angle subduction has been shown to coincide with kimberlite magmatism and, if hydrous minerals become destabilized, generated fluids can percolate through the mantle and trigger continental lithosphere metasomatism in some cases (Currie and Beaumont, 2011). Igneous activity from the Precambrian established relic fractures in felsic bedrock due to failed rifting of the early North American Plate, resulting in high-angle dip-slip uplifting (Shavers et al. 2017, Marshak and Paulsen, 1996). The significance of these high angle faults in the AAIP provides potential conduits for magmatic ascension upon decompression.

A lower diatreme facies derived alnöite from the AAIP, the focus of this study, was first noted by Singewald and Milton, 1930, and further detailed by Kidwell, 1947 (sample K-24) and later by Mansker, 1973. The samples of K-24 and corresponding thin sections (BHF-01-24) examined in this study were prepared and petrologically characterized by Freeman, 2016, who analyzed the mineral chemistry of olivine phenocrysts and established and the diatreme emplacement age via $^{40}Ar/^{39}Ar$ geochronology of biotite (386 $\pm$ 1 ma). Shavers et al., 2016, presented results of a geochemical and stable carbon and oxygen isotopic study of a variety of rock-types associated with the AAIP which include the diatreme facies (K-24). They concluded that

a mafic, carbonate-rich melt source intrinsic to the mantle carrying pristine olivine phenocrysts constituted the kimberlite magma that formed the diatreme and crater facies.

The K-24 alnöite supports intriguing olivine-phlogopite spatial relationships, textures, and alteration characteristics potentially unique and indicative of the magmatic evolution of the AAIP and AUC diatreme petrogenesis in general. Olivine geothermometry of K-24 rocks performed by Freeman, 2016, indicate that crystallization temperatures of olivine range from 1500-1750°C at pressures between 1.6 and 5.4 GPa. The olivine macrocrysts that define the distinctive ovoid domains and phlogopite crystals within the melilite and carbonate matrix of the diatreme facies are suggestive of several possible petrogenetic processes including: mingling of distinct mantle magmas (Brooker and Kjarsgaard, 2010; Sparks, 2013; Freeman, 2016; Morgavi et al., 2017), liquid-magma immiscibility (Brooker and Kjarsgaard, 2010; Potter et al., 2017), assimilation (Russel et al., 2012, Sparks, 2013), and formation of an aerosol during emplacement (Gernon et al., 2012). The complexity of this rock fabric, the presence of multiple textural and mineralogical domains, and the intimate spatial association of olivine, in various degrees of serpentinization, and phlogopite indicated that a detailed petrographic and mineral compositional investigation is needed to provide insight into the magmatic and post-magmatic processes, as well as the nature of the mantle sources, that contributed to the formation of this diatreme.

The focus of this study aims to identify the peculiar textural and spatial relationships of two major minerals within the K-24 samples (olivine and phlogopite) and unravel the sequential magmatic history resulting in these petrographic features. Petrographic and geochemical analysis of individual mineral species in thin sections are

performed to develop and constrain petrogenetic models depicting the evolution of the K-24 diatreme in the AAIP. These observations are bound within the diatreme-facies of the K-24 alnöite, which provides a vital snapshot of the magmatic origins of the unique textures linked to the petrogenesis of this alkaline ultramafic carbonatite (AUC) diatreme leading up to and including the emplacement and secondary alteration of the K-24 alnöite specifically. Through this study, the nature of mantle sources involved in the generation of these undersaturated alkaline igneous rocks found in the AAIP will be constrained.

2. GEOLOGIC SETTING

The Ozark Dome, spanning across south-central Missouri, serves as the backbone of the regional geological setting that hosted the petrogenesis of the AAIP (Figure 2). The Ozark Dome is a broad regional upwarp defined by outward dipping Paleozoic strata. A thin veneer of Paleozoic clastic sedimentary and carbonate cover rocks overlay Mesoproterozoic crystalline basement rock of the Ozark Dome (Thompson, 1995). The extrusive and intrusive igneous basement rocks are well exposed in the St. Francois Mountains within the eastern front of the Ozark Dome (Van Schmus and Hinze, 1985). The intracratonic Illinois Basin borders the Ozark Dome to the east and the late Proterozoic Reelfoot Rift constitutes the southern edge (McBride and Nelson, 1999; Tuttle et al., 2002, Csontos and Van Arsdale, 2008, Van Arsdale et al., 2013).

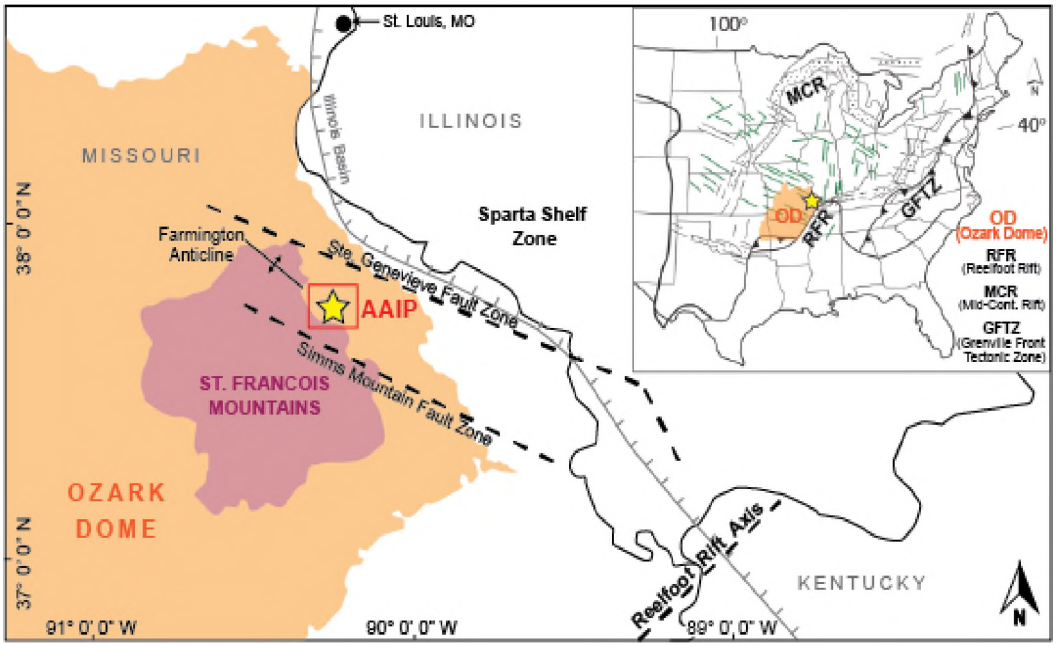

Figure 2: Regional geologic map of the AAIP study area. Adapted from Marshak et al., 2000, Shavers et al. 2016, and Liu, 2019.

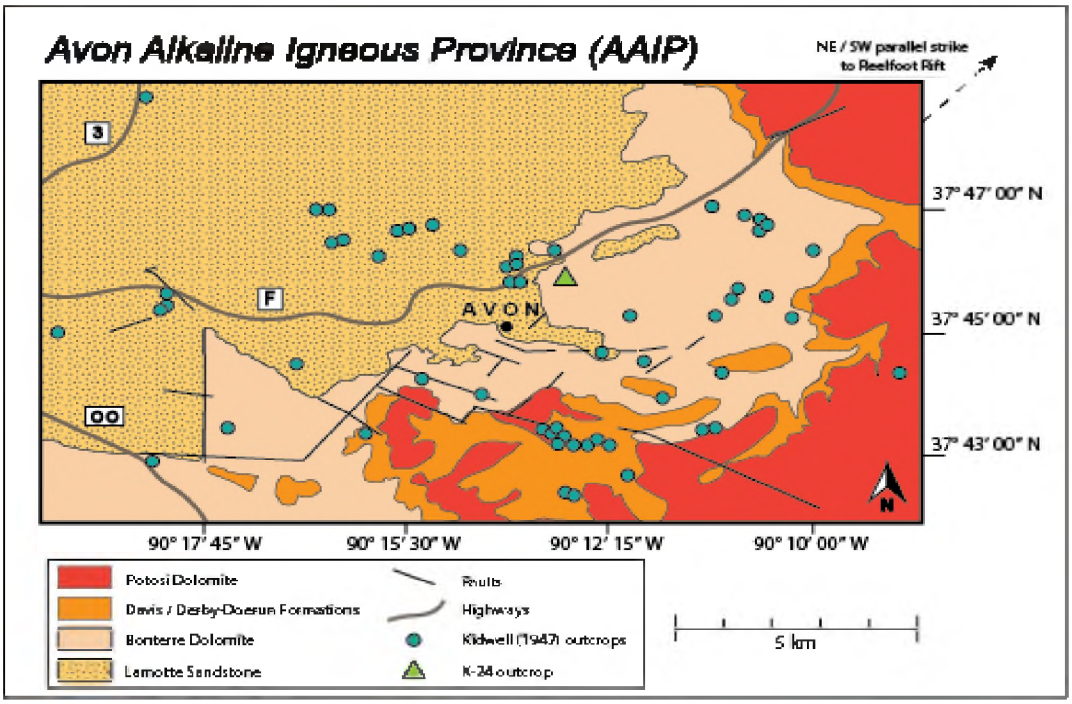

Figure 3: Local geologic map of the AAIP. Study area focuses on K-24 outcrop within southwest Ste. Genevieve county, Missouri. Adapted from Kidwell, 1947, and Shavers et al., 2016.

Dominant fault trends (NW-SE and NE-SW) and subsequent tectonic faults have exploited the basement fabric in a form of structural inheritance (Marshak et al., 2000, 2003; Harrison and Schultz, 2002). The Ste. Genevieve and Simms Mountain Fault Zones are two such NW-SE faults which confine the AAIP (Figure 2). These faults formed amid Neoproterozoic to early Cambrian rifting and are associated with the formations of Reelfoot Rift. The NW-SW trend define smaller faults within the AAIP (Figure 3). Reactivation of these faults during the Devonian, as a result of far-field lithospheric stress from North American Plate boundaries, localized intrusion of magma associated with the AAIP (Horrall et al. 1993, Marshak and Paulsen 1996; Timmons et al., 2001; Marshak et al., 2000, 2003; Harrison and Schultz, 2002).

According to Kidwell, 1947, Freeman, 2016, and Shavers et al., 2018, there appears to be a linearity of outcrops hosting AAIP intrusions in Avon (Figure 3) which may be due to exposures associated with stream erosion, otherwise the intrusions are scattered throughout the area. Of the multiple igneous intrusions constituting the AAIP, the subject of this study focuses on the Kidwell 24 (K-24) AUC kimberlitic diatreme pipe, just one of at least four sections identified as members of the same diatreme complex (Figure 4). Mantle-fed through a lower root zone with explosion breccias extending upward along the wall rock facies, the K-24 diatreme intruded through overlying Paleozoic strata basement rock. This basement rock mainly comprises metaluminous to mildly peraluminous, type-A epizonal rhyolite and mesozonal granite of the Eastern Granite-Rhyolite Province formed approximately 1.48 Ga in the Precambrian (Menuge et al., 2002; Freeman, 2016). The diatreme bore further upward through overlying late Cambrian Lamotte Sandstone and Bonterre Dolomite currently at the

surface of the AAIP (Kidwell, 1947; Thompson, 1995; Freeman, 2016; Shavers et al., 2016, 2017). The carbonate content found in the lower facies of this diatreme was derived from a mantle source while upper facies carbonate was derived from deuteric alteration with surrounding crustal carbonate rocks via fluid-rock interaction and metasomatism (Shavers et al. 2016).

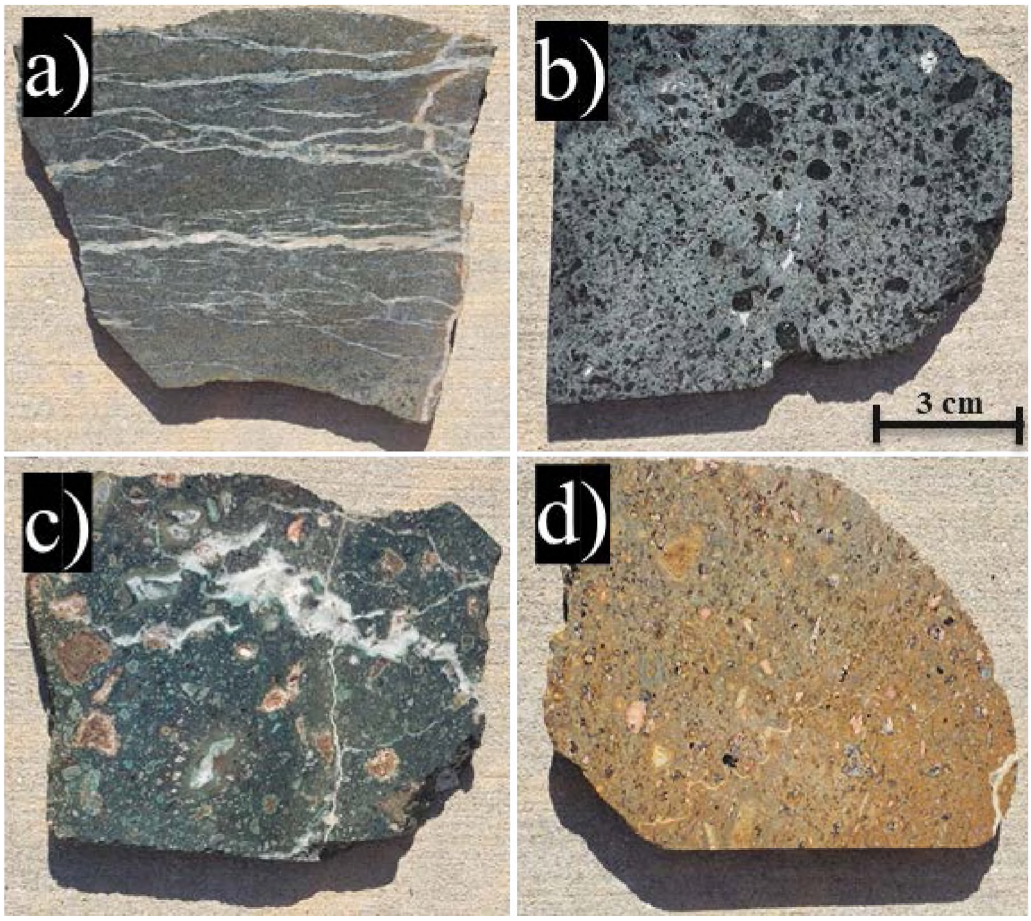

Figure 4: AAIP rock samples from various facies of the diatreme complex. 4a) dike facies, 4b) diatreme facies (alnöite), 4c) upper diatreme / lower maar facies, 4d) crater tuff facies.

Tectonic-induced fault formation and resultant decompression melting are typical hosting conditions for mantle-derived intrusions to form kimberlitic systems (Jelsma et al. 2009). Far-field stresses generated from late Paleozoic continental collision along southern and eastern margins of North America induced reactivation of Precambrian basement-faults in the mid-continent (Marshak et al., 2000, 2003; Harrison and Schultz, 2002; Liu, 2019). Two near-vertical, steeply dipping faults along basement rock penetrated upward in an en-echelon propagation between 100-600 km long and 2-20 km wide regionally. These steep faults are associated with episodic fault reactivation and lateral slip displacement along the Ste. Genevieve Fault Zone in the Paleozoic (Nelson et al., 1985; Clendenin et al., 1989; Marshak and Paulsen, 1996; Marshak et al., 2000, 2003; Harrison and Shultz, 2002; Cox, 2009). The uplifting of the northern block of the Sparta Shelf Zone correlates to reactivation of NW-SE faults and sinistral wrench faulting in the Ste. Genevieve Fault Zone and are likely responsible for localizing emplacement of the AAIP (Nelson et al., 1985; Marshak and Paulsen, 1997; Shavers et al., 2017).

3. METHODOLOGY

3.1. PETROGRAPHY

For petrographic analysis of all BHF-01-24 thin sections (A – F), a Leica DV-M6 petrographic microscope provided by the Missouri University of Science & Technology. Plane polarized light (PPL) and cross polarized light (XPL) modes were utilized to observe textural and spatial details of minerals present in thin sections both on the millimeter and micrometer scale. All BHF-01-24 thin sections contain direct samples

from the K-24 alnöite and petrographic observations made from these thin sections reflect magmatic processes involved in the petrogenesis of the K-24 alnöite diatreme.

3.2. ELECTRON MICROPROBE ANALYSIS

Thin section BHF-01-24-D from the K-24 sample was selected and carbon-coated for electron microprobe analysis (EMPA) at Auburn University, targeting phlogopite and olivine (Figure 5). A JEOL 8600 electron microprobe was used for EMPA, set with 15 kV accelerating voltage and 20 nA beam current for spot analyses and 15 kV accelerating voltage and 50 nA beam current for wavelength-dispersive X-ray spectroscopy (WDS) mapping. 1µm spot-size and 20 second counting times for quantitative analyses of samples and standards was additionally set. The calculated weight percentages of oxides were based on WDS spectrometer measurements, ZAF matrix corrections, and published compositions of mineral and synthetic standards (included in Appendix B). Accuracy of standard analysis compared with average oxide abundances of target minerals are included below (Table 1, Table 2)

For olivine, phl-Ia, and phl-Ib probe data, an olivine magmaclast (OM) in BHF-01-24-D.1 was selected for target locations for electron microprobe analysis (Figure 5). For phl-II and other phl-Ia, an unspecified zone in BHF-01-24-D with an abundance of phlogopite in matrix was additionally selected for microprobe analysis. Further images of these locations and specific targets are detailed in Appendix B. Petrographic classification designating the different types of phlogopite (phl-Ia, ph-Ib, and phl-II) are included in Section 5.

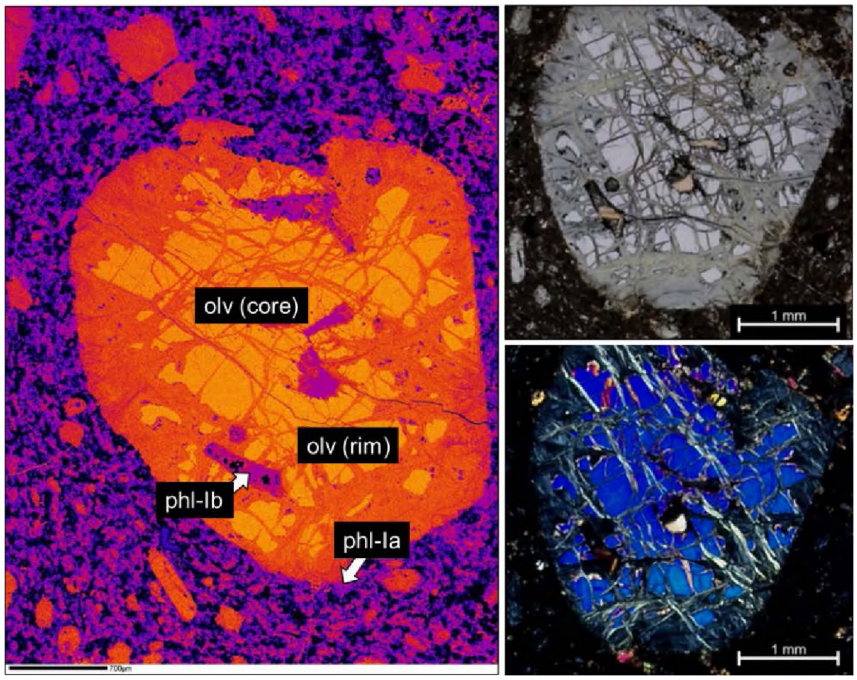

Figure 5: BHF-01-24-D.1. EMPA zone of study for geochemical analysis. Electron microprobe false-color magnesium elemental image (left) and petrographic images in plane polarized light (upper right) and cross polarized light (lower right)

Table 1: Olivine standard accuracy with K-24 olivine oxide abundance averages.

	olv standard	standard SD(±)	olv core (ave.)	olv rim (ave.)
SiO_2	39.3811	1.1169	39.4192	39.5758
TiO_2	0.0151	0.0116	0.0064	0.0294
Al_2O_3	0.0182	0.0299	0.0526	0.0635
Cr_2O_3	0.0378	0.0157	0.0519	0.0505
FeO	17.1556	0.1220	11.8692	11.7592
MnO	0.3521	0.0365	0.1619	0.1573
MgO	43.3933	0.3399	47.6733	47.4192
NiO	0.0042	0.0112	0.2878	0.2543
BaO	b.d.l	b.d.l	b.d.l	b.d.l
CaO	0.0182	0.0221	0.1762	0.1845
Na_2O	0.0064	0.0127	0.0161	0.0426
K_2O	b.d.l	b.d.l	b.d.l	b.d.l
Total	**100.3800**	**1.3361**	**99.7133**	**99.5358**

Table 2: Phlogopite standard accuracy with K-24 phlogopite oxide abundance averages.

	phl standard	standard SD(±)	phl-Ia (ave.)	phl-Ib (ave.)	phl-II (ave.)
SiO_2	32.5522	0.9370	41.4629	41.1257	37.0186
TiO_2	1.3960	0.0535	0.8992	1.4920	2.3601
Al_2O_3	17.6456	0.4382	8.7543	11.0643	13.1700
Cr_2O_3	0.0000	0.0000	0.0000	0.0000	0.0000
FeO	31.7911	0.5649	6.9893	5.7936	5.2279
MnO	0.0436	0.0333	0.0464	0.0328	0.0612
MgO	2.6904	0.1518	25.7443	24.8293	23.4150
NiO	0.0000	0.0000	0.0000	0.0000	0.0000
BaO	0.0713	0.0562	0.1570	0.8520	4.7979
CaO	0.0214	0.0137	0.2242	0.0179	0.0274
Na_2O	0.2127	0.3447	0.1070	0.1852	0.2243
K_2O	8.8383	0.2287	9.4384	9.6183	7.7088
Total	**96.2344**	**1.2635**	**93.8229**	**95.0109**	**94.0112**

4. PETROLOGY

Alnöites are mafic lamprophyres characterized by phenocrysts of biotite, titanium-rich pyroxene, and olivine set in a melilite-matrix (Rosenbusch, 1887; Rock, 1986; Le Bas and Streckeisen, 1991). Minor to trace minerals can include calcite, chlorite, chromite, spinel, perovskite, and andradite garnet.

The K-24 diatreme alnöite of the AAIP is characterized by abundant, distinctive olivine domains and phlogopite set in a melilite matrix with local carbonate. These features also fit with the refined definition of a kimberlitic diatreme rock suggested by Clement et al., 1984. Unlike other alnöite, this sample is noticeably void of titanim-rich pyroxene and garnet. The K-24 alnöite sample (Figure 6) displays size variability of

olivine domains (magmaclasts) ranging from as large as 2 cm to less than 1 mm across. Olivine magmaclasts (OM) are the most abundant mineral species, constituting nearly 50% of the fine grain matrix. OM are dark grey, subhedral, sub-rounded, and conspicuous when compared against the light grey aphanitic groundmass. Phlogopite phenocrysts are harder to identify by the naked eye due to their smaller size (< 1 mm) and constitute about 10% of the matrix as the second most abundant mineral in groundmass. Phlogopite is euhedral to subhedral, tabular, and is found in channels or as rimming or contacting OM domains.

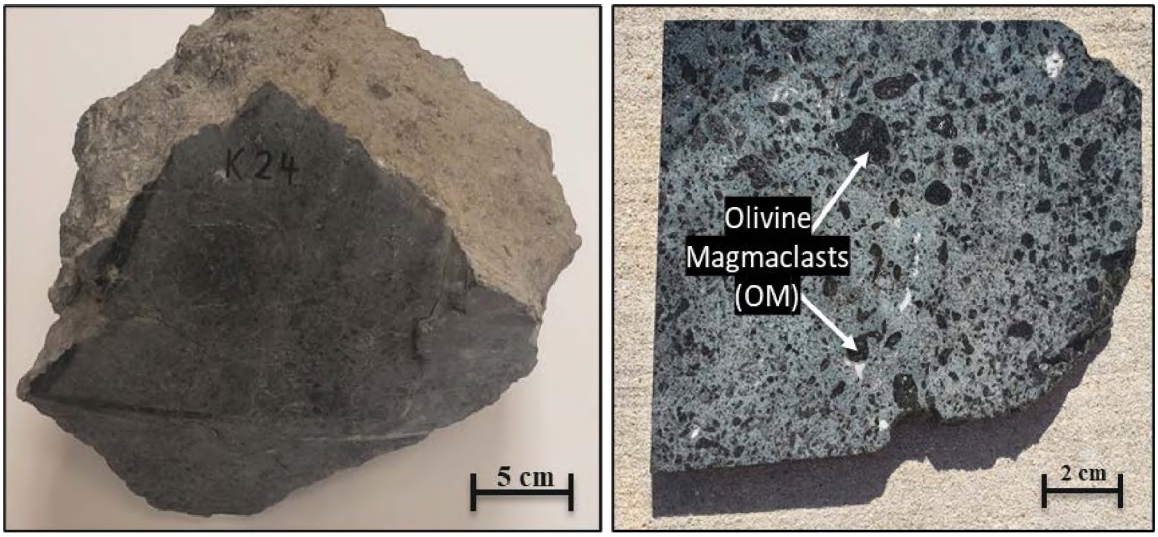

Figure 6: K-24 alnöite sample from the lower diatreme facies. Grey matrix is dominated by subhedral dark-grey olivine domains (magmaclasts) exhibiting porphyritic textures.

Minor mineral species identified include oxides (spinel, ilmenite, perovskite, magnetite, chromite), melilite, apatite, and chlorite (Freeman, 2016, Shavers et al., 2016). Quartz and Ti-rich garnet (schorlomite) have been noted as minerals found in other

diatreme / crater facies samples but were not identified in the sample used in this study (Le Bas and Streckeisen, 1991, Freeman, 2016, Shavers et al., 2016). While minor mineral phases can be useful for understanding various aspects of petrogenesis, this study focuses on major mineral phases (olivine and phlogopite).

5. TEXTURAL AND SPATIAL ANALYSIS

5.1. OLIVINE MAGMACLASTS (OM)

Criteria used to classify OM include: the abundance of relict olivine comparable to serpentine within the cores of OM, the grouping of relict olivine within OM, and the abundance of channels each OM exhibit (Table 3). Average OM sizes are included by zone in Appendix A and are not distinct criteria for classification.

Table 3: OM type characterization based on different key textural characteristics

OM Type	Relict Olivine Abundance	Relict Olivine Grouping	Channels
OM-I	relict olivine > serpentine	consolidated/fragmented core	common
OM-II	relict olivine < serpentine	scattered throughout OM	uncommon
OM-IIIa	fully-serpentinized	no relict olivine present	sparse
OM-IIIb	fully-serpentinized	no relict olivine present	absent

OM are massive and/or fragmented domains, with few hosting “channels” where minerals such as phlogopite (phl-Ib) and chlorite have crystallized within. OM have a

large margin of size variation throughout samples, being as small as a few micrometers to as large as a few centimeters and are subhedral/sub-rounded and generally ovoid in shape. Mineral inclusions of oxides are uncommon in OM both along and separate from fracture lines and channels, while such inclusions were not observed directly within relict olivine preserved in cores of OM-I and OM-II, which maintain different amounts and clustering of relict olivine (Figure 7). Of the magmaclasts which preserve relict olivine, only OM-I and OM-II show varying degrees of serpentinization but have not fully lost all olivine content, as shown petrographically (Figure 7). Distinctions are made between OM-IIIa (i.e. overall larger size, the rare presence of channels) and OM-IIIb (i.e. overall larger size, the rare presence of channels) petrographically (Figure 8).

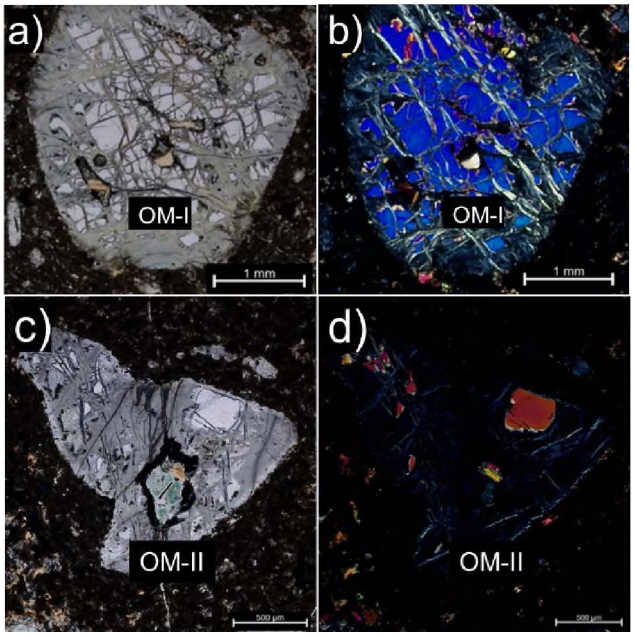

Figure 7: OM-I and OM-II comparison. Petrographic images from BHF-01-24-D.1 (7a and 7b) and BHF-01-24-D.5 (7c and 7d). 7a) Plane polarized image of an OM-I; 7b) cross polarized image of an OM-I; 7c) plane polarized image of an OM-II; 7d) cross polarized image of an OM-II.

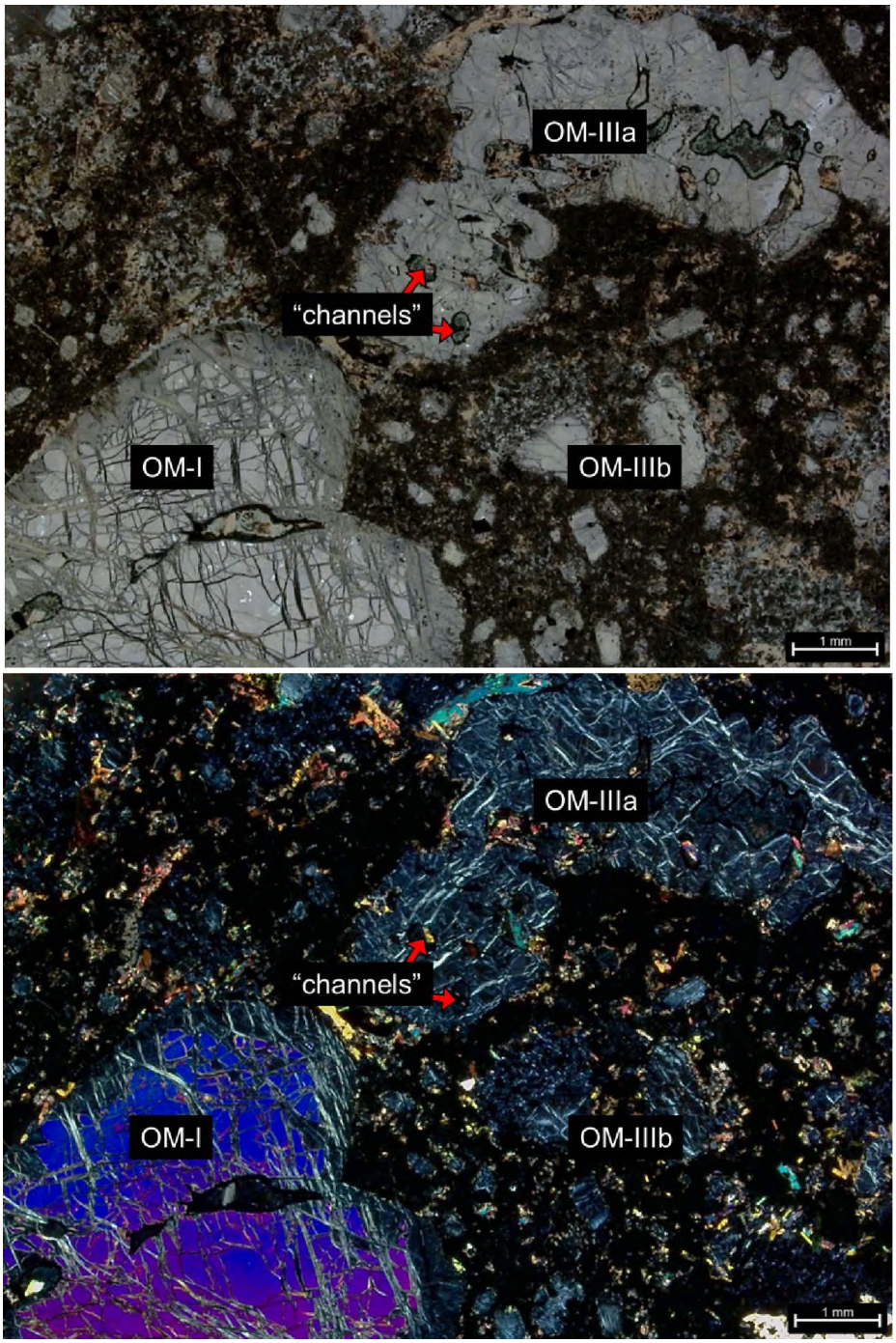

Figure 8: BHF-01-24-E.3 showing OM-I, OM-IIIa, and OM-IIIb. Petrographic microscope images collected in plane-polarized light (top) and cross-polarized light (bottom) display common optical characteristics that distinguish OM types, most notably channel presence, the amount and grouping of relict olivine in each type.

Outside of the relict olivine, but still confined to OM domains, are serpentinized rim zones in which relict olivine altered to serpentine (Figure 9). Relict olivine phenocrysts are between 0.01mm to 1cm in diameter and are not found outside of OM domains. Fractures segregate relict olivine within large consolidated complexes in OM-I and "scatter" relict olivine in OM-II. Relict olivine phenocrysts are euhedral to subhedral, white in plane-polarized light and exhibit high birefringence in cross-polarized light. In plane-polarized light, serpentinite domains are also pale-grey in color and exhibit anomalous extinction in cross-polarized light.

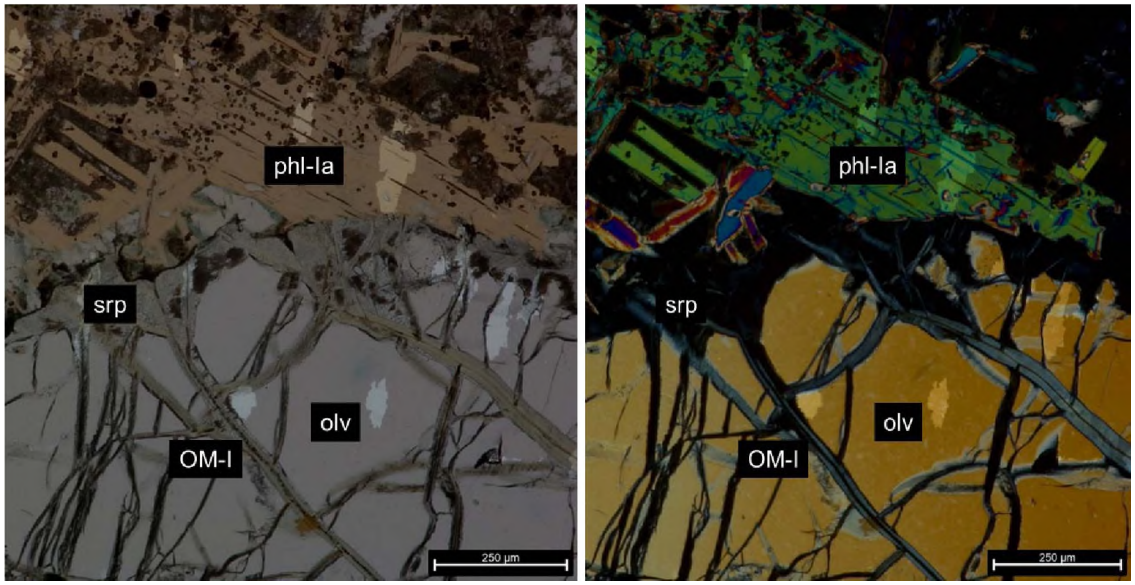

Figure 9: BHF-01-24-A.4: OM-I with consolidated grouping relict olivine (olv) rimmed by serpentine (srp), which is in contact with phl-Ia. Petrographic microscope images collected in plane-polarized light (left) and cross-polarized light (right) show distinct optical characteristic differences between relict olivine, serpentinized olivine domain and phlogopite. Cross-cutting between phlogopite phenocrysts and serpentinized fracture lines within OM are also visible.

5.2. PHLOGOPITE

Phlogopite is the second most abundant mineral and is found as both euhedral and anhedral crystals across samples, which is a primary criterion used for classification of different phlogopite types in this study (Table 4). Additionally, orientation between phlogopite of the same classification, association with OM, and birefringence are key parameters used to distinguish differences between phlogopite groups.

Table 4: Phlogopite type characterization based on different key textural characteristics

Phl Type	Shape	OM association	Birefringence	Oxides
Phl-Ia	Euhedral / tabular	contacting, matrix	nominal	moderate
Phl-Ib	Euhedral-subhedral	contacting, embaying	nominal	Rare/none
Phl-II	Anhedral / irregular	rimming, matrix	lower	high

In plane-polarized light, phlogopite appear tan in color, while in cross-polarized light, phl-I exhibit birefringence nominal for phlogopite (second order) however phl-II shows lower than nominal birefringence. Phl-Ia and phl-Ib (to varied degrees) show euhedral, tabular features and commonly display cleavage lines while phl-II show anhedral, irregular textures, making it difficult to discern individual crystals. Phl-I have been identified as spatially cross-cutting each other at various orientations and typically contact OM rims (Figure 9) whereas phl-II rim OM, sometimes entirely rimming OM-IIIb (Figure 10). Phl-Ib is petrographically similar to phl-Ia; the primary difference being phl-Ib forms only in OM channels and therefore is smaller on average in size. Size

variation of phlogopite is relatively consistent throughout the matrix, as crystals are between a few micrometers to a few millimeters in length. Oxide inclusions are more common in phl-II with phl-Ia having moderate amounts of oxide inclusions comparably and phl-Ib having virtually no oxide inclusions. Phlogopite types are not exclusively spatially dependent upon one another, however phl-Ia and phl-II have been found to border yet remain spatially independent from one another (Figure 10, Figure 11, Figure 12). The crystal shape quality, spatial relationship with OM, oxide abundance, and birefringence are notable contrasting features between phl-Ia and phl-II (Figure 10).

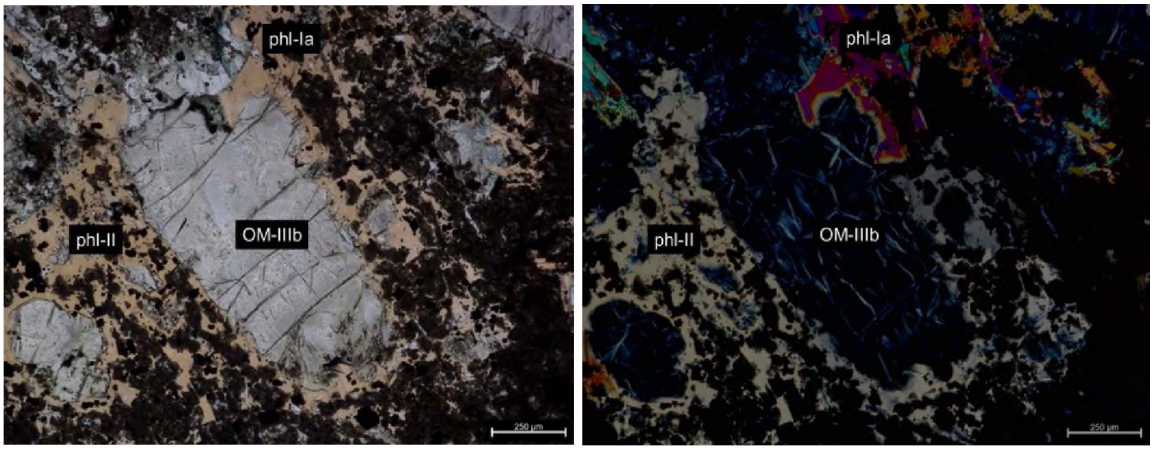

Figure 10: BHF-01-24-D.6: Phl-Ia and phl-II contacting and rimming OM-IIIb. Petrographic microscope images collected in plane-polarized light (top) and cross-polarized light (bottom) show distinct optical characteristic differences between the two types of phlogopite.

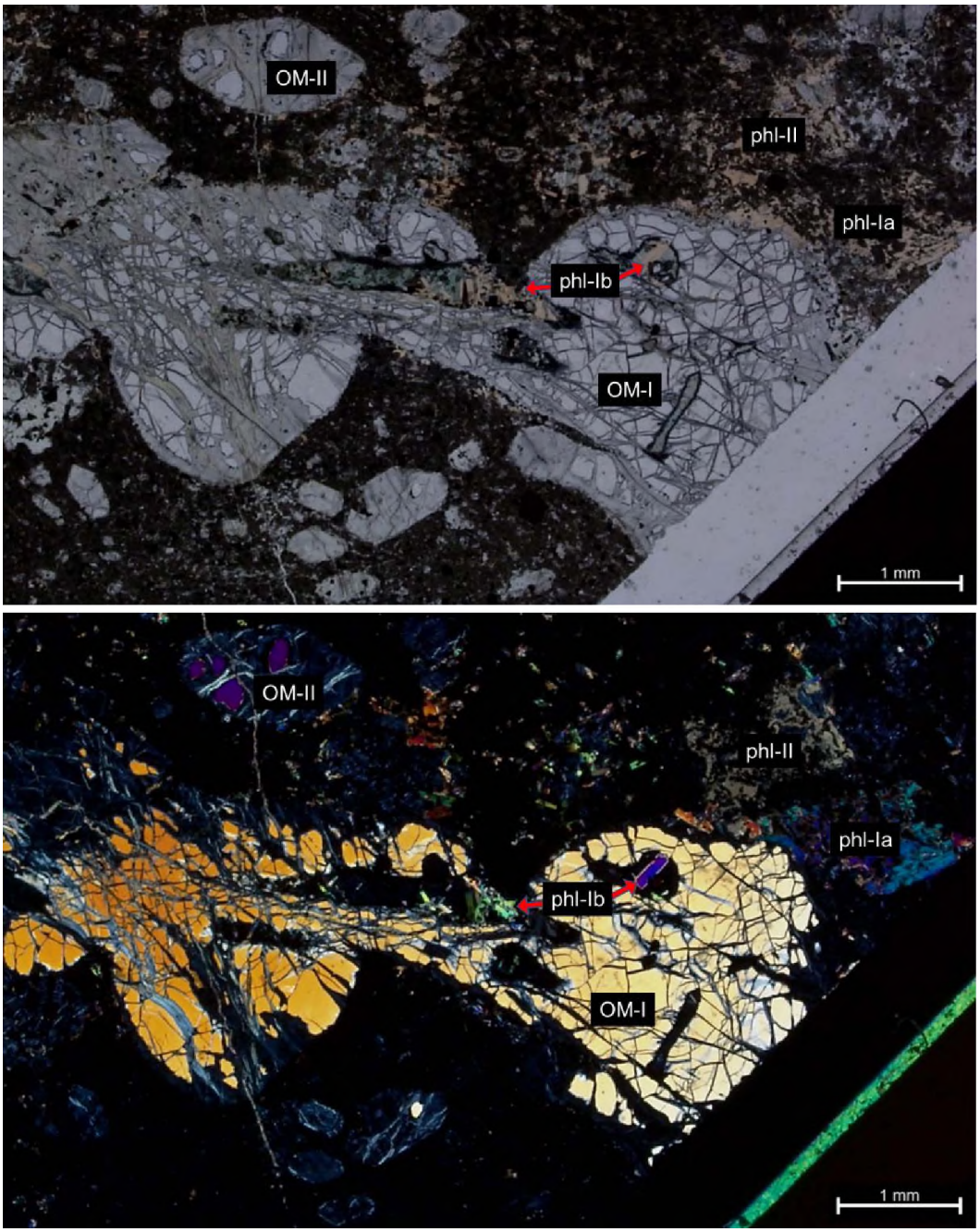

Figure 11: BHF-01-24-D.4: OM-I with all phl types. Petrographic images including phl-Ia, phl-Ib, and phl-II in close spatial proximity to an OM-I domain, plane-polarized (top) and cross-polarized (bottom).

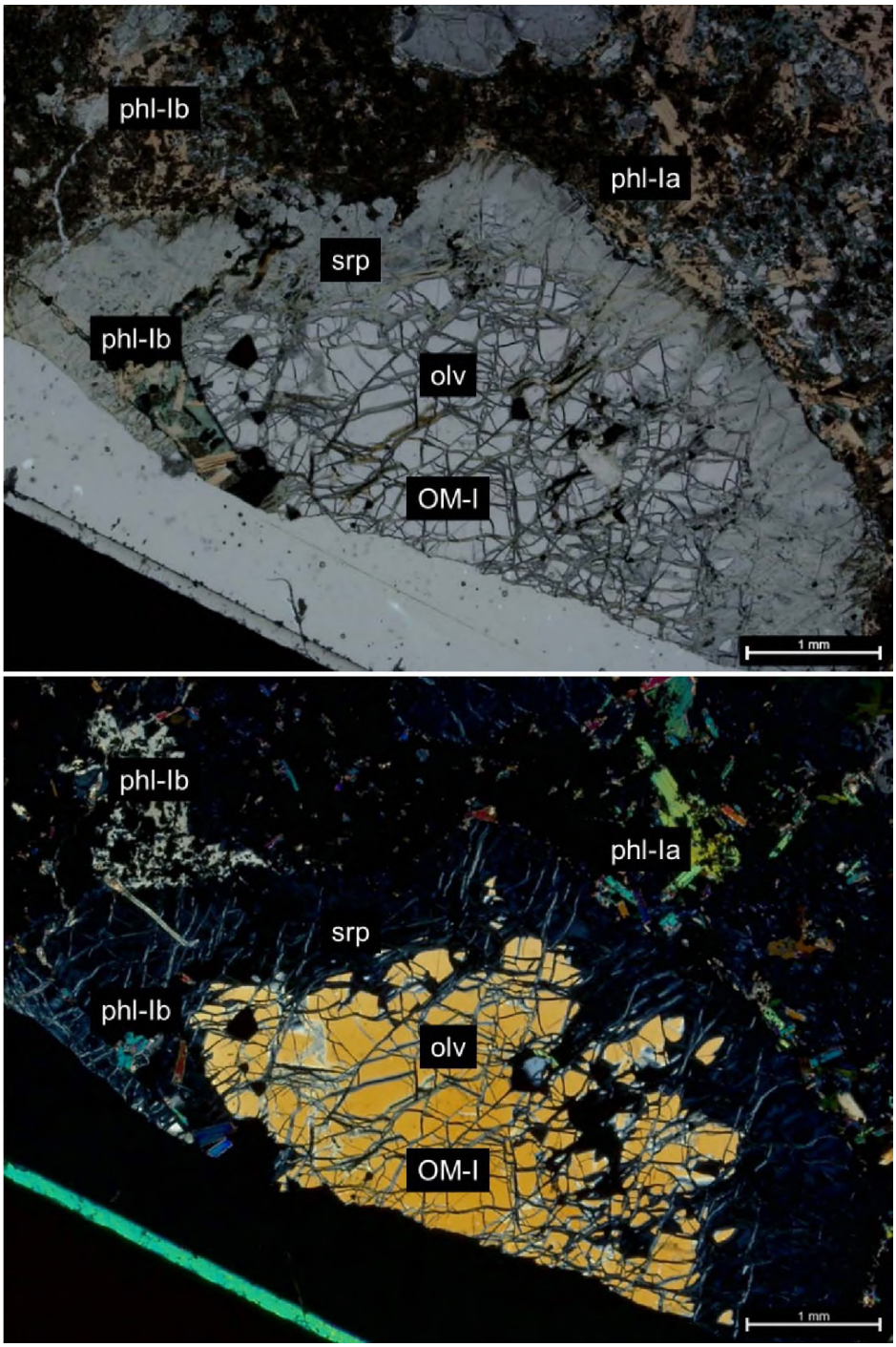

Figure 12: BHF-01-24-F.1: OM-I with all phl types. Petrographic images including phl-Ia, phl-Ib, and phl-II in close spatial proximity to an OM-I domain, plane-polarized (top) and cross-polarized (bottom).

6. MINERAL COMPOSITIONS

6.1. OLIVINE

Elemental abundance data collected (Table 5, Table 6) was plotted along bivariate abundance ratios of various elements (Figure 13, Figure 14) as well as abundance variations of similar igneous rocks bearing olivine based on minor element concentration ratios (Figure 15).

Table 5: OM-I relict olivine (core and rim) elemental concentrations (oxide wt. %).

OM-I olv (core)													Averages	SD (±)
SiO_2	40.6500	39.7000	40.0700	39.4700	40.0200	39.9300	38.8000	39.3000	37.8900	39.0100	39.1500	39.0400	**39.4192**	0.7237
TiO_2	0.0000	0.0038	0.0000	0.0010	0.0153	0.0029	0.0000	0.0124	0.0000	0.0000	0.0029	0.0381	**0.0064**	0.0112
Al_2O_3	0.0120	0.0000	0.0000	0.1201	0.0000	0.0000	0.0990	0.0569	0.1095	0.0569	0.1347	0.0420	**0.0526**	0.0518
Cr_2O_3	0.0566	0.0370	0.0059	0.0939	0.0637	0.0466	0.0295	0.0643	0.0491	0.0435	0.0633	0.0694	**0.0519**	0.0223
FeO	11.8400	11.6700	11.7600	12.1200	11.9100	11.4600	12.2500	11.6200	12.1800	11.7700	12.0300	11.8200	**11.8692**	0.2386
MnO	0.0915	0.1544	0.1545	0.1324	0.1463	0.1929	0.1430	0.1569	0.1639	0.1979	0.2390	0.1706	**0.1619**	0.0367
MgO	47.9100	47.7000	47.8100	47.7200	48.1900	47.8400	47.3300	47.6100	47.9500	47.3600	47.2000	47.4600	**47.6733**	0.2921
NiO	0.3118	0.2308	0.2309	0.2648	0.3067	0.2759	0.2792	0.2871	0.3163	0.2753	0.3732	0.3020	**0.2878**	0.0389
BaO	b.d.l	b.d.l	b.d.l	b.d.l	b.d.l	b.d.l	b.d.l	b.d.l	b.d.l	b.d.l	b.d.l	b.d.l	**0.0000**	0.0000
CaO	0.1994	0.1824	0.2030	0.2051	0.1606	0.1770	0.1396	0.1806	0.1822	0.1773	0.1614	0.1457	**0.1762**	0.0211
Na_2O	0.0000	0.0000	0.0000	0.0046	0.0000	0.0776	0.0000	0.0000	0.0417	0.0137	0.0551	0.0000	**0.0161**	0.0268
K_2O	b.d.l	b.d.l	b.d.l	b.d.l	b.d.l	b.d.l	b.d.l	b.d.l	b.d.l	b.d.l	b.d.l	b.d.l	**0.0000**	0.0000
Total	101.0600	99.6700	100.2300	100.1300	100.8100	100.0000	99.0800	99.3000	98.8700	98.9100	99.4100	99.0900	**99.7133**	0.7355
%Fo	87.18%	87.35%	87.30%	86.72%	87.18%	87.49%	86.64%	87.22%	86.73%	87.03%	86.54%	87.01%	**87.03%**	0.0031
Mg#	87.8262	87.9334	87.8762	87.5403	87.8254	88.3197	87.3233	87.9589	87.6161	87.7950	87.6088	87.7431	**87.7805**	0.2494
OM-I olv (rim)													Averages	SD (±)
SiO_2	39.3100	39.1200	38.9900	39.0600	39.7600	39.9900	38.9000	39.0800	40.5900	40.6500	39.3500	40.1100	**39.5758**	0.6263
TiO_2	0.0000	0.0588	0.0010	0.0306	0.0217	0.0000	0.0522	0.0336	0.0277	0.0237	0.0553	0.0476	**0.0294**	0.0214
Al_2O_3	0.0644	0.0738	0.0502	0.2545	0.0000	0.0682	0.0000	0.0435	0.0000	0.1944	0.0124	0.0000	**0.0635**	0.0815
Cr_2O_3	0.0333	0.0554	0.0401	0.1156	0.0488	0.0421	0.0382	0.0429	0.0821	0.0444	0.0505	0.0123	**0.0505**	0.0260
FeO	11.6100	11.6000	12.0700	11.8600	11.7900	11.8200	12.0600	11.6500	11.7800	11.6700	11.6400	11.5600	**11.7592**	0.1715
MnO	0.0676	0.1273	0.1698	0.2282	0.1934	0.1740	0.1708	0.1770	0.1172	0.1883	0.1226	0.1517	**0.1573**	0.0427
MgO	47.3300	46.9000	47.8800	47.0400	47.6100	47.7100	47.8400	47.3300	47.4100	46.9100	47.7500	47.3200	**47.4192**	0.3462
NiO	0.2977	0.3221	0.2290	0.2701	0.3082	0.3131	0.2618	0.1684	0.3098	0.2074	0.1447	0.2198	**0.2543**	0.0600
BaO	b.d.l	b.d.l	b.d.l	b.d.l	b.d.l	b.d.l	b.d.l	b.d.l	b.d.l	b.d.l	b.d.l	b.d.l	**0.0000**	0.0000
CaO	0.1857	0.1957	0.1990	0.2114	0.1366	0.1848	0.1672	0.1841	0.2025	0.1738	0.1933	0.1799	**0.1845**	0.0195
Na_2O	0.0748	0.1411	0.0192	0.1331	0.0000	0.0664	0.0095	0.0095	0.0570	0.0000	0.0000	0.0000	**0.0426**	0.0520
K_2O	b.d.l	b.d.l	b.d.l	b.d.l	b.d.l	b.d.l	b.d.l	b.d.l	b.d.l	b.d.l	b.d.l	b.d.l	**0.0000**	0.0000
Total	98.9700	98.6000	99.6500	99.2000	99.8600	100.3700	99.5000	98.7200	100.5800	100.0600	99.3200	99.6000	**99.5358**	0.6183
%Fo	87.26%	87.00%	86.94%	86.47%	87.14%	87.04%	86.97%	87.22%	87.06%	86.89%	87.41%	87.36%	**87.06%**	0.0025
Mg#	89.9016	88.1202	87.6522	87.8940	87.8042	87.9393	87.6319	87.8890	87.8888	87.7551	87.9718	87.9490	**88.0331**	0.6042

From oxide abundances, mineral formula recalculations were preformed to determine the atoms per fractional unit (a.p.f.u.) of elements in Table 6. The redox state of iron was determined from the difference between total iron (II) a.p.f.u. and the difference between total anion charge and calculated cation charges. Normalization to full anion charge (oxygen) was selected for determining normalization factors.

Table 6: OM-I relict olivine (core and rim) elemental concentrations (a.p.f.u.).

OM-I olv (core)	(a.p.f.u)												Averages	SD (±)
Si	0.9960	0.9874	0.9907	0.9801	0.9852	0.9891	0.9754	0.9822	0.9572	0.9801	0.9801	0.9792	**0.9819**	0.0097
Ti	0.0000	0.0001	0.0000	0.0000	0.0003	0.0001	0.0000	0.0002	0.0000	0.0000	0.0001	0.0007	**0.0001**	0.0002
Al	0.0003	0.0000	0.0000	0.0035	0.0000	0.0000	0.0029	0.0017	0.0033	0.0017	0.0040	0.0012	**0.0016**	0.0015
Cr	0.0011	0.0007	0.0001	0.0018	0.0012	0.0009	0.0006	0.0013	0.0010	0.0009	0.0013	0.0014	**0.0010**	0.0004
Fe 2+	0.2426	0.2427	0.2431	0.2514	0.2452	0.2337	0.2575	0.2428	0.2553	0.2466	0.2492	0.2479	**0.2465**	0.0064
Fe 3+	0.0000	0.0000	0.0000	0.0002	0.0000	0.0037	0.0000	0.0000	0.0020	0.0007	0.0027	0.0000	**0.0008**	0.0013
Mn	0.0019	0.0033	0.0032	0.0028	0.0031	0.0040	0.0030	0.0033	0.0035	0.0042	0.0051	0.0036	**0.0034**	0.0008
Mg	1.7500	1.7686	1.7622	1.7665	1.7686	1.7668	1.7739	1.7739	1.8060	1.7739	1.7617	1.7747	**1.7706**	0.0132
Ni	0.0061	0.0046	0.0046	0.0053	0.0061	0.0055	0.0056	0.0058	0.0064	0.0056	0.0075	0.0061	**0.0058**	0.0008
Ba	0.0000	0.0000	0.0000	0.0000	0.0000	0.0000	0.0000	0.0000	0.0000	0.0000	0.0000	0.0000	**0.0000**	0.0000
Ca	0.0052	0.0049	0.0054	0.0055	0.0042	0.0047	0.0038	0.0048	0.0049	0.0048	0.0043	0.0039	**0.0047**	0.0005
Σ VI	2.0073	2.0248	2.0186	2.0371	2.0287	2.0193	2.0474	2.0339	2.0824	2.0382	2.0357	2.0396	**2.0344**	0.0187
Na	0.0000	0.0000	0.0000	0.0002	0.0000	0.0037	0.0000	0.0000	0.0020	0.0007	0.0027	0.0000	**0.0008**	0.0012
K	0.0000	0.0000	0.0000	0.0000	0.0000	0.0000	0.0000	0.0000	0.0000	0.0000	0.0000	0.0000	**0.0000**	0.0000
OM-I olv (rim)	**(a.p.f.u)**												**Averages**	**SD (±)**
Si	0.9801	0.9850	0.9738	0.9792	0.9878	0.9885	0.9733	0.9823	0.9993	1.0041	0.9824	0.9964	**0.9860**	0.0097
Ti	0.0000	0.0011	0.0000	0.0006	0.0004	0.0000	0.0010	0.0006	0.0005	0.0004	0.0010	0.0009	**0.0006**	0.0004
Al	0.0019	0.0022	0.0015	0.0075	0.0000	0.0020	0.0000	0.0013	0.0000	0.0057	0.0004	0.0000	**0.0019**	0.0024
Cr	0.0007	0.0011	0.0008	0.0023	0.0010	0.0008	0.0008	0.0009	0.0016	0.0009	0.0010	0.0002	**0.0010**	0.0005
Fe 2+	0.1976	0.2373	0.2512	0.2421	0.2449	0.2411	0.2519	0.2444	0.2398	0.2410	0.2430	0.2401	**0.2395**	0.0139
Fe 3+	0.0444	0.0069	0.0009	0.0065	0.0000	0.0032	0.0005	0.0005	0.0027	0.0000	0.0000	0.0000	**0.0055**	0.0125
Mn	0.0014	0.0027	0.0036	0.0048	0.0041	0.0036	0.0036	0.0038	0.0024	0.0039	0.0026	0.0032	**0.0033**	0.0009
Mg	1.7593	1.7606	1.7828	1.7580	1.7634	1.7581	1.7844	1.7736	1.7401	1.7274	1.7773	1.7525	**1.7615**	0.0168
Ni	0.0060	0.0065	0.0046	0.0054	0.0062	0.0062	0.0053	0.0034	0.0061	0.0041	0.0029	0.0044	**0.0051**	0.0012
Ba	0.0000	0.0000	0.0000	0.0000	0.0000	0.0000	0.0000	0.0000	0.0000	0.0000	0.0000	0.0000	**0.0000**	0.0000
Ca	0.0050	0.0053	0.0053	0.0057	0.0036	0.0049	0.0045	0.0050	0.0053	0.0046	0.0052	0.0048	**0.0049**	0.0005
Σ VI	2.0163	2.0237	2.0507	2.0330	2.0235	2.0200	2.0519	2.0334	1.9987	1.9881	2.0334	2.0061	**2.0232**	0.0192
Na	0.0000	0.0000	0.0000	0.0002	0.0000	0.0037	0.0000	0.0000	0.0020	0.0007	0.0027	0.0000	**0.0008**	0.0012
K	0.0000	0.0000	0.0000	0.0000	0.0000	0.0000	0.0000	0.0000	0.0000	0.0000	0.0000	0.0000	**0.0000**	0.0000

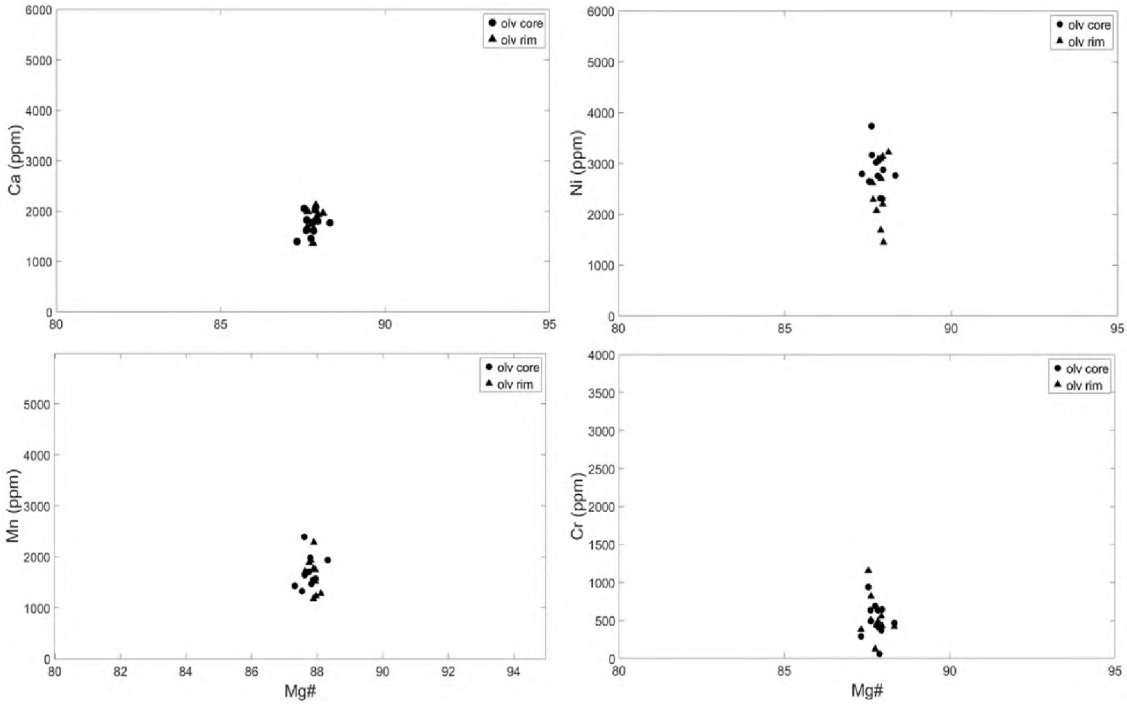

Figure 13: Olivine bivariate plots for Mg# vs. trace element abundance. Analysis of olivine was taken from points within the cores of and rims of relict olivine clusters within the same OM.

Figure 13 indicates that trace element enrichment in relict olivine is considerably homogeneous, as rim and core values do not plot in distinctively separate zones. Variation in trace element concentration with respect to a consistently high magnesium number indicates that significant fractionation of olivine may not be present. Figure 14 demonstrates that olivine from K-24 plot distinctively beyond fractionated melting curves and likely derive from a fertile peridotite source. More bivariate plots for K-24 olivine are included in Appendix C.

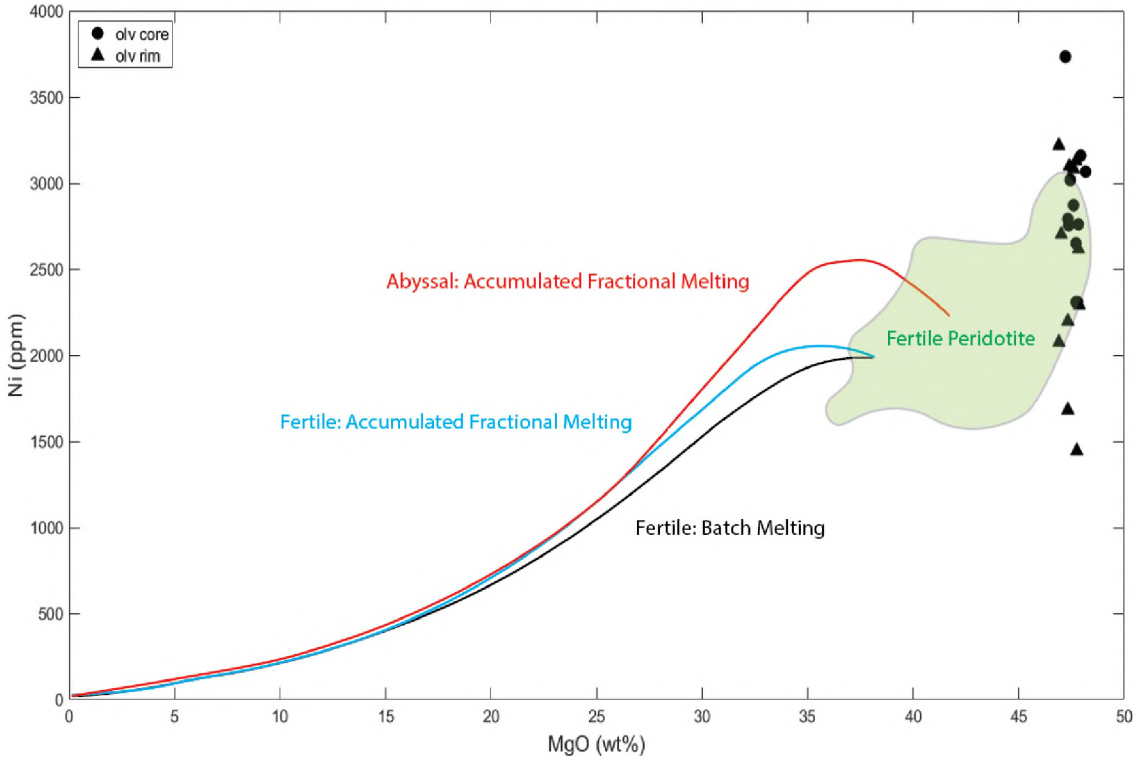

Figure 14: Olivine bivariate plot of nickel and magnesium oxide ratios with melting curves and zonal plot of fertile peridotite (Herzberg, 1993, 2011).

K-24 olivine shows geochemical distinction from olivine associated with most other igneous rock types and as expected have similarity proximity to continental alkaline rocks (Figure 15). The grouping of K-24 olivine reflects unique signatures specific to the AAIP and mid-continental AUC diatreme alnöites. Therefore, either an expansion of the continental alkaline rock zone (Figure 15) should be assessed based on the compositional data of these olivine phenocrysts, or perhaps a unique zone for alkaline ultramafic carbonatite diatreme rocks and/or continental alnöites can now be identified.

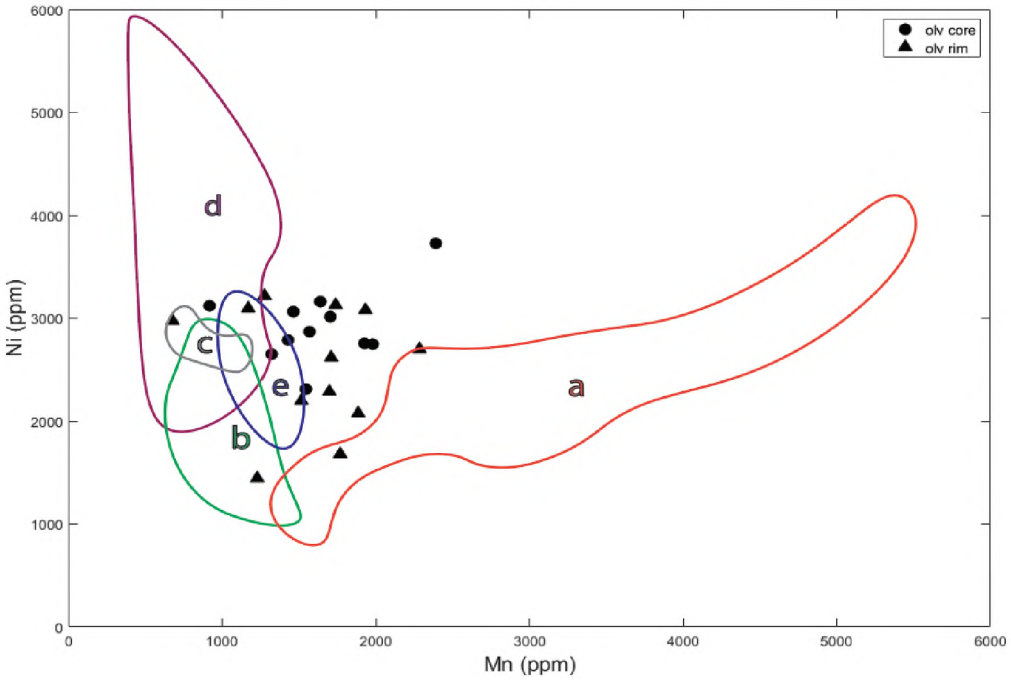

Figure 15: Elemental abundance variation diagram for OM relict olivine with olivine from other mafic and ultramafic assemblages (Foley et. al, 2013). a) ocean island basalt, b) kimberlite, c) diamondiferous mantle rock, d) Eastern Mediterranean lamproite, e) continental alkaline rocks.

6.2. PHLOGOPITE

Phlogopite types show distinct geochemical differences that suggest a variety of magmatic processes were involved in their formation and within the K-24 diatreme. Furthermore, these geochemical distinctions parallel petrographic distinctions. Elemental abundance data collected (Table 7, Table 8) was plotted along abundance variations of similar igneous rocks bearing phlogopite based on common ion substitution pairs for kimberlite-derived phlogopite (Figure 16), as well as bivariate abundance ratios of trace elements compared to titanium-oxide concentration (Figure 17).

Table 7: Phlogopite elemental concentrations (oxide wt. %).

	Phl-Ia														Averages	SD (+)
SiO_2	41.5600	40.8000	39.5500	40.9800	41.3800	42.3600	41.0800	42.1800	42.6300	41.9400	43.0200	40.7000	41.4500	40.8500	**41.4629**	0.9109
TiO_2	0.6720	0.7324	0.8242	0.8925	0.9745	1.1072	1.0071	1.0568	0.9475	0.8804	0.8337	0.8759	0.8976	0.8864	**0.8992**	0.1171
Al_2O_3	9.7000	9.2000	9.2500	8.7500	9.0600	9.3000	8.9200	8.4900	8.1000	8.4000	8.7500	8.2900	7.8000	8.5500	**8.7543**	0.5225
Cr_2O_3	b.d.l	b.d.l	b.d.l	b.d.l	b.d.l	b.d.l	b.d.l	b.d.l	b.d.l	b.d.l	b.d.l	b.d.l	b.d.l	b.d.l	**0**	0.0000
FeO*	6.4300	6.5400	6.7200	6.7800	6.8500	7.1900	6.7800	7.5900	7.4100	7.1500	7.4100	7.2600	6.8400	6.9000	**6.9893**	0.3485
MnO	0.0257	0.0170	0.0763	0.0538	0.0934	0.0486	0.0226	0.0820	0.0398	0.0113	0.0454	0.0595	0.0736	0.0000	**0.0464**	0.0286
MgO	26.4600	25.5600	25.4400	25.9700	24.9200	25.8200	25.0000	25.6200	25.8600	26.0400	26.3900	25.4900	26.1200	25.7300	**25.7443**	0.4530
NiO	b.d.l	b.d.l	b.d.l	b.d.l	b.d.l	b.d.l	b.d.l	b.d.l	b.d.l	b.d.l	b.d.l	b.d.l	b.d.l	b.d.l	**0**	0.0000
BaO	0.1024	0.0656	0.0179	0.2087	0.0954	0.2527	0.2681	0.1844	0.2094	0.1131	0.1195	0.1789	0.2383	0.1434	**0.157**	0.0748
CaO	0.1567	0.2098	0.6003	0.1352	0.0920	0.0803	0.0787	0.0918	0.0990	0.5222	0.2625	0.5355	0.1723	0.1030	**0.2242**	0.1863
Na_2O	0.2219	0.1453	0.1034	0.0848	0.1556	0.1194	0.1462	0.0000	0.1427	0.0755	0.0947	0.1043	0.0330	0.0708	**0.107**	0.0554
K_2O	10.0967	9.8565	9.5185	9.8387	9.2961	9.6252	9.3762	9.4117	9.2872	9.1449	9.2249	9.0737	9.1805	9.2071	**9.4384**	0.3091
Total	95.4254	93.1266	92.1006	93.6937	92.9170	95.9034	92.6789	94.7067	94.7256	94.2774	96.1507	92.5678	92.8053	92.4407	**93.8229**	1.3654
Mg#	94.7723	94.0878	95.0847	95.4160	92.3469	92.8571	93.0272	93.1973	93.7288	94.5854	93.7288	94.7458	96.2712	95.0847	**94.21**	1.1157
	Phl-Ib														**Averages**	**SD (+)**
SiO_2	41.1400	41.7900	42.0800	40.9500	41.1200	40.6000	40.8300	42.1700	40.4800	41.0100	41.4300	41.4300	40.5400	40.1900	**41.1257**	0.5995
TiO_2	1.4831	1.4961	1.5448	1.5212	1.5619	1.5491	1.5485	1.4565	1.4811	1.4153	1.4512	1.5074	1.4560	1.4151	**1.492**	0.0492
Al_2O_3	10.6500	10.8600	10.5400	10.8600	11.1300	11.5900	11.6900	10.7400	10.3400	11.1600	11.2300	11.4000	11.4300	11.2800	**11.0643**	0.4078
Cr_2O_3	b.d.l	b.d.l	b.d.l	b.d.l	b.d.l	b.d.l	b.d.l	b.d.l	b.d.l	b.d.l	b.d.l	b.d.l	b.d.l	b.d.l	**0**	0.0000
FeO*	5.7300	5.6100	6.0000	5.8900	5.6800	5.8300	5.7200	5.9000	5.8100	5.8700	5.8100	5.8300	5.8700	5.5600	**5.7936**	0.1205
MnO	0.0368	0.0481	0.0142	0.0707	0.0226	0.0113	0.0199	0.0428	0.0791	0.0000	0.0170	0.0255	0.0398	0.0312	**0.0328**	0.0223
MgO	24.8700	24.6500	25.1700	24.9500	24.6100	24.0100	24.6900	24.9200	24.7700	24.9700	24.8300	24.9500	24.9300	25.2900	**24.8293**	0.3002
NiO	b.d.l	b.d.l	b.d.l	b.d.l	b.d.l	b.d.l	b.d.l	b.d.l	b.d.l	b.d.l	b.d.l	b.d.l	b.d.l	b.d.l	**0**	0.0000
BaO	0.8402	0.8051	0.8365	0.8702	0.9001	0.8236	0.6994	0.8243	0.9766	0.8531	1.0010	0.9132	0.7902	0.7951	**0.852**	0.0778
CaO	0.0257	0.0000	0.0398	0.0000	0.0074	0.0307	0.0100	0.0368	0.0124	0.0108	0.0215	0.0249	0.0299	0.0000	**0.0179**	0.0138
Na_2O	0.2112	0.1407	0.2640	0.1552	0.1503	0.1554	0.1692	0.2229	0.1553	0.2021	0.2114	0.1976	0.1462	0.2110	**0.1852**	0.0370
K_2O	9.6608	9.5274	9.8654	9.4117	9.5808	9.6519	9.7231	9.5986	9.7231	9.6164	9.4918	9.7676	9.5452	9.4918	**9.6183**	0.1235
Total	94.6478	94.9274	96.3547	94.6790	94.7631	94.2520	95.1001	95.9119	93.8276	95.1077	95.4939	96.0462	94.7773	94.2642	**95.0109**	0.7253
Mg#	91.9521	90.7376	91.7667	92.0962	91.0653	89.5189	90.7376	90.9091	92.7959	91.6096	90.9247	90.9247	91.6096	93.1624	**91.42**	0.9317
	Phl-II														**Averages**	**SD (+)**
SiO_2	37.5600	36.7300	35.7100	37.2100	36.7300	37.7000	36.5900	36.2000	36.0300	36.7700	38.2200	37.8100	37.7600	37.2400	**37.0186**	0.7460
TIO_2	2.3473	2.4256	2.4499	2.4128	2.4584	2.4193	2.3881	2.2466	2.3058	2.2153	2.3414	2.3502	2.3405	2.3398	**2.3601**	0.0719
Al_2O_3	12.9800	13.4600	12.9900	13.5200	12.9800	13.4800	13.6300	13.6700	13.0100	12.5300	12.8300	13.2000	12.9500	13.1500	**13.17**	0.3362
Cr_2O_3	b.d.l	b.d.l	b.d.l	b.d.l	b.d.l	b.d.l	b.d.l	b.d.l	b.d.l	b.d.l	b.d.l	b.d.l	b.d.l	b.d.l	**0**	0.0000
FeO*	5.1600	5.0800	5.4000	5.2400	5.2700	5.2400	5.0600	5.4500	5.1000	5.1600	5.3800	5.0700	5.2700	5.3100	**5.2279**	0.1281
MnO	0.0590	0.0761	0.0813	0.0308	0.0702	0.0910	0.1009	0.0393	0.0112	0.0281	0.0000	0.0898	0.0505	0.1292	**0.0612**	0.0367
MgO	23.6900	23.3300	23.4800	23.3500	23.7200	23.7100	23.2800	23.2900	23.4800	22.9700	23.3200	23.2100	23.3800	23.6000	**23.415**	0.2137
NiO	b.d.l	b.d.l	b.d.l	b.d.l	b.d.l	b.d.l	b.d.l	b.d.l	b.d.l	b.d.l	b.d.l	b.d.l	b.d.l	b.d.l	**0**	0.0000
BaO	4.8300	4.7600	4.7600	4.7500	4.9700	5.0200	5.1100	4.5900	4.9500	4.9900	4.7200	4.6200	4.5400	4.5600	**4.7979**	0.1854
CaO	0.0163	0.0245	0.0561	0.0220	0.0350	0.0173	0.0325	0.0342	0.0187	0.0220	0.0407	0.0334	0.0000	0.0310	**0.0274**	0.0133
Na_2O	0.1880	0.2174	0.3185	0.1924	0.2028	0.2883	0.2313	0.1636	0.1060	0.2270	0.2937	0.2737	0.2163	0.2214	**0.2243**	0.0561
K_2O	7.9528	7.8461	7.7927	7.8550	7.7927	7.7304	7.8372	7.7215	7.6148	7.4992	7.5881	7.4636	7.6326	7.5970	**7.7088**	0.1459
Total	94.7834	93.9497	93.0385	94.5830	94.2291	95.6963	94.2600	93.4052	92.6265	92.4116	94.7339	94.1207	94.1399	94.1784	**94.0112**	0.8877
Mg#	91.4485	91.0839	92.8196	90.3846	92.4694	90.9091	90.9091	90.7666	92.5087	90.9408	89.8955	90.0350	90.4181	91.2740	**91.13**	0.9083

From oxide abundances, mineral formula recalculations were preformed to determine the atoms per fractional unit (a.p.f.u.) of elements in Table 8. The redox state of iron was determined from the difference of excessive octahedral cations (a.p.f.u) and

total iron (a.p.f.u.), as normalizing to a full octahedral and tetrahedral site were necessary. While other elements have been known to be associated to two sites (i.e. Mg, Ni, Ti), these elements were constrained to their primary sites such that full occupancy of tetrahedral and octahedral sites could be attained.

Table 8: Phlogopite elemental concentrations (a.p.f.u.).

Phl - Ia (matrix)			(a.p.f.u)												Averages	SD (±)
Si	5.92	5.96	5.85	5.95	6.05	6.01	6.03	6.05	6.11	6.03	6.05	5.98	6.04	5.97	**6.00**	0.0640
Fe^{3+}	0.46	0.45	0.54	0.55	0.39	0.44	0.42	0.51	0.52	0.54	0.50	0.58	0.62	0.55	**0.51**	0.0629
Al^{IV}	1.63	1.58	1.61	1.50	1.56	1.55	1.54	1.44	1.37	1.42	1.45	1.44	1.34	1.47	**1.49**	0.0853
Σ IV	8.01	7.99	8.00	8.00	8.00	8.00	7.99	8.00	8.00	7.99	8.00	8.00	8.00	7.99	**8.00**	0.0056
Al^{VI}	0.00	0.00	0.00	0.00	0.00	0.00	0.00	0.00	0.00	0.00	0.00	0.00	0.00	0.00	**0.00**	0.0000
Ti	0.07	0.08	0.09	0.10	0.11	0.12	0.11	0.11	0.10	0.10	0.09	0.10	0.10	0.10	**0.10**	0.0125
Cr	0.00	0.00	0.00	0.00	0.00	0.00	0.00	0.00	0.00	0.00	0.00	0.00	0.00	0.00	**0.00**	0.0000
Fe^{2+}	0.31	0.35	0.29	0.27	0.45	0.42	0.41	0.40	0.37	0.32	0.37	0.31	0.22	0.29	**0.34**	0.0629
Mn	0.00	0.00	0.01	0.01	0.01	0.01	0.00	0.01	0.00	0.00	0.01	0.01	0.01	0.00	**0.01**	0.0049
Mg	5.62	5.57	5.61	5.62	5.43	5.46	5.47	5.48	5.53	5.59	5.53	5.59	5.68	5.61	**5.56**	0.0715
Ni	0.00	0.00	0.00	0.00	0.00	0.00	0.00	0.00	0.00	0.00	0.00	0.00	0.00	0.00	**0.00**	0.0000
Σ VI	6.00	6.00	6.00	6.00	6.00	6.01	5.99	6.00	6.00	6.01	6.00	6.01	6.01	6.00	**6.00**	0.0056
Ba	0.01	0.00	0.00	0.01	0.01	0.01	0.02	0.01	0.01	0.01	0.01	0.01	0.01	0.01	**0.01**	0.0046
Ca	0.02	0.03	0.10	0.02	0.01	0.01	0.01	0.01	0.02	0.08	0.04	0.08	0.03	0.02	**0.03**	0.0290
Na	0.06	0.04	0.03	0.02	0.04	0.03	0.04	0.00	0.04	0.02	0.03	0.03	0.01	0.02	**0.03**	0.0144
K	1.83	1.84	1.80	1.82	1.73	1.74	1.76	1.72	1.70	1.68	1.66	1.70	1.71	1.72	**1.74**	0.0556
Σ a-site	1.92	1.91	1.93	1.87	1.79	1.79	1.83	1.74	1.77	1.79	1.74	1.82	1.76	1.77	**1.82**	0.0637
Phl - Ib (embaying)			**(a.p.f.u)**												**Averages**	**SD (±)**
Si	5.96	6.02	6.00	5.91	5.94	5.91	5.87	6.02	5.93	5.90	5.94	5.91	5.84	5.81	**5.93**	0.0598
Fe^{3+}	0.23	0.14	0.23	0.25	0.16	0.10	0.15	0.17	0.29	0.21	0.16	0.17	0.22	0.27	**0.20**	0.0526
Al^{IV}	1.82	1.84	1.77	1.85	1.90	1.99	1.98	1.81	1.78	1.89	1.90	1.92	1.94	1.92	**1.88**	0.0670
Σ IV	8.01	8.00	8.00	8.01	8.00	8.00	8.00	8.00	8.00	8.00	8.00	8.00	8.00	8.00	**8.00**	0.0035
Al^{VI}	0.00	0.00	0.00	0.00	0.00	0.00	0.00	0.00	0.00	0.00	0.00	0.00	0.00	0.00	**0.00**	0.0000
Ti	0.16	0.16	0.17	0.17	0.17	0.17	0.17	0.16	0.16	0.15	0.16	0.16	0.16	0.15	**0.16**	0.0067
Cr	0.00	0.00	0.00	0.00	0.00	0.00	0.00	0.00	0.00	0.00	0.00	0.00	0.00	0.00	**0.00**	0.0000
Fe^{2+}	0.47	0.54	0.48	0.46	0.52	0.61	0.54	0.53	0.42	0.49	0.53	0.53	0.49	0.40	**0.50**	0.0520
Mn	0.00	0.01	0.00	0.01	0.00	0.00	0.00	0.01	0.01	0.00	0.00	0.00	0.00	0.00	**0.00**	0.0045
Mg	5.37	5.29	5.35	5.36	5.30	5.21	5.29	5.30	5.41	5.35	5.31	5.31	5.35	5.45	**5.33**	0.0565
Ni	0.00	0.00	0.00	0.00	0.00	0.00	0.00	0.00	0.00	0.00	0.00	0.00	0.00	0.00	**0.00**	0.0000
Σ VI	6.00	6.00	6.00	6.00	5.99	5.99	6.00	6.00	6.00	5.99	6.00	6.00	6.00	6.00	**6.00**	0.0041
Ba	0.05	0.05	0.05	0.05	0.05	0.05	0.04	0.05	0.06	0.05	0.06	0.05	0.04	0.04	**0.05**	0.0059
Ca	0.00	0.00	0.01	0.00	0.00	0.00	0.00	0.01	0.00	0.00	0.00	0.00	0.00	0.00	**0.00**	0.0035
Na	0.06	0.04	0.07	0.04	0.04	0.04	0.05	0.06	0.04	0.06	0.06	0.05	0.04	0.06	**0.05**	0.0103
K	1.78	1.75	1.79	1.73	1.77	1.79	1.78	1.75	1.82	1.76	1.74	1.78	1.75	1.75	**1.77**	0.0234
Σ a-site	1.89	1.84	1.92	1.82	1.86	1.88	1.87	1.87	1.92	1.87	1.86	1.88	1.83	1.85	**1.87**	0.0282
Phl - II (palmate)			**(a.p.f.u)**												**Averages**	**SD (±)**
Si	5.58	5.50	5.41	5.53	5.49	5.54	5.48	5.43	5.46	5.61	5.67	5.63	5.62	5.53	**5.53**	0.0759
Fe^{3+}	0.15	0.13	0.27	0.10	0.23	0.12	0.11	0.15	0.22	0.14	0.09	0.06	0.11	0.16	**0.15**	0.0563
Al^{IV}	2.27	2.37	2.32	2.37	2.29	2.34	2.41	2.42	2.32	2.25	2.24	2.32	2.27	2.30	**2.32**	0.0542
Σ IV	8.00	8.00	8.00	8.00	8.01	8.00	8.00	8.00	8.00	8.00	8.00	8.01	8.00	7.99	**8.00**	0.0046
Al^{VI}	0.00	0.00	0.00	0.00	0.00	0.00	0.00	0.00	0.00	0.00	0.00	0.00	0.00	0.00	**0.00**	0.0000
Ti	0.26	0.27	0.28	0.27	0.28	0.27	0.27	0.25	0.26	0.25	0.26	0.26	0.26	0.26	**0.26**	0.0090
Cr	0.00	0.00	0.00	0.00	0.00	0.00	0.00	0.00	0.00	0.00	0.00	0.00	0.00	0.00	**0.00**	0.0000
Fe^{2+}	0.49	0.51	0.41	0.55	0.43	0.52	0.52	0.53	0.43	0.52	0.58	0.57	0.55	0.50	**0.51**	0.0505
Mn	0.01	0.01	0.01	0.00	0.01	0.01	0.01	0.00	0.00	0.00	0.00	0.01	0.01	0.02	**0.01**	0.0059
Mg	5.24	5.21	5.30	5.17	5.28	5.20	5.20	5.21	5.31	5.22	5.16	5.15	5.19	5.23	**5.22**	0.0474
Ni	0.00	0.00	0.00	0.00	0.00	0.00	0.00	0.00	0.00	0.00	0.00	0.00	0.00	0.00	**0.00**	0.0000
Σ VI	6.00	6.00	6.00	5.99	6.00	6.00	6.00	5.99	6.00	5.99	6.00	5.99	6.01	6.01	**6.00**	0.0064
Ba	0.28	0.28	0.28	0.28	0.29	0.29	0.30	0.27	0.29	0.30	0.27	0.27	0.26	0.27	**0.28**	0.0116
Ca	0.00	0.00	0.01	0.00	0.01	0.00	0.01	0.01	0.00	0.00	0.01	0.01	0.00	0.00	**0.00**	0.0049
Na	0.05	0.06	0.09	0.06	0.06	0.08	0.07	0.05	0.03	0.07	0.08	0.08	0.06	0.06	**0.06**	0.0150
K	1.51	1.50	1.51	1.49	1.49	1.45	1.50	1.48	1.47	1.46	1.44	1.42	1.45	1.44	**1.47**	0.0281
Σ a-site	1.84	1.84	1.89	1.83	1.85	1.82	1.88	1.81	1.79	1.83	1.80	1.78	1.77	1.77	**1.82**	0.0362

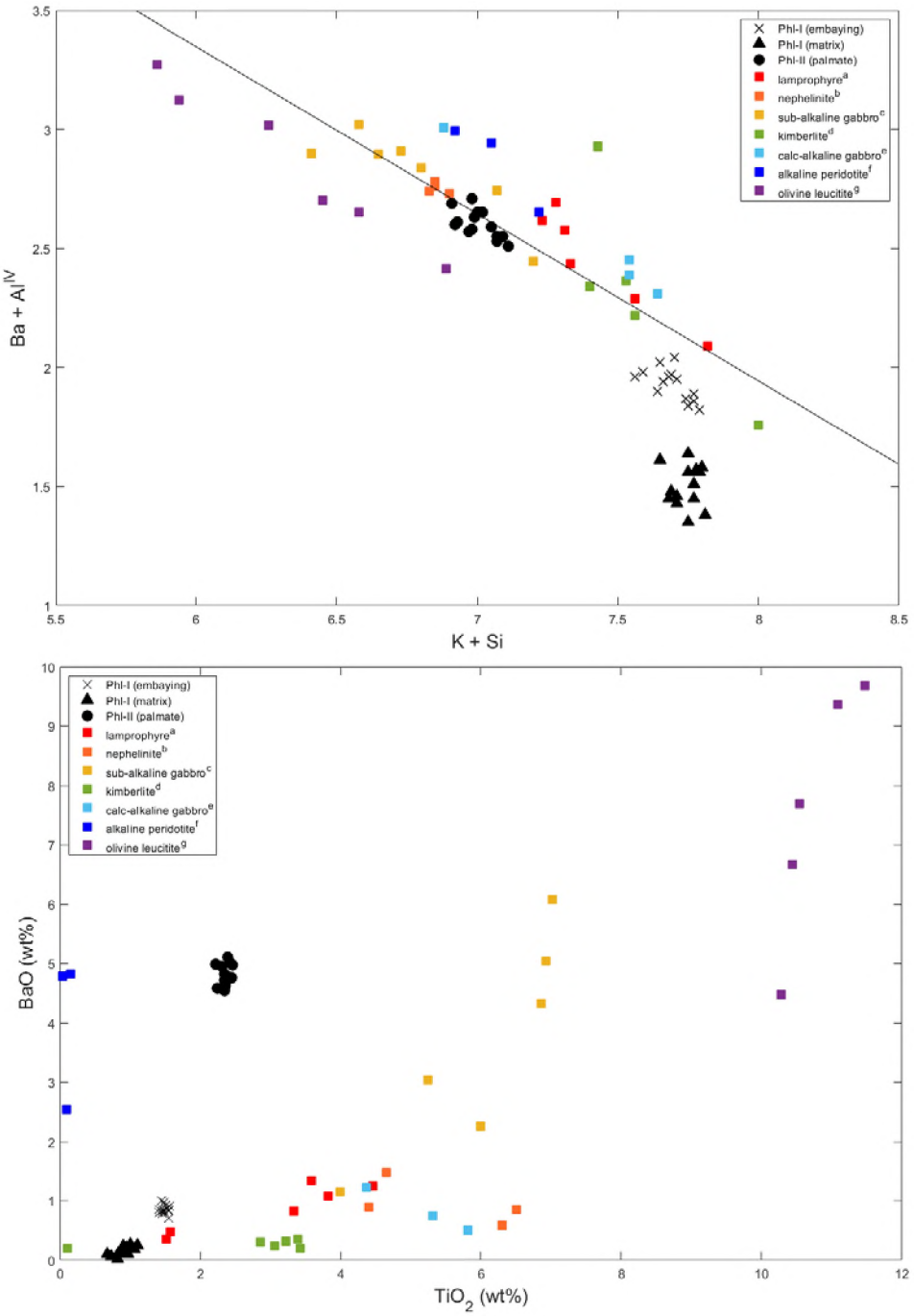

Figure 16: Phlogopite bivariate plots compared to phlogopite in other igneous rocks. Phlogopite cation substitution pairs (top) and trace elements (bottom) reflect metasomatic-magmatic evolution. Phlogopite from this study are compared to Ba-Ti-enriched biotites from metasomatic alteration ion-substitution from other studies: a) Owen, 2008; b) Ihbi et al., 2005; c) Shaw and Penczak, 1996; d) Arima, 1988; e) Bigi et al., 1993; f) Gaspar and Wyllie, 1982; g) Zhang et al., 1993. Ion pair substitution line based on Zhang et al., 1993.

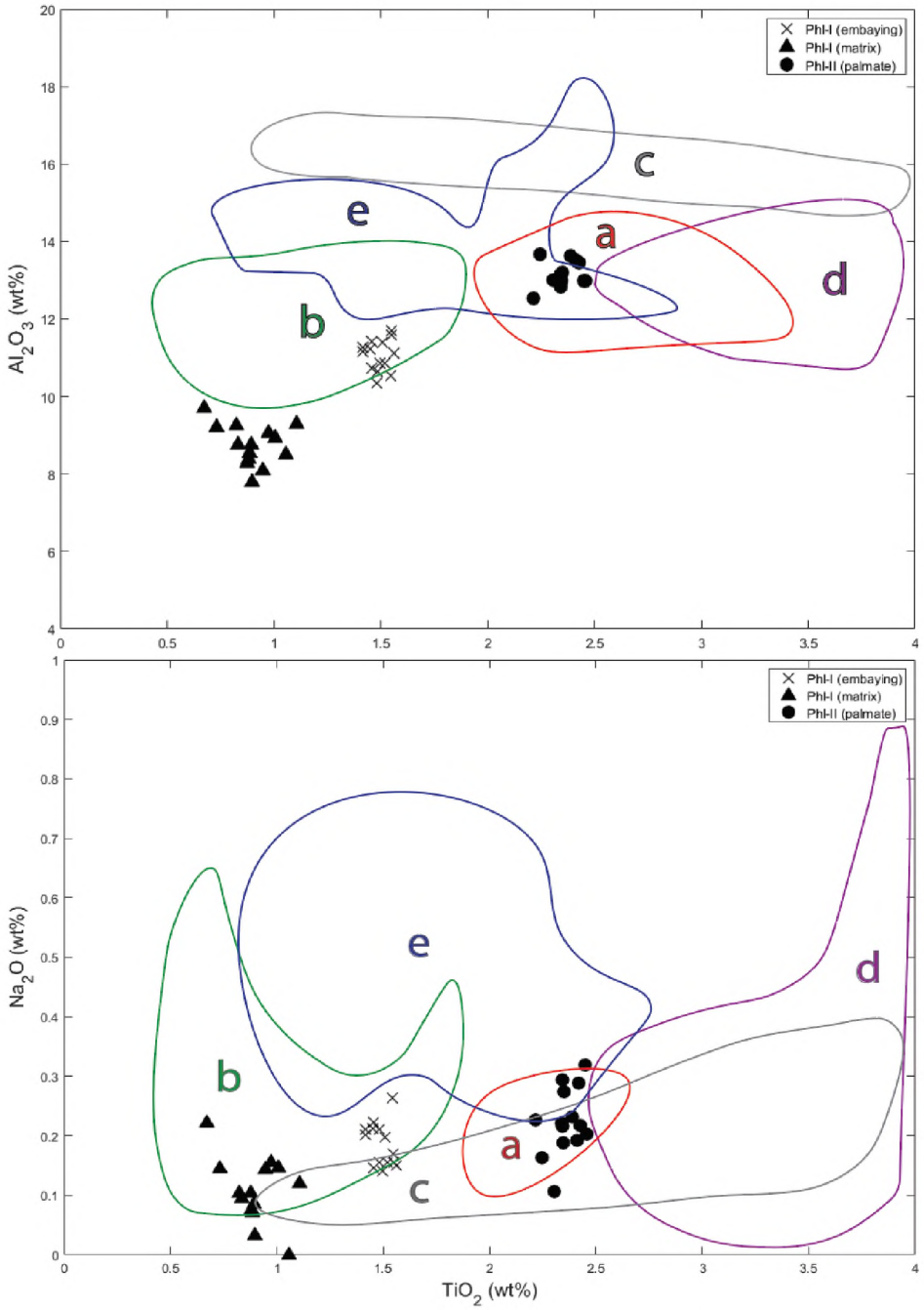

Figure 17: Elemental abundance bivariate diagram for phlogopite compared to phlogopite in other relevant igneous rocks. K-24 phlogopite is plotted with phlogopite from other kimberlite, mantle xenolith, and metasomatic assemblages (Kargin et al., 2019): a) phlogopite from late-kimberlite veinlets, b) phlogopite from metasomatized peridotite xenoliths, c) kimberlite groundmass, d) high Ti-Cr phlogopite from mantle xenoliths, e) phlogopite from carbonate veinlets in eclogite xenoliths.

A summary of petrographic features and compositional variations in phlogopite are shown in Table 9 and a quadrilateral biotite plot (Figure 18) confirms phlogopite compositions. Additional phlogopite bivariate plots are included in Appendix D.

Table 9: Phlogopite petrographic and chemical abundance variation.

Phlogopite	**Textural Features**	**OM Spatial Relations**	**K + Si (a.p.f.u)**	**Ba + Al^{IV} (a.p.f.u)**	**Ti (a.p.f.u)**	**Mg#**
Phl-Ia	Euhedral, moderate oxide amounts	Matrix, OM contacting	1.74 + 6.00 (7.74)	0.01 + 1.49 (1.50)	0.10	94.21
Phl-Ib	Euhedral-subhedral, rare/no oxides	Within OM channels	1.77 + 5.93 (7.70)	0.05 + 1.88 (1.93)	0.16	91.42
Phl-II	Anhedral, palmate, high oxide amounts	Matrix, OM rimming	1.47 + 5.53 (7.00)	0.28 + 2.32 (2.60)	0.26	91.13

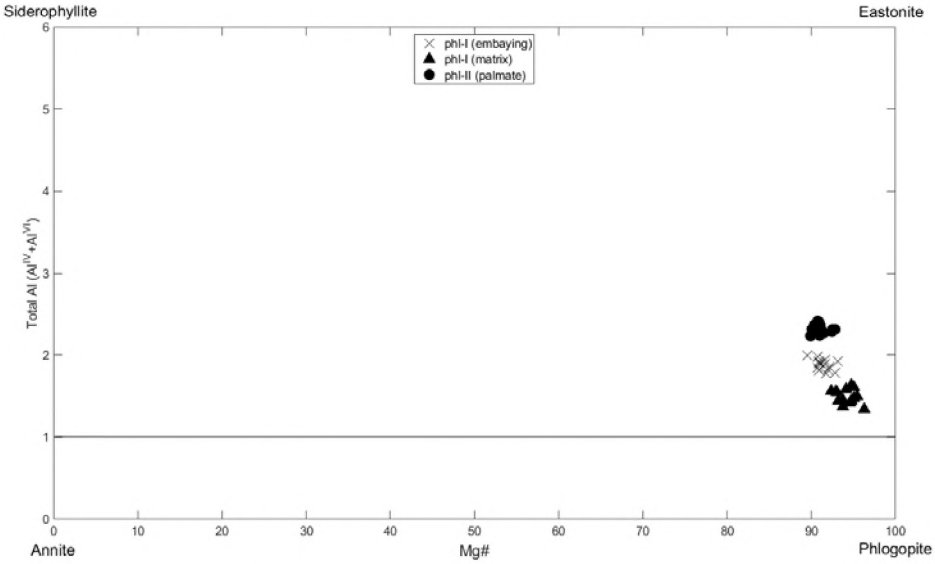

Figure 18: Biotite quadrilateral plot showing K-24 biotite plot as phlogopite.

7. DISCUSSION

Within the BHF-01-24 thin sections, key petrographic characteristics and observed mineral textures are indicators of multivariate phases of magmatic evolution. With geochemical data collected from distinctly different phlogopite groups determined from petrographic analysis, further support in constructing a comprehensive petrogenetic model of the K-24 diatreme is possible. Discussions and interpretations of petrographic and mineral chemistry observations and results are detailed in this section.

7.1. POIKILITIC TEXTURES

Poikilitic textures of minerals, where an older mineral species (chadacryst) is included in a different younger mineral (oikocryst), are indicative of the order of mineral crystallization in the magmatic evolution of igneous rocks due to differences in nucleation time and growth rates of two different mineral species as they begin to crystallize. (Wager et al., 1960, Mcbriney and Noyes, 1979, Barnes et al., 2016). In Figure 19, OM-IIIb is shown as an included chadacryst within a phl-I oikocryst. Additionally, phlogopite crystals are not included within OM domains themselves, only being present in channels. This evidence suggests that olivine formed before phlogopite and serpentinized rims in OM result from alteration of original olivine. Relict olivine contains no chadacrysts and therefore could reflect the earliest, near-liquidus phase mineral to have crystallized.

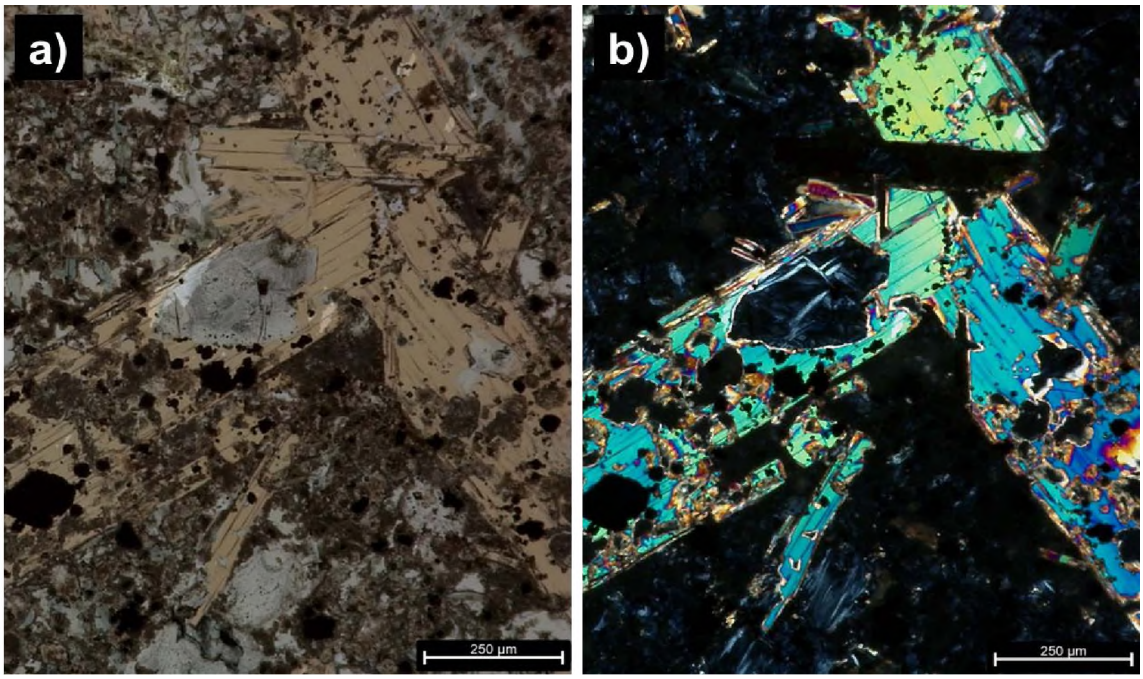

Figure 19: BHF-01-24-A.2 Phl-Ia with OM-IIIb chadacryst. Petrographic microscope images collected in plane-polarized light (19a) and cross-polarized light (19b) show distinct poikilitic textures of younger phlogopite crystallized around older OM-IIIb.

7.2. RELICT OLIVINE

Relict olivine clusters in OM are petrographically supported as primary in origin, not originating from peritectic or secondary re-crystallization as explained through petrographic differences distinguishing between the two (Erdmann et al., 2014). Little to no evidence of olivine being xenocrystic persists, as poikilitic observations and prior findings by Freeman, 2016, suggest relict olivine is the first mineral to form in the parent magma prior to or coinciding with the initial phase. Relict olivine within OM preserves the geochemical signature of the original mantle-derived magma source of the K-24 diatreme (i.e. Mg# / $Fo_{86.9}$-$Fo_{89.9}$, MgO wt% 46.9-48.2, variable Ni conc. range of 1600-3700 ppm) in which olivine crystallized earliest from the liquidus melt phase (Freeman, 2016). Petrographic evidence detailing euhedral relict olivine and phl-Ia phenocrysts

spatially associated further support pristine crystallization conditions, suggesting equilibria between the partial melt and source was present. Serpentinized rims of OM are in contact with early phlogopite, suggesting that olivine reacted with phl-Ia and phl-Ib prior to serpentinization but not necessarily after.

While outer rims of OM are serpentinized in the mid-phase of kimberlite magma ascent and in close spatial interaction with phl-II, relict olivine undergoes no distinct interactions with phlogopite after the initial euhedral generations (phl-Ia and phl-Ib). Late phlogopite (post-serpentinization event) would have been formed by the reaction of serpentine, not olivine. Mineral composition plots of relict olivine within OM reflect early magma conditions intrinsic to the mantle source, from a fertile, metasomatized peridotite which produced a partial melt in equilibrium, forming olivine and phlogopite as early phenocrysts from the liquidus (Section 7.3.).

7.3. EARLY PHLOGOPITE GENERATION (PHL-IA)

Mineral compositional data suggests phl-Ia was also derived from a partial melt of metasomatized peridotite (Kargin et al., 2019) as early, liquidus-phase phenocrysts. However, speculation on the specific reaction(s) involved in phl-Ia formation requires a better understanding of mineral assemblages of peridotite involved in the formation of the AAIP, which this study does not focus on. Nonetheless, a variety of destabilized reactants minerals in metasomatized peridotite are subjectable to reactions in which phlogopite is produced via the dissolution of minerals such as garnet, pyroxene, and other early magmatic minerals mentioned in other reactions (Aoki 1975, Van Achterburg 2001, Safonov and Butvina, 2016, and Kargin et al., 2019). Based on the lack of remaining

peridotite xenocrysts in the kimberlite melt, it can be reasonably inferred that a series of complex reactions in which garnet and pyroxene were completely depleted prior to the ascension of primary magma into the root zone, leaving components which formed phlogopite and minor accessory products in these reactions.

7.4. RAPID OLIVINE GROWTH AND PHL-IB FORMATION

Rounded mineral channels occur in dissolving olivine crystals due to a destabilizing event, either due to resorption or rapid mineral growth due to undercooling (Le Maitre et al., 2002, Vernon and Clarke, 2008). Morphological "channels" trend through pre-existing fractures or atomically weak-bonding interfaces where new product minerals form as a result of melt mixing reactions or, alternatively, by rapid growth rate due to large olivine content in melts followed by high eruption temperatures (Donaldson, 1976). Based on OM morphology (Figure 20), channels within OM show similarities to skeletal olivine dislocations resulting from rapid crystallization of kimberlite olivine in both experimental and microscopic studies (Donaldson, 1976, Jones et al., 2014, Venturi et al., 2020). This infers a period of rapid, bulk olivine crystallization which additionally marks phl-Ib crystallization from a slightly evolved magma. Slight enrichments in ion exchange pairs in phl-Ib from phl-Ia is explained through a later crystallization period where the generation of euhedral to subhedral phl-Ib, and thus the evolving magma, slowly diverged from pristine magmatic conditions.

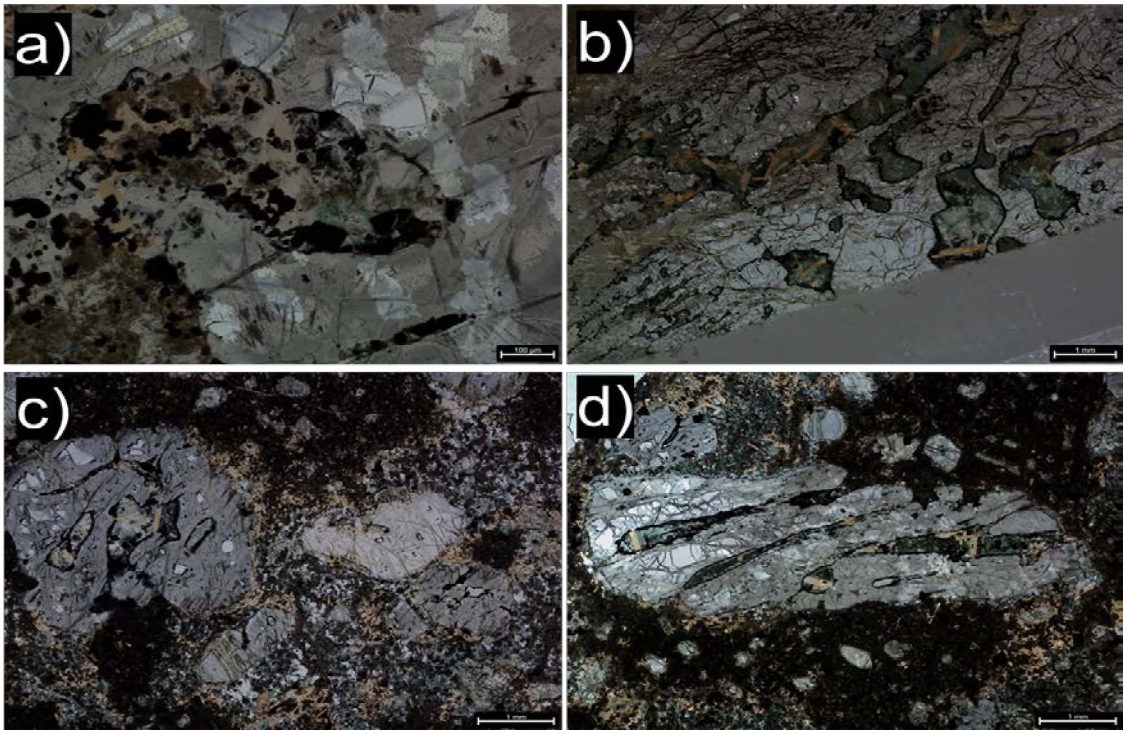

Figure 20: Various OM with skeletal morphology. Petrographic images (plane polarized) of BHF-01-24 thin sections show skeletal morphology defined by dislocation channels formed via rapid crystal growth. 20a) BHF-01-24-A.3 (magnified view of a dislocation channel), 20b) BHF-01-24-B.1 (multiple channels hosted in a single, large OM-I), 20c) BHF-01-24-D.3 (a variety of OM types hosting channels varying in size and degree of rapid growth), 20d) BHF-01-24-E.2 (long channels within an elongated OM-I).

7.5. SERPENTINIZATION VIA CARBONATE INFLUX

Clustered grouping of relict olivine in OM could offer insight into the degree of serpentinization each OM has undergone or simply be the result of sample-orientation when thin sections were cut and prepared. With complete serpentinization in OM-IIIa and OM-IIIb and varying degrees of serpentinization in OM-I and OM-II, the utility of these petrographic distinctions is mainly for classification purposes. As no relict olivine is found outside of serpentinized OM, it can also be inferred that OM void of relict olivine were completely serpentinized in a direct melt-dehydration reaction of primitive olivine.

Changes in modal x CO_2 / x H_2O from dehydration-induced serpentinization from either a single, volatile-rich melt or from the injection of a volatile-rich fluid is believed to be the cause of serpentinization and phreatomagmatic induction in the K-24 via the following reaction:

$$3Mg_2SiO_4 + \text{melt } [SiO_2 + 4H_2O] \rightarrow 2Mg_3Si_2O_5(OH)_4 \quad (1)$$

$$\text{(forsterite olivine) + [silica + water]} \rightarrow \text{(serpentine)}$$

Volatile-rich deuteric residua often form alongside serpentinization and carbonate crystallization in hypabyssal zones of kimberlite-forming magmas (Mitchell, 2008, Giuliani et al., 2017). Dehydration serpentinization of OM during magma ascent would result in an increase x CO_2 / x H_2O of the fluid and/or residual melt component associated with the rising magma.

7.6. MAGMACLASTS

Magmaclasts are sub-spherical clasts consisting of a central fragmented core with a juvenile rim and derive from volcaniclastic, silica-undersaturated, ultramafic, carbonatitic kimberlites resulting from volatile degassing-driven magmatic eruptions (Llyod and Stoppa, 2003, Gernon et al., 2012). Originally thought to be the result of rapid dissociation of immiscible fluids, recent research suggests that magmaclasts (formerly pelletal lapilli) form as a result of fluidized spray granulation of olivine amid eruptions in diatremes, representative of the interface between the erupting magma and volatile component (Gernon et al., 2012). The influence of multi-stage pulses of stalled magma within the root zone alongside volatile degassing via decompression and local variation in gas velocity within the diatreme, where the minimum gas flow rate required to induce

granulized fluidization was met, are responsible for developing distinct, features of magmaclasts (Figure 21). OM -I and OM-II closely share characteristics of magmaclasts formed via fluidized spray, most likely forming during rapid accent via eruption.

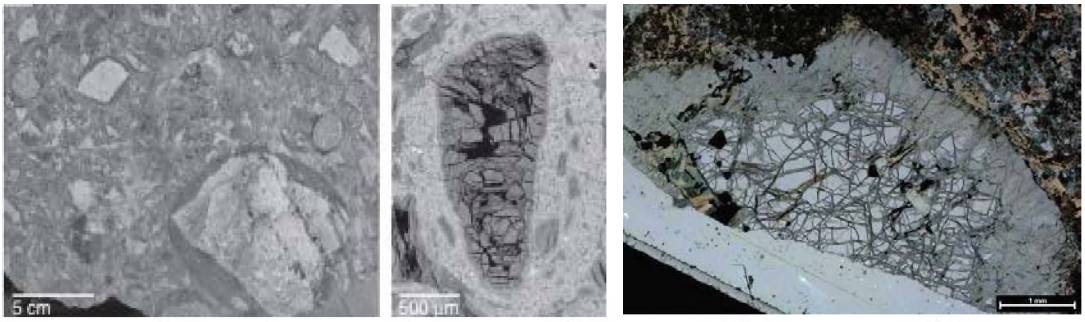

Figure 21: A side-by-side comparison of OM images from literature and this study. BSE images from Gernon et al. 2012 (left and middle) show magmaclasts formed via granulized fluid spray from a kimberlite magma compare with OM observed in plane polarized images of BHF-01-24-F.1 (right). Common features of both magmaclasts include oxide inclusions, fragmented central cores, and serpentinized rims, where no olivine zonation occurs.

7.7. PHLOGOPITE-II FORMATION

Phlogopite is a major mineral indicator of modal mantle and alkali metasomatism, especially in carbonatites and kimberlites, where parent melts are typically hydrous silicic to carbonatite enriched in H_2O, CO_2, alkali elements, and halogens (Ekka et al., 2018, Safonov et al., 2019). Major phase K-Ca-metasomatism occurs in phlogopite as a function of alkali exchange in rocks with moderate K_2O content (Deymar et al., 2018). Phlogopite is also known to interact with silicate wall-rock in typical magmatic genesis

of kimberlites with multiple pulses of magma prior to eruption (Shee, 1985, Giuliani et al., 2014, 2016).

Spatial association of serpentine, spinel, and phl-II suggests a potential reaction explaining the formation of phl-II amid the magmatic phase is possible, given the presence of either assimilated potassium oxide and silica from wall rocks and/or components directly from the kimberlite melt:

$$Mg_3Si_2O_5(OH)_4 + 3MgAl_2O_4 + K_2O + 4SiO_2 \rightarrow 2KMg_3AlSi_3O_{10}(OH)_2 + 2Al_2O_3 \quad (2)$$

(serpentine) + (spinel) + (potassium oxide) + (silica) → (phl-II) + (aluminum oxide)

Fluid-induced phlogopite (phl-II) undergo cation exchanges that parallel barian-titanian phlogopite enrichment in barium and aluminum (± titanium) cations while releasing potassium, silicon, and magnesium or iron (II) cations (Mansker et al., 1979; Arima, 1988; Bigi et al., 1993, Zhang et al., 1993; Shaw and Penczak, 1996; Ibhi et al., 2005; Guiliani et al., 2016; Kargin et al., 2019; Ventruti et al., 2020) due to an ion exchange pair that occurs in biotite crystal structures based on compatibility and charge balance by combination of one or more of the following reactions:

$$K^+ + Si^{4+} \rightarrow Ba^{2+} + {}^{IV}Al^{3+} \quad (3a)$$

$$(Mg^{2+}, Fe^{2+}) + 2\ OH^{-1} \rightarrow Ti^{4+} + 2O^{2-} \quad (3b)$$

$$Ba^{2+} + 3\ {}^{IV}Al^{3+} + 2Ti^{4+} \rightarrow K^+ + 3Si^{4+} + 3(Mg^{2+}, Fe^{2+}) \quad (3c)$$

Barium-enriched phlogopite in kimberlites preferentially crystallizes during a stalled batch period when multiple magma pulses in the root zone fail to erupt and/or after massive crystallization of olivine occurs under fast cooling conditions (Guiliani et al., 2016, Kargin et al., 2019, Ventruti et al., 2020). Residual CO_2 rich melt, with higher

concentrations of incompatible elements (e.g., Ba, Si, Al, etc.) or assimilation of felsic granitic basement, promotes crystallization of mid-late phase magmatic barium-enriched phlogopite (phl-II). Considering phlogopite rim reaction rates with olivine increase with bulk water content concentration (Grant et al., 2014), phl-II most likely crystallized after the stalled batch period in the root zone magma after rapid olivine crystallization (and phl-Ib crystallization) but continued ion substitution with incompatible elements through an additional, late-stage metasomatic process. Dissolution banding from Deymar et al., 2018 and irregular palmate porphyroblastic plate textures from Solov'eva et al., 2015 similarly appear in phl-II (Figure 22). These "autometasomatic" textures in phlogopite occur in late-stage carbonate-rich kimberlite paragenesis (Solov'eva et al., 2015).

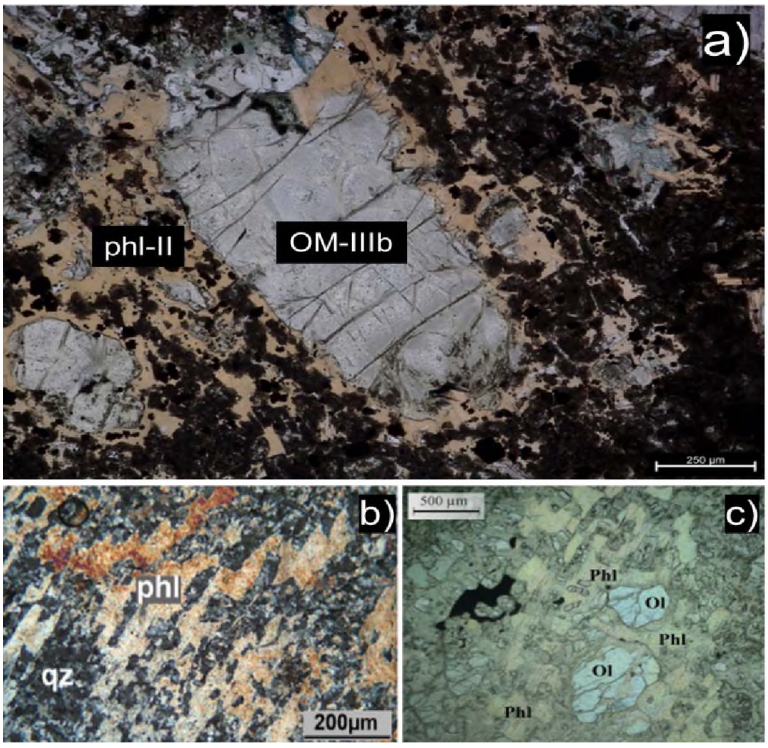

Figure 22: Images comparing phlogopite palmate porphyroblast textures. 22a) BHF-01-24-D.6, phl-II; 22b) Deymar et al., 2018; 22c) Solov'eva et al., 2015.

Lower BaO wt% and TiO_2 wt% abundance in phlogopite is more indicative of origination from metasomatized mantle peridotite (Gaspar and Wyllie, 1982, Owen, 2008) via subduction-generated fluids, which agrees with the geochemical disparity of these concentrations in phl-I compared to phl-II. Although phl-Ia and phl-Ib appear petrographically similar, there is a subtle difference in geochemical signatures between them. Higher barium, aluminum, and titanium enrichment in phl-II compared to phl-Ib and only slightly higher enrichments in phl-Ib compared to phl-Ia infers that phl-Ia and phl-Ib are early and mid-phase phenocrysts respectively, originating from a metasomatized mantle peridotite. The differences are explainable under the assumption that phl-Ib underwent slightly greater ion substitution during the stalled batch period where skeletal olivine formed due to rapid growth conditions providing the channel pathways in which phl-Ib crystallized. Phl-Ia and phl-Ib do not show metasomatic textures petrographically and chemically show low ion substitution related to late-stage metasomatism, suggesting the mechanism for late-metasomatic alteration occurring in phl-II must result separately from phl-Ia and phl-Ib crystallization. This key difference should explain the spatial relationship between phl-I contacts with OM and phl-II rim-reactions with OM and is evident of multiple generations of phlogopite.

8. PETROGENESIS

Based on petrographic and geochemical analysis, a model of the petrogenesis of the K-24 diatreme in the AAIP is proposed.

8.1. INITIAL-PHASE (MULTI-PULSE MAGMATISM)

Late-Devonian tectonics induced reactivation of pre-existing faults within the AAIP, providing conduits for magmatic ascension from the structurally weakened and fractured sub-continental lithosphere following regional geological fault-lines. A generated partial melt from variably metasomatized fertile peridotite rich in phlogopite (due to destabilization of mafic minerals) was in equilibrium before mobilizing further via decompression-driven ascension. During initial-phase magmatism, euhedral olivine (relict olivine) and phlogopite (phl-Ia) crystallized from the liquidus phase as magmatic phenocrysts while the partial melt mobilized into the root zone via a feeder dike. Due to a heterogeneous, low ratio of x CO_2 / x H_2O, magmatic mobilization of the magma fails and the initial pulse is unable to erupt or break through the hypabyssal facies, instead entering a stalled batch period in which multiple, failed pulses of magma remain entrained in the root zone (Sparks, 2013; Giuliani et al., 2016).

8.2. MID-PHASE (CARBONATE INFLUX AND ERUPTION)

The conduit is metasomatized as a result over this period of rapid olivine growth, where the magma does not reach phreatic levels until a carbonate influx event. During the mid-phase, rapid olivine growth develops skeletal morphology with variable amounts of "channels" in which dehydration of the evolving magma induces the formation of a secondary generation of euhedral-subhedral phlogopite (phl-Ib) within olivine channel margins. Serpentinization of olivine via magma dehydration may contribute to a carbonate influx, however the possibility of an intrusion of a carbonate-rich melt intrinsic to the mantle cannot be discounted as a contributor to the carbonate influx event which

enabled eruption. Whether by the modal depletion of H_2O or by magma mixing / fluid-melt injection, the introduction of significant CO_2 into the kimberlitic magma system induced gas exsolution led by a CO_2 gas propulsion front seeping upward through cracks to the surface. Pressurized quenching and deformation of the main kimberlite conduit and strata at the surface occurs (Sparks et al., 2006) while a shift from low to high x CO_2 / x H_2O re-mobilizes the stalled magma. CO_2 sequestration and solubility conditions in the kimberlite melt (Russell et al., 2012) procure the minimum gas flow required to develop a main transport gas front, which results in phreatomagmatic eruption. Prior to or during phreatomagmatic eruption, a final generation of phlogopite (phl-II) begins to crystallize via serpentine rim reactions incorporating either components present in the kimberlite magma or assimilated felsic material from basement rock as the magma travels through the hypabyssal zone.

8.3. LATE-PHASE (METASOMATISM AND EMPLACEMENT)

As the kimberlite magma is erupting, olivine magmaclasts (OM) form on ascent as an "aerosol" jet of granulated fluid sprays ejected melt material along the diatreme facies. Late-stage autometasomatism by residual CO_2-rich melt initiated throughout phl-II prior to and/or amid emplacement, producing porphyroblastic palmate, anhedral textures. The melt coalesced along the middle to lower diatreme margin along wall-rock while the rest of the erupted magma explosively breaches overlying strata toward the surface (Clement, 1975), forming the crater facies. Over a period of 386 million years, erosion of overlying strata exposed outcrops of dikes and diatreme rocks in the AAIP, including the K-24 alnöite, which this study has petrographically and geochemically investigated in an

attempt to understand the petrogenetic formation of the AUC diatreme complex from which it derives from beneath the surface.

8.4. FURTHER STUDIES

Detailed trace element analysis of relict olivine phenocrysts could be performed in manners similar to Nosova et al., 2018 to understand detailed magmatic evolution of olivine prior to OM formation in an attempt to understand more about the mantle source. Trends in trace element zonation across OM margins could be used to determine if magma mixing or fluid injection was present in the petrogenetic evolution profile, prompting the carbonate influx event. While this study has interpreted the morphology of OM channels to originate from skeletal deformation via rapid crystal, examining trace element consistency across channel margins would provide further support for rapid growth being the cause of channel formation within OM. In-depth studies of the birefringent differences between phl-I and phl-II could be performed to relate magmatic and autometasomatic mechanisms to optical differences between these two distinct generations of phlogopite. Additional work on volatile concentration within melt inclusions of the AAIP diatreme complex could further refine understanding the evolution of CO_2 and H_2O in respect to the petrogenesis of this study. Geochemical analyses and detailed petrography of minor and trace minerals in the K-24 alnöite, mainly oxides and chlorite, can be expanded upon in further studies to provide more detailed constraints on the petrogenesis of this diatreme complex based on the roles of these minerals in main mineral (olivine and phlogopite) formation.

REFERENCES

Aoki, K., Origin of phlogopite and potassic richterite bearing peridotite xenoliths from South Africa. *Contributions to Mineralogy and Petrology* (1975), 53, 145-156.

Arima, M., Barium-rich phlogopite in a mantle derived xenolith of the Upper Canada Mine kimberlite, Ontario, Canada: implications for Ba-resevoir in the upper mantle. *J. Min. Petr. Econ. Geol.* (1988), 88, 217-231

Barnes, J.S., Mole, D.R., Le Vaillant, M., Campbell, M.J., Verrall, M.R., Roberts, M.P., Evans, N.J., Poikilitic Textures, Heteradcumulates and Zoned Orthopyroxenes in the Ntaka Ultramafic Complex, Tanzania: Implications for Crystallization Mechanisms of Oikocrysts, *Journal of Petrology*, Volume 57, Issue 6, June 2016, Pages 1171–1198

Bigi, S., Brigatti, M.F., Mazzuchelli, M., Rivalenti, G., Crystal chemical variations in Ba-rich biotites from gabbroic rocks of lower crust (Ivrea Zone, NW Italy). *Contributions to Mineralogy and Petrology,* (1993), 113, 87-99

Brooker, R.A., Kjarsgaard, B.A., 2011. Silicate-carbonate liquid immiscibility and phase relations in the system SiO2-Na2O-Al2O3-Cao-Co2 at 0.1-2.5 GPa with applications to carbonatite genesis. J. Petrol. 52, 1281–1305.

Clement, C.R., The emplacement of some diatreme-facies kimberlites. *Physics and Chemistry of the Earth* (1975), pg 51-59.

Clement, C.R., Skinner, E.M.W., Smith, B.H.S. (1984). Kimberlite Redefined. *The Journal of Geology,* 92(2), 223-228.

Clendenin, C. W., Niewendorp, C. A., Lowell, G. R.; Reinterpretation of faulting in southeast Missouri. *Geology* 1989; 17 (3): 217–220.

Cox, R.T., Ouachita, Appalachian, and Ancestral Rockies deformations recorded in mesoscale structures on the foreland Ozark Plateaus, Tectonophysics, Volume 474, Issues 3–4, 2009, p. 674-683

Csontos, R., and Van Arsdale, R., 2008, New Madrid seismic zone fault geometry, *Geosphere* vol. 4, p. 802-813.

Currie, C.A., Beaumont, C., Are diamond-bearing Cretaceous kimberlites related to low-angle subduction beneath western North America? *Earth and Planetary Science Letters* (2011), 303, 1-2, pg. 59-70.

Deymar, S., Yazdi, M. & Rezvanianzadeh, M., Behzadi, Me., Alkali metasomatism as a process for Ti–REE–Y–U–Th mineralization in the Saghand Anomaly 5, Central Iran: Insights from geochemical, mineralogical, and stable isotope data. (2018) Ore Geology Reviews.

Donaldson, C.H., An experimental investigation of olivine morphology, *Contributions to Mineralogy and Petrology* (1976), 57, 187-213

Ekka, M.A., Prasad, J., Bhattacharya, D.K., Occurrence of phlogopite in carbonatite and associated alkaline rocks at Beldih, Purulia District, West Bengal, India. *International Journal of Engineering Science Invention* (2018), 2319-6726, Vol. 7, Is. 4, pg. 06-10

Erdmann, S., Scaillet, B., Martel, C., Cadoux, A., Characteristic textures of recrystallized peritectic, and primary magmatic olivine in experimental samples and natural volcanic rocks. *Journal of Petrology* (2014), vol. 55, no. 12, pg. 2377-2402

Freeman, Z.W., "Avon Alkaline Igneous Province, Missouri: Characterization of subcontinental mantle source and evolution via chemical analysis of olivine" (2016). Masters Theses. 7737.

Foley, S.F., Prelevic, D., Rehfeldt, T., Jacob, D.E., Minor and trace elements in olivines as probes into early igneous and mantle melting processes. *Earth and Planetary Science Letters* (2013), 363, 181-191

Gaspar, J.C., Wyllie, P.J., Barium phlogopite from the Jacupiranga carbonatite, Brazil. *American Mineralogist* (1982), 67 (9-10): 997-1000.

Gernon, T.M., Brown, R.J., Tait, M.A., Hincks, T.K., The origin of pelletal lapilli in explosive kimberlite eruptions. Nat Commun 3**,** 832 (2012).

Giuliani, A., Phillips, D., Kamenetsky, V.S., Kendrick, M.A., Wyatt, B.A., Goeman, K., Hutchison, G., Petrogenesis of Mantle Polymict Breccias: Insights into Mantle Processes Coeval with Kimberlite Magmatism, *Journal of Petrology*, 2014, Volume 55, Issue 4, Pages 831–858.

Giuliani, A., Phillips, D., Kamenetsky, V.S., Goemann, K., Constraints on kimberlite ascent mechanisms revealed by phlogopite compositions in kimberlites and mantle xenoliths. *Lithos*, 240–243 (2016), pp. 189-201

Giuliani, A., Soltys, A., Phillips, D., Kamenetsky, V.S., Maas, R., Goemann, K., Woodhead, J.D., Drysdale, R.N., Griffin, W.L., The final stages of kimberlite petrogenesis: Petrography, mineral chemistry, melt inclusions and Sr-C-O isotope geochemistry of the Bultfontein kimberlite (Kimberley, South Africa), *Chemical Geology* (2017), 455, 342-356.

Grant, T. B., Milke, R., Wunder, B.,Wirth, R., Rhede, D., Experimental study of phlogopite reaction rim formation on olivine in phonolite melts: Kinetics, reaction rates, and residence times: American Mineralogist (2014) 99 (11-12): 2211-2226

Harrison, R.W., and Shultz, A., 2002, Tectonic framework of the southwestern margin of the Illinois basin and its influence on neotectonism and seismicity: Seismological Research Letters, v.73, p.689-731

Herzberg, C., Lithosphere peridotites of the Kaapval craton, *Earth and Planetary Science Letters* (1993), 120, 1-2, 13-19.

Herzberg, C., Identification of Source Lithology in the Hawaiian and Canary Islands: Implications for Origins, Journal of Petrology (2011), Volume 52, Issue 1, pg. 113–146

Ibhi, A., Nachit, H., El Abia, H., Titanium and barium incorporation into the phyllosilicate phases: The example of phlogopite-kinoshitalite solid solution. *J. Phys. IV France,* 123 (2005) 331-335.

Jelsma, H., Barnett, W., Richards, S., Lister, G., Tectonic setting of kimberlites. Lithos, 112 (2009), pp. 155-165

Jones, T.J., Russell, J.K., Porritt, L.A., Brown, R.J., Morphology and surface features of olivine in kimberlite: implications for ascent processes. *Solid Earth* (2014), 5, 313-326

Kargin, A.V., Sazonova, L.V., Nosova, A.A., Lebedeva, N.M., Kostitsyn, Yu.A., Kovalchuk, E.V., Tetryachenko, V.V., Tikhomirova, Ya.S., Phlogopite in mantle zenoliths and kimberlite from the Grib pipe, Arkhangelsk province, Russia: Evidence for multi-stage mantle metasomatism and origin of phlogopite in kimberlite. *Geoscience Frontiers* 10 (2019) 1941-1959

Kidwell, A. L. (1947), Post-Devonian Igneous Activity in Southeastern Missouri, edited by M. D. o. B. a. Administration, Jefferson City, MO

Kostrovitsky, S. I., *Physical Conditions, Hydraulics and Kinematics of Emplacement of Kimberlite Pipes* 1–95 (Nauka, Novosibirsk, 1976)

Le Bas, M., Streckeisen, A., 1991. The IUGS systematics of igneous rocks. Journal of the Geological Society, London 148, 825-833.

Le Maitre, R. W., Streckeisen, A., Zanettin, B., Le Bas, M. J., Bonin, B., Bateman, P., & Lameyre, J. (2002). Igneous rocks. A classification and glossary of terms, 2. Cambridge University Press.

Liu, Chao, "Origin of Periclines in the Ozark Plateau, Missouri: A field and numerical modeling" (2019). *Doctoral Dissertations*. 2818.

Llyod, F., Stoppa, F., (2003) Pelletal lapilli in diatremes – some inspiration from the old masters. Geolines. 15. 65-71.

Lorenz, V., (2003) Maar-diatreme volcanoes, their formation, and their setting in hard-rock or soft-rock environments. Geolines 15, 72–83.

Mansker, W.L., 1973. Petrology of a Southeastern Missouri Ultramafic Pipe. University of Missouri.

Mansker, W.L., Ewing, R.C., Keil, K., Barian-titanian biotites in nephelinites from Oahu, Hawaii. *American Mineralogist* (1979), 64, 156-159.

Marshak, S., Paulsen, T., 1996; Midcontinent U.S. fault and fold zones: A legacy of Proterozoic intracratonic extensional tectonism?. *Geology* ; 24 (2): 151–154.

Marshak, S., Paulsen, T., 1997; Structural Style, Regional Distribution, and Seismic Implications of Midcontinent Fault-and-Fold Zones, United States. *Seismological Research Letters* ; 68 (4): 511–520.

Marshak S., Karlstrom K., Timmons, J.M., 2000, Inversion of Proterozoic extensional faults: An explanation for the pattern of Laramide and Ancestral Rockies intracratonic deformation, United States: Geology, v. 28, p.735-738

Marshak, S., Nelson, W.J., McBride, J.H., 2003, Phanerozoic strike-slip faulting in the continental interior platform of the United States: examples from the Laramide Orogen, Midcontenent, and Ancestral Rocky Mountains: Geological Society, London, Special Publications, v. 210, p. 159-184.

Mcbirney, A.R., Noyes, R. M., Crystallization and Layering of the Skaergaard Intrusion, *Journal of Petrology*, Volume 20, Issue 3, August 1979, Pages 487–554

McBride, J. H., Nelson, J.W., Style and origin of mid-Carboniferous deformation in the Illinois Basin, USA - Ancestral Rockies deformation?, Tectonophysics, Volume 305, Issues 1-3, 1999, pg. 249-273

Menuge, J.F., Brewer, T.S., Seeger, C.M., Petrogenesis of metaluminous A-type rhyolites from the St Francois Mountains, Missouri and the Mesoproterozoic evolution of the southern Laurentian margin. (2002) Precambrian Research. vol. 113, 3-4. pg 269-291.

Mitchell, R.H., Kimberlites: Mineralogy, Geochemistry, and Petrology. Plenum Press, London & New York (1986).

Mitchell, R.H., Petrology of hypabyssal kimberlites: Relevance to primary magma compositions. J. Volcanol. Geoth. Res., 174 (1) (2008), pp. 1-8

Morgavi D., Arienzo I., Montagna C., Perugini D., Dingwell D.B. (2017) Magma Mixing: History and Dynamics of an Eruption Trigger. In: Gottsmann J., Neuberg J., Scheu B. (eds) Volcanic Unrest. Advances in Volcanology. Springer, Cham. ISBN: 978-3-319-58412-6

Murphy, J. & Keppie, John. (2005). The Acadian Orogeny in the Northern Appalachians. International Geology Review. 47. 663-687.

Nelson, W.J, Lumm, D.K., Schwalb, H.R., Ste. Genevieve fault zone, Missouri and Illinois. Office of Nuclear Regulatory Research, Division of Radiation Programs and Earth Sciences, Washington, D.C. (1985)

Nosova, A.A., Sazonova, L.V., Kargin, A.V., Smirnova, M.D., Lapin, A.V., Shcherbakov, V.D., Olivine in ultramafic lamprophyres: chemistry, crystallization, and melt sources of Siberian pre- and post-trap aillikites. *Contributions to Mineralogy and Petrology* (2018), 173:55

Owen, J.P., Geochemistry of lamprophyres from the Western Alps, Italy: implications for the origin of an enriched isotopic component in the Italian mantle. *Contributions to Mineralogy and Petrology* (2008), 155:341-362

Potter, N.J., Kamenetsky, V.S., Simonetti, A., Goemann, K., Different types of liquid immiscibility in carbonatite magmas: A case study of the Oldoinyo Lengai 1993 lava and melt inclusions. *Chemical Geology* (2017), 455, 376-384

Rock, N.M.S., The Nature and Origin of Ultramafic Lamprophyres: Alnöites and Allied Rocks. *Journal of Petrology* (1986), 27, 1, 155-196.

Rosenbusch H. (1887) Mikroskopische Physiographie, 2nd edition. Schweizerbart, Stuttgart, pg. 805

Russell, J.K., Porritt, L.A., Lavallée,Y., Dingwell, D.B., Kimberlite ascent by assimilation-fuelled buoyancy. Nature, 481 (7381) (2012), pp. 352-356

Safonov, O.G., Butvina, V.G. Indicator reactions of K and Na activities in the upper mantle: Natural mineral assemblages, experimental data, and thermodynamic modeling. *Geochem. Int.* 54, 858–872 (2016).

Safonov, O., Buvina, V., Limanov, E., Phlogopite-forming reactions as indicators of metasomatism in the lithospheric mantle (2019) Minerals 2019, 9, 685

Singewald, J. T., and Milton, C., 1930, An alnöite pipe, its contact phenomena, and ore deposition near Avon, Missouri: The Journal of Geology, vol. 38, p. 54-66

Shavers, E.J., Ghulam, A., Encarnacion, J., Bridges, D.L., Luetkemeyer, P.B., Carbonatite associated with ultramafic diatremes in the Avon Volcanic District, Missouri, USA: Field, petrographic, and geochemical constraints (2016) Lithos, 248-251, pp. 506-516.

Shavers, E.J., Ghulam, A., Hartling, S., Emplacement of ultramafic-carbonatite intrusions along reactivated North American mid-continent rift structures (2017) Tectonophysics, 712-713

Shavers, E.J., Ghulam, A., Encarnacion, J., Surface alteration of a melilitite-clan carbonatite and the potential for remote carbonatite detection (2018) Ore Geology Reviews, 92, pp. 19-28.

Shaw, C.S.J., Penczak, R.S., Barium and titanium-rich biotite and phlogopite from the western and eastern gabbro, Coldwell alkaline complex, northwestern Ontario. *The Canadian Mineralogist* (1996), 34 (5): 967-975

Shee, S. (1985) The petrogenesis of the Wesselton Mine kimberlites, Kimberley, Cape Province, R.S.A. Unpublished PhD Thesis, University of Cape Town, p. 220.

Solov'eva, L.V., Kalashnikova T.V., Kostrovitsky S.I., Ivanov A.V., Matsuk S.S., Suvorova L.F., Metasomatic and magmatic processes in the mantle lithosphere of the Birekte Terrain of the Siberian Craton and their effect on the lithosphere evolution. *Geodynamics & Tectonophysics*. 2015; 6(3):311-344

Sparks, R.S.J., Baker, L., Brown, R.J., Field, M., Schumacher, J., Stripp, G., Walters, A., 2006. Dynamical constraints on kimberlite volcanism, Journal of Volcanology and Geothermal Research, Volume 155, Issues 1-2, pg. 18-48.

Sparks, R.S.J., Kimberlite Volcanism. *Annual Review of Earth and Planetary Sciences* (2013), Vol. 41:497-528

Thompson, T.L., 1995. The Stratigraphic Succession in Missouri. Rolla, Missouri.

Timmons, J.M., Karlstrom, K.E., Dehler, C.M., Geissman, J.W., Heizler, M.T., Proterozoic multistage (ca. 1.1 and 0.8 Ga) extension recorded in the Grand Canyon Supergroup and establishment of northwest- and north-trending tectonic grains in the southwestern United States. *GSA Bulletin* 2001; 113 (2): 163–181.

Tuttle, M.P., Schweig, E.S., Sims, J.D., Lafferty, R.H., Wolf, L.W., Haynes, M.L., The Earthquake Potential of the New Madrid Seismic Zone. *Bulletin of the Seismological Society of America* 2002; 92 (6): 2080-2089

Van Achterberg, E., Griffin, W.L., Stiefenhofer, J., Metasomatism in mantle xenoliths from the Letlhakane kimberlites: estimation of element fluxes. *Contributions to Mineralogy* (2001), 141: 397-414

Van Arsdale, R., Pryne, D., Woolery, E., Northwestern Extension of the Reelfoot North Fault Near New Madrid, Missouri. *Seismological Research Letters* 2013; 84 (6): 1114–1123.

Van Schmus, W.R., Hinze, W.J., The Midcontinent Rift System, Annual Review of Earth and Planetary Sciences 1985 13:1, 345-383

Ventruti, G., Caggianelli, A., Festa, F., Langone, A., Crystal chemistry of barian titanian phlogopite from a lamprophyre of the gargano promontory (Apulia, Southern Italy), *Minerals* 2020, 10(9), 766.

Vernon, R. H. & Clarke, G. L. (2008): Principles of Metamorphic Petrology. Cambridge University Press.

Wager, L.R., Brown, G.M., Wadsworth, W.J., Types of Igneous Cumulates, *Journal of Petrology*, Volume 1, Issue 1, February 1960, Pages 73–85

Wilson, L., Head III, J. An integrated model of kimberlite ascent and eruption. *Nature* 447, 53–57 (2007).

Zartman, R.R., Brock, M.R., Heyl, A.V., and Thomas H.H., K-Ar and Rb-Sr ages of some Alkalic Intrusive Rocks from the Central and Eastern United States. American Journal of Science, 1967, 265 (10) 848-870

Zhang, M., Suddaby, P., Thompson, R.N., Dungan, M.A., Barian titanian phlogopite from potassic lavas in northeast China: Chemistry, substitutions, and paragenesis. *American Mineralogist* (1993), Vol. 78, pg. 1056-1065.

SECTION

2. CONCLUSION

Petrographic and geochemical characterization of olivine and phlogopite in a late-Devonian diatreme-facies alnöite (K-24) from the Avon Alkaline Igneous Province (AAIP) provided considerable insight towards constraining the petrogenesis of one of the only Devonian-age igneous complexes in the mid-continent. Petrographic textural and spatial analysis and geochemical data regarding differences in phlogopite crystals enabled the discernment of multiple phlogopite generations within the alkaline-ultramafic-carbonatite (AUC) diatreme complex from which the K-24 alnöite formed. Applying the same methods toward understanding the complex role of olivine within olivine magmaclasts in context of the development of the diatreme further enabled its petrogenetic evolution to be constrained. Implications for deciphering how this igneous complex was generated could constitute broader understanding of the many persisting mysteries regarding formation of diatremes and enigmatic igneous processes within the mantle around the world.

The petrogenesis of the K-24 alnöite begins with a decompression-driven magma mobilization event 386 $\pm$ 1 ma (Freeman, 2016) within metasomatized peridotite beneath the AAIP. From this partial melt, homogenous euhedral olivine and the first generation of phlogopite (phl-Ia) crystallize from the liquidus as the rising magma ascended through a feeder dike into the root zone of the conduit. Multiple magmatic pulses during a stalled batch period with low x CO_2 / x H_2O lead to the rapid growth of olivine crystals, inducing

skeletal structures and providing margins for which a mid-phase phlogopite generation (phl-Ib) could occupy. Pressure quenching of olivine followed by serpentinization via dehydration of the melt contributed to an influx in x CO_2 / x H_2O in the stalled magma. As CO_2 exsolves, prompting a transport gas front, the magma undergoes remobilization via eruption through the hypabyssal zone and expanding conically upward through the diatreme facies, creating olivine magmaclasts textures and a final, late generation of phlogopite (phl-II). An aerosol spray of rising magma coalesced along the diatreme facies wall-rock while the rest of the magma blasted upward to the surface. Late-stage autometasomatism of late-generated phlogopite via CO_2 -rich residual melt resulted in palmate porphyroblast textures and secondary mineral crystallization (carbonates within veinlets). Over time, the exposure of the K-24 alnöite at the surface enabled its collection and study, revealing that pristine mantle signatures were only preserved in relict olivine amid a complex petrogenetic evolution of the diatreme below the AAIP.

APPENDIX A.

COMPREHENSIVE PETROGRAPHIC ANALYSIS

Table A.1: Comprehensive petrographic analysis of K-24 thin sections (BHF-01-24.A-F)

	Ave Olv Size (mm)	Olv Grouping	Ave Phl Size (mm)	Phl shape	Phl Grouping	Spatial Relationship	Oxide Relationship
A.1	3.125	Consolidated	0.678	Subhedral	Cross-Cutting	Contact	Included & rimming
A.2	OM only		0.773	Euhedral	Cross-Cutting	Full-Rimming	Included & rimming
A.3	0.104	Fragmented	0.0435	Anhedral	Ambiguous	Embayed	Embayed, included, & rimming
A.4	3.222	Consolidated	0.7185	Euhedral	Cross-Cutting	Contact	Rimming, included in only phl
A.5	4.2165	Consolidated	0.755	Anhedral	Ambiguous	Contact	Rimming, embayed, included only in phl
B.1	6.4465	Consolidated	0.3425	Euhedral	Ambiguous	Embayed	Rimming, embayed, included only in olv
B.2	OM only		0.27	Subhedral	Ambiguous	Rimmed & embayed	Rimming, embayed, included only in phl
B.3	3.0925	Consolidated	0.27	Anhedral	Ambiguous	Rimmed & embayed	Rimming, embayed, included only in phl
B.4	3.4015	Consolidated	1.684	Subhedral	Cross-Cutting	Rimmed & embayed	Embayed, included, & rimming
C.1	0.745	Fragmented	0.325	Euhedral	Cross-Cutting	Rimmed & embayed*	Embayed, included, & rimming
C.2	0.2455	Fragmented	---	Anhedral	Sparse	Contact	Embayed, included, & rimming
C.3	OM only		0.2715	Euhedral	Cross-Cutting	Contact	Included & rimming
D.1	2.645	Consolidated	0.6315	Subhedral	Cross-Cutting	Rimmed & embayed	Embayed, included, & rimming
D.2	0.186	Solo				Isolated	Included & rimming
D.3	OM only	Fragmented	0.23	Subhedral	Cross-Cutting	Rimmed & embayed	Embayed, included, & rimming
D.4	4.43	Consolidated	0.235	Subhedral	Ambiguous	Rimmed & embayed	Embayed, included, & rimming
D.5	OM only	Fragmented	0.1455	Subhedral	Ambiguous	Embayed	Embayed, included, & rimming
D.6	OM only	Consolidated	---	Anhedral	Ambiguous	Full-Rimming	Included & rimming
D.7	0.0465	Solo	0.0575	Subhedral	Ambiguous	Isolated	Engulfing (anomaly)
E.1	1.81	Fragmented	1.44	Subhedral	Cross-Cutting	Contact	Included & rimming
E.2	1.065	Consolidated	0.195	Subhedral	Ambiguous	Rimmed & embayed	Embayed, included, & rimming
E.3	4.825	Consolidated	0.18	Subhedral	Ambiguous	Rimmed & embayed	Embayed, included, & rimming
E.4	1.225	Consolidated	0.79	Euhedral	Cross-Cutting	Contact	Embayed, included, & rimming
F.1	3.17	Consolidated	0.215	Subhedral	Cross-Cutting	Rimmed & embayed	Embayed, included, & rimming
F.2	OM only		0.3111	Euhedral	Cross-Cutting	Contact	Included & rimming
F.3	0.613		---	Anhedral	Ambiguous	Contact	Included & rimming

The comprehensive petrographic analysis of the K-24 alnöite (Table A.1) includes specified features noted in zones across each thin section. Trends developed from observations of thin section minerals enabled categorization of features and inevitably classification of OM and phlogopite. This also led to developing inquiries to discern the origin of specific mineral features and provided tangible evidence for petrogenetic events resulting in the diverse array of textural and spatial characteristics within OM and phlogopite. In addition, full plane polarized, and cross polarized light microscopic image sets taken from petrographic microscopy of the BHF-01-24 thin sections are included below:

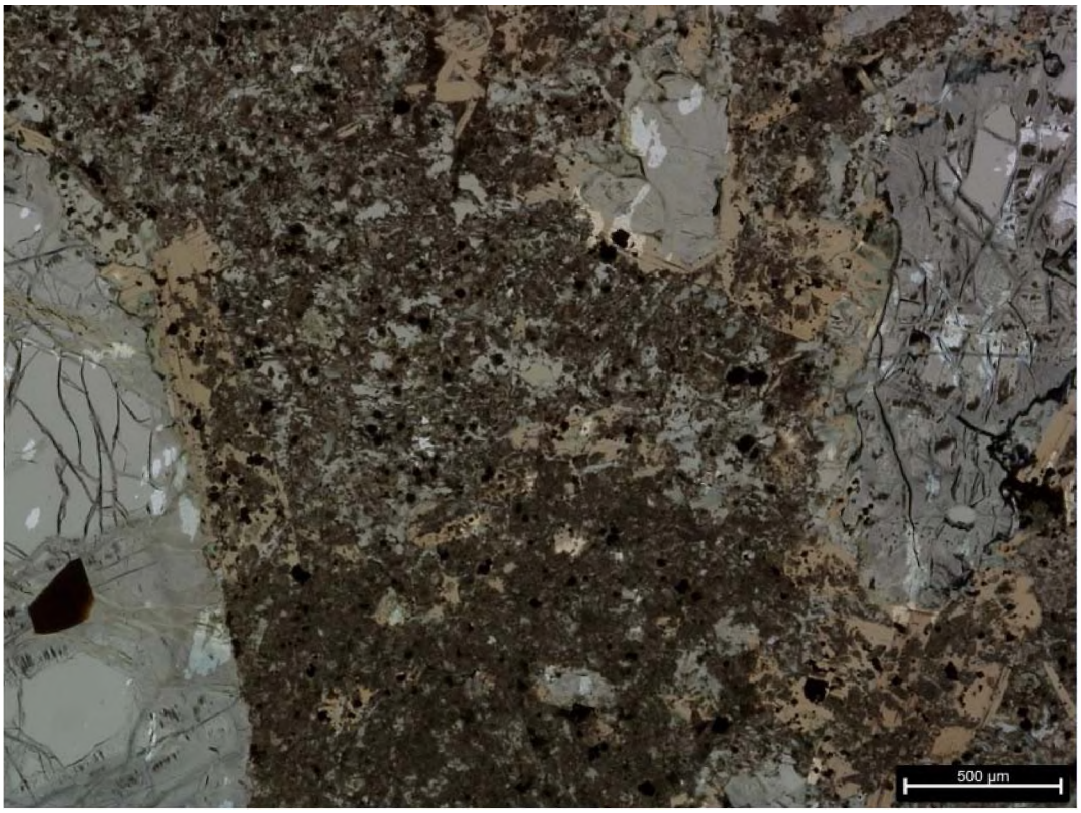

Figure A.1.: BHF-01-24-A.1 plane polarized light

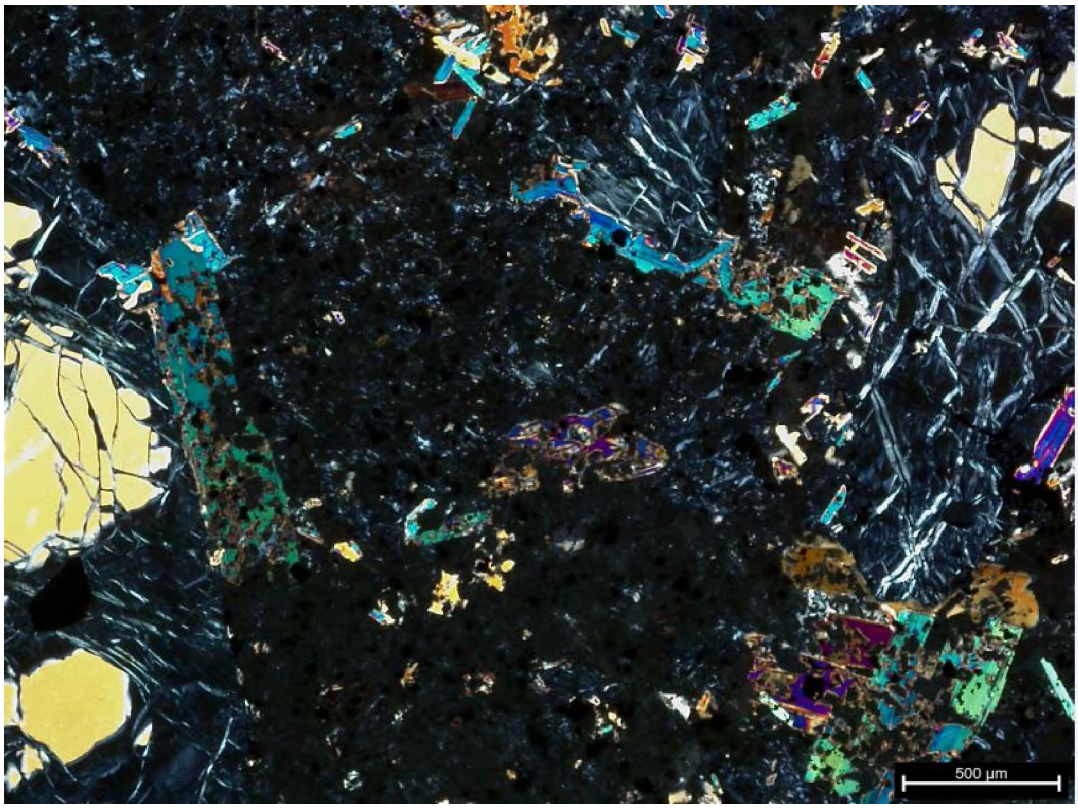

Figure A.2.: BHF-01-24-A.1 cross polarized light

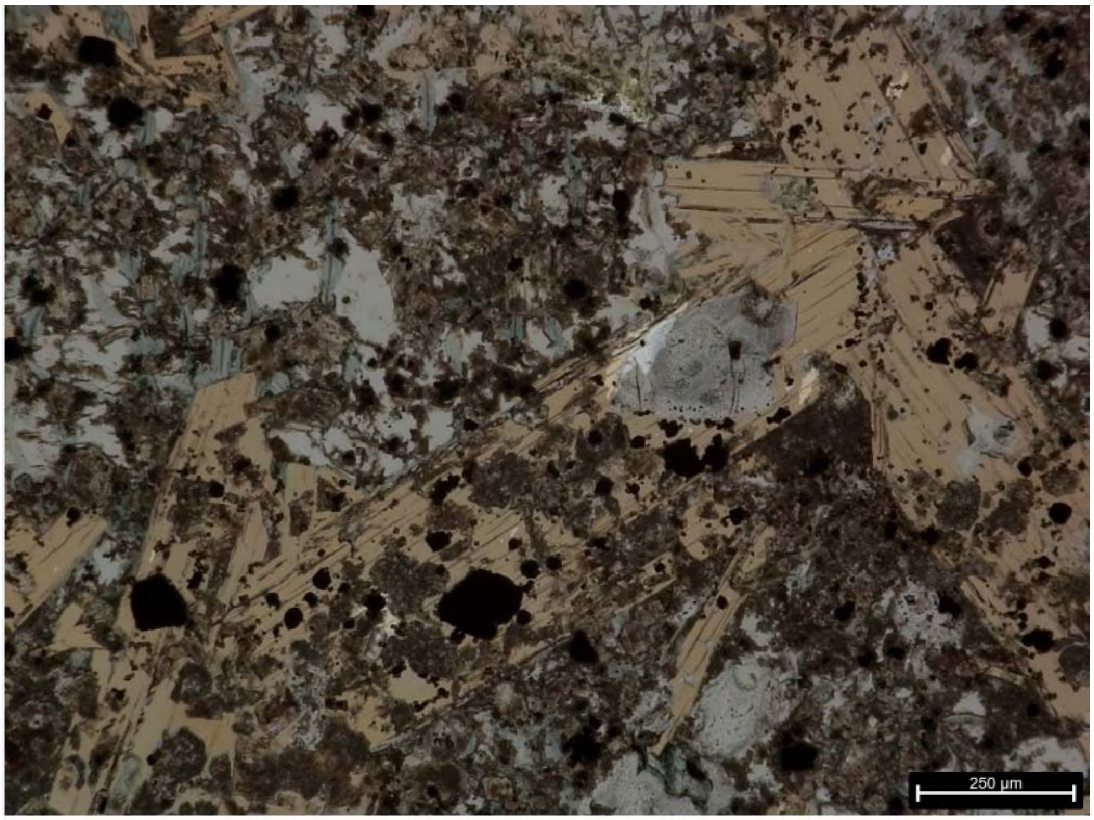

Figure A.3.: BHF-01-24-A.2 plane polarized light

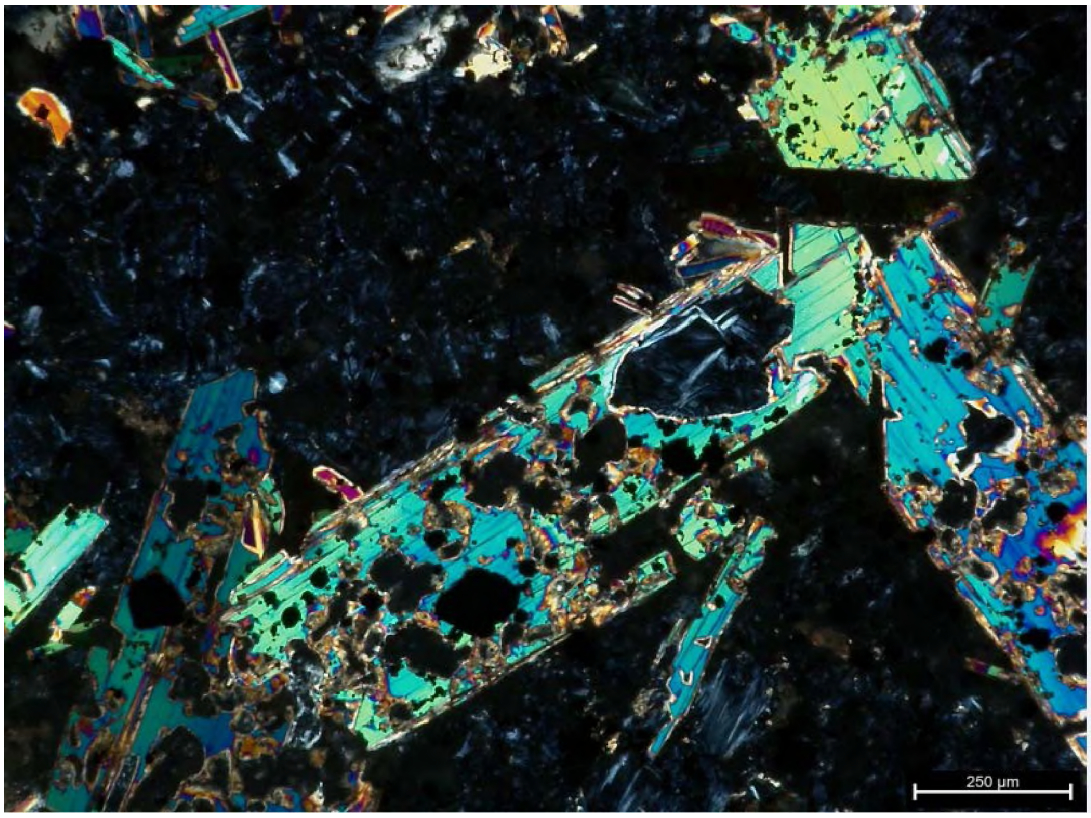

Figure A.4.: BHF-01-24-A.2 cross polarized light

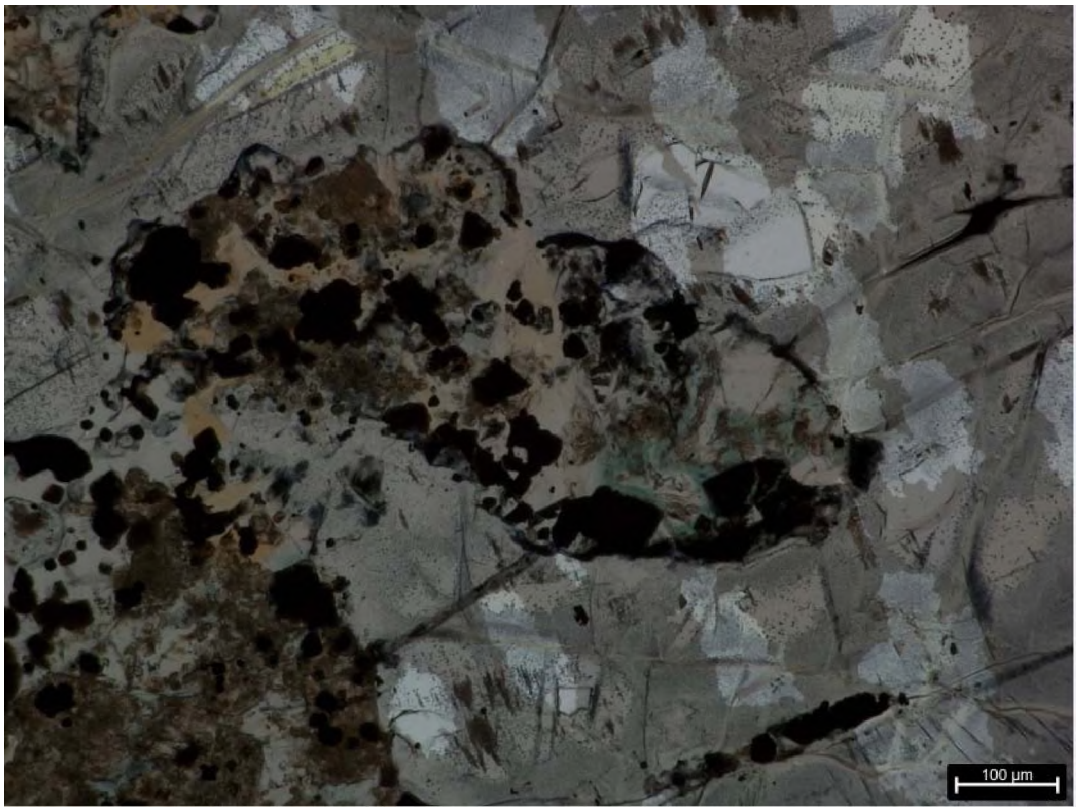

Figure A.5.: BHF-01-24-A.3 plane polarized light

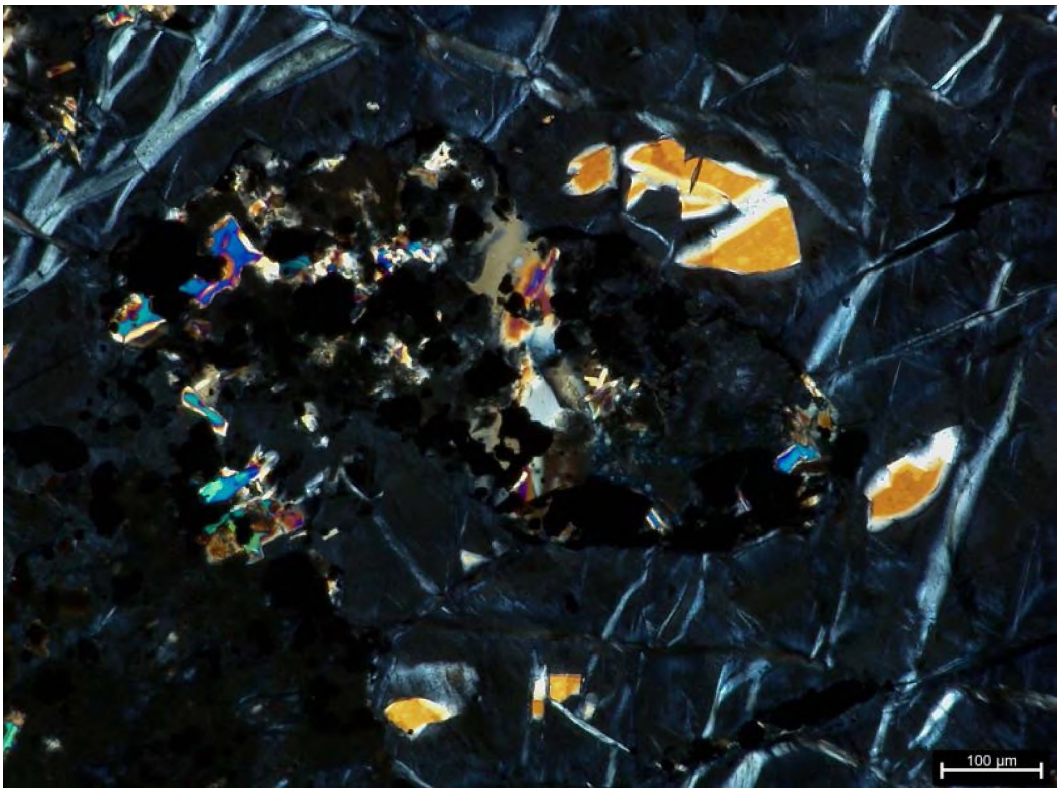

Figure A.6.: BHF-01-24-A.3 cross polarized light

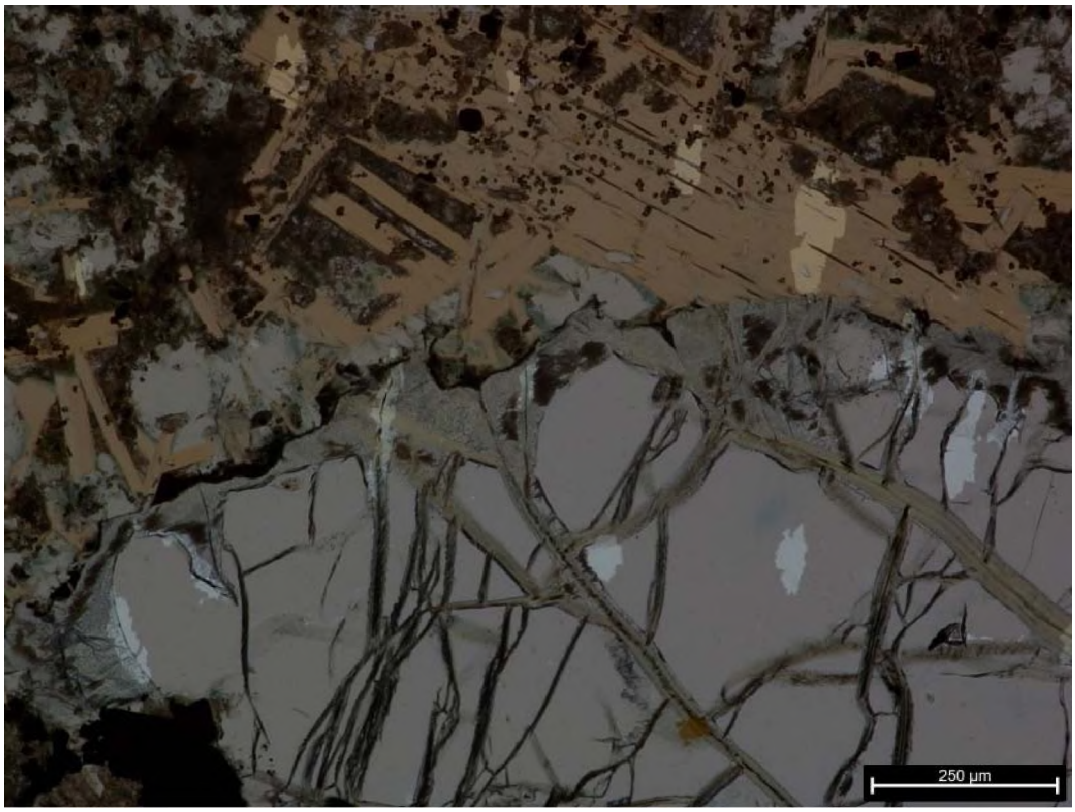

Figure A.7.: BHF-01-24-A.4 plane polarized light

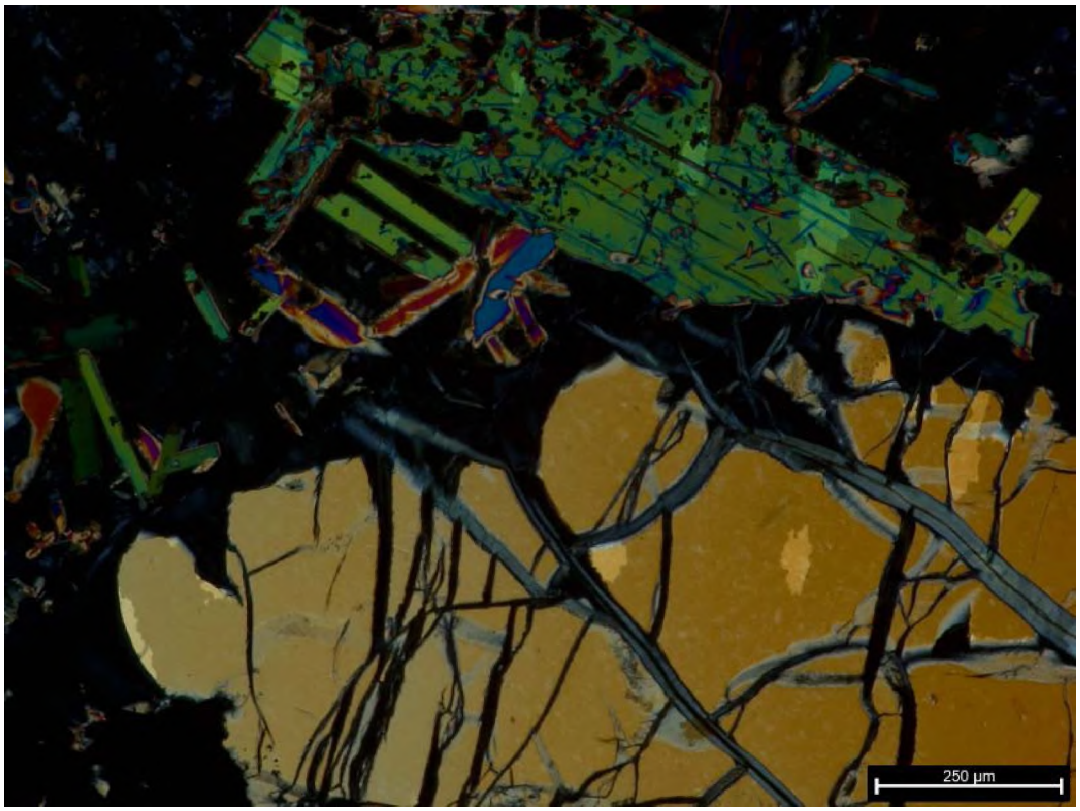

Figure A.8.: BHF-01-24-A.4 cross polarized light

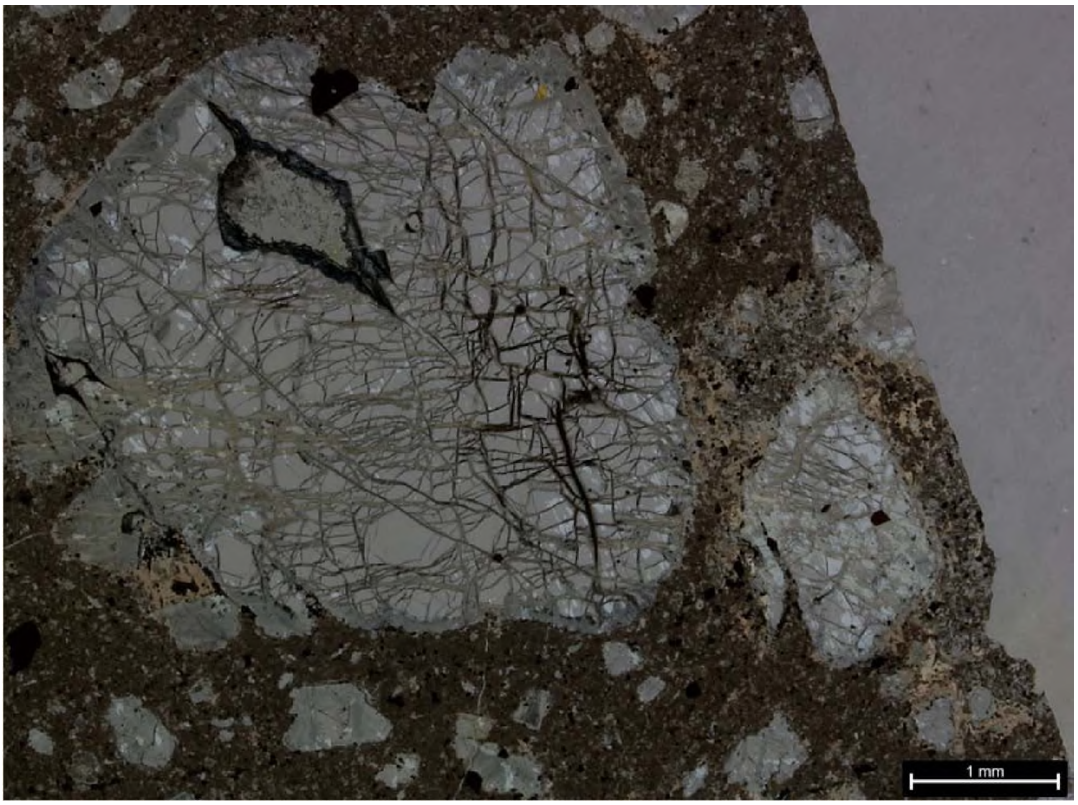

Figure A.9.: BHF-01-24-A.5 plane polarized light

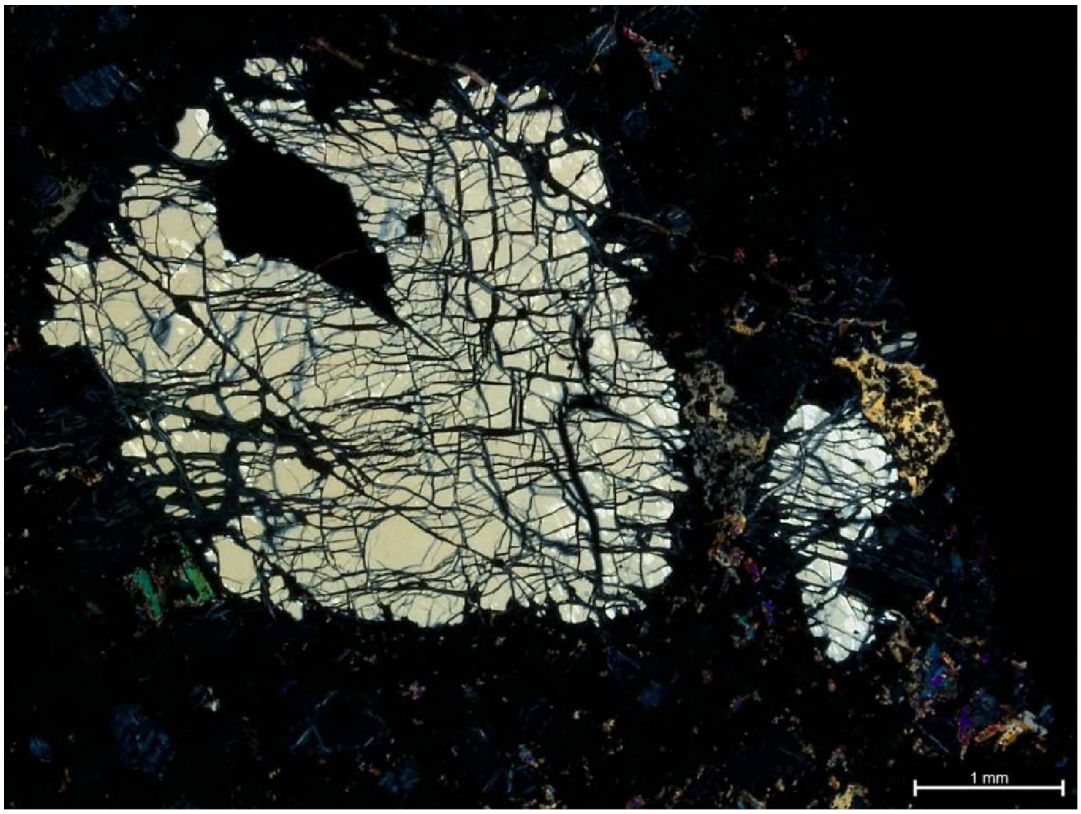

Figure A.10.: BHF-01-24-A.5 cross polarized light

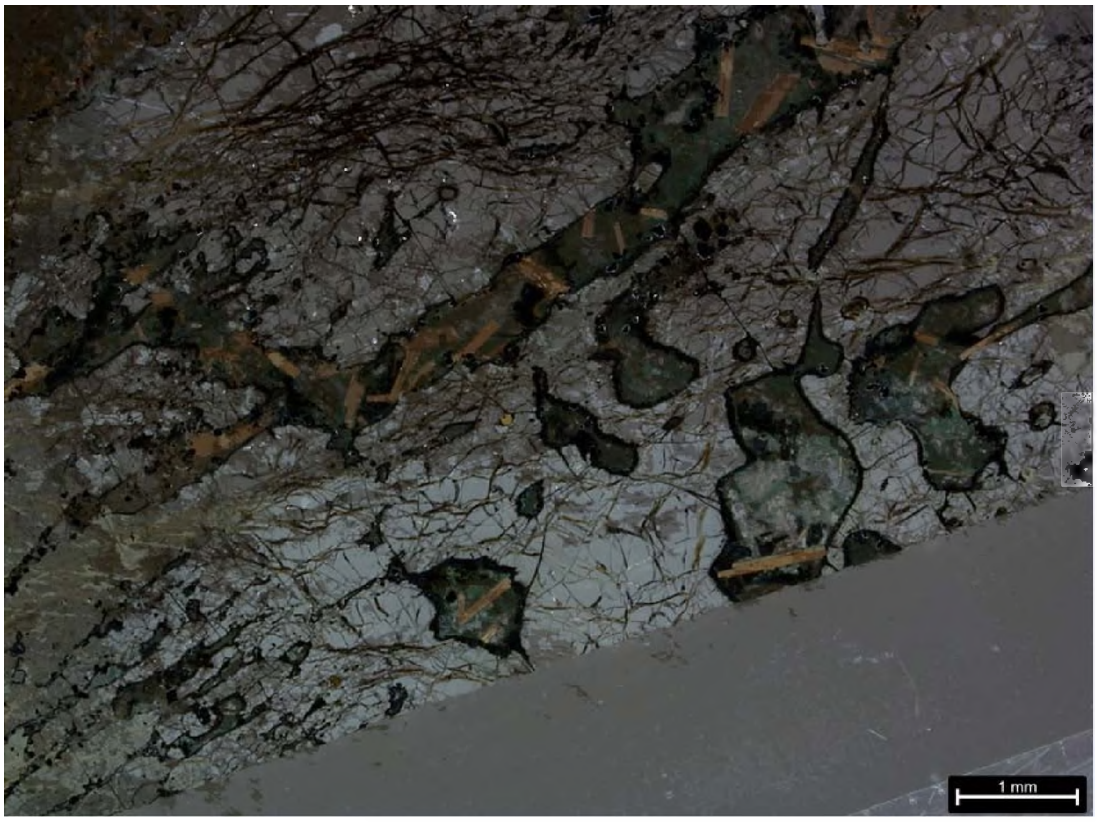

Figure A.11.: BHF-01-24-B.1 plane polarized light

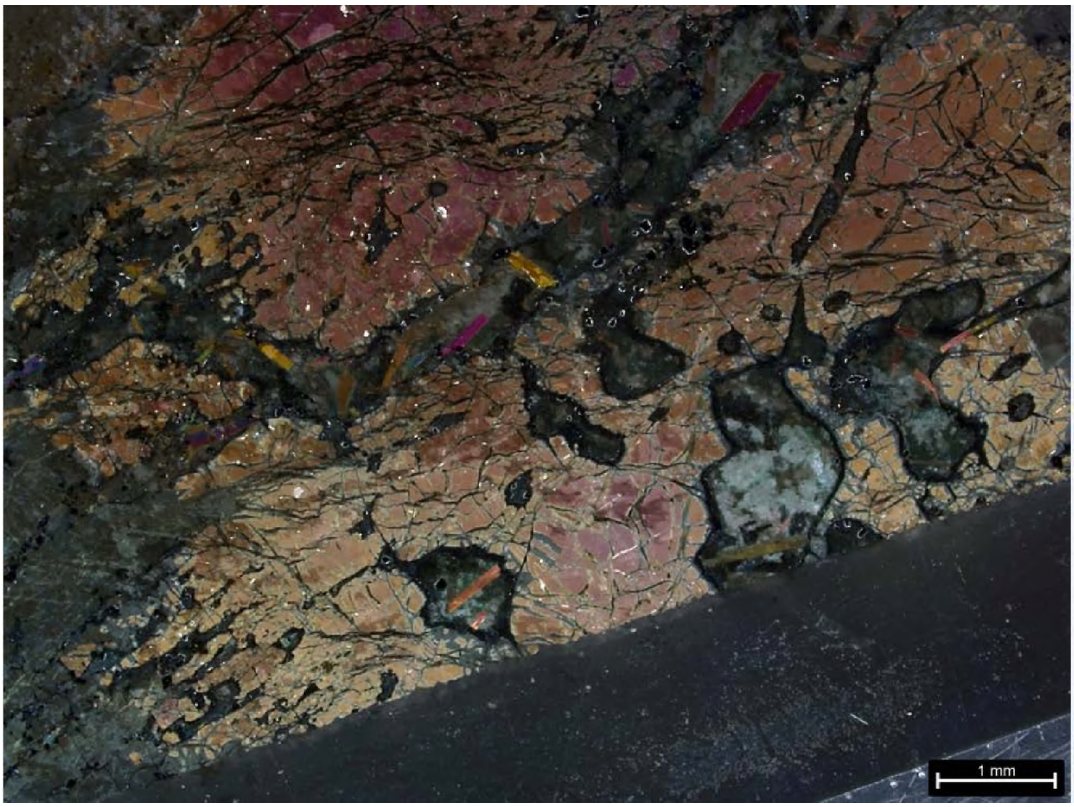

Figure A.12.: BHF-01-24-B.1 cross polarized light

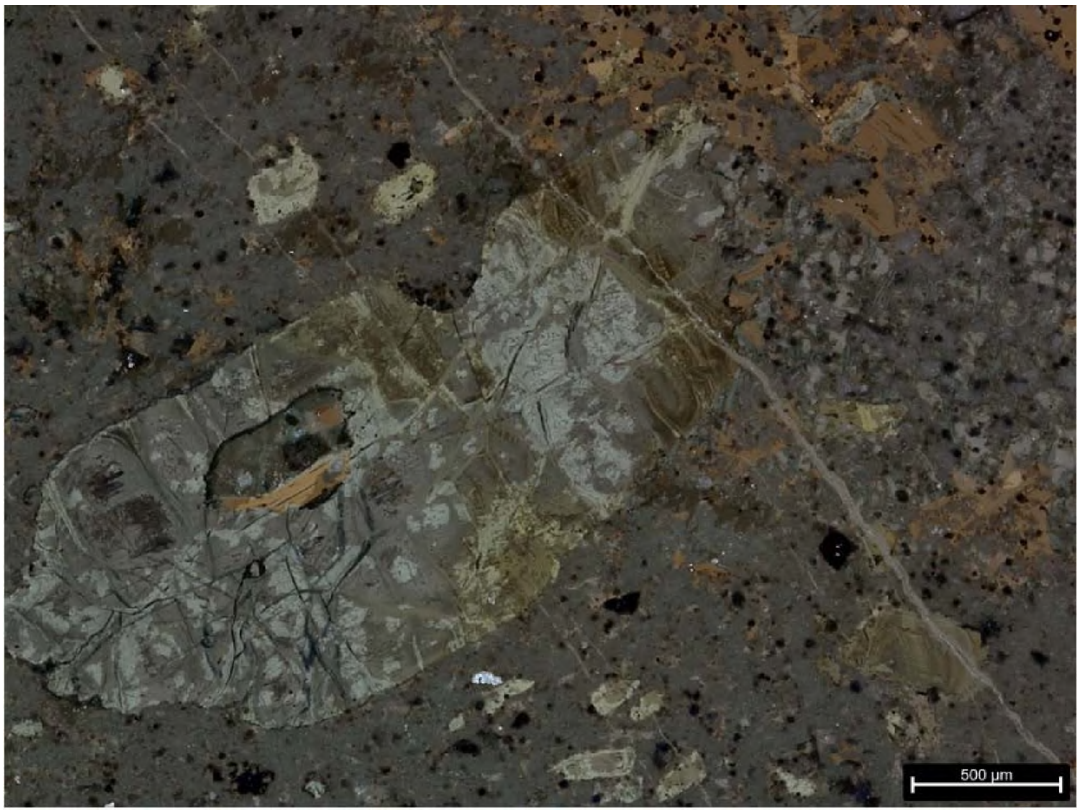

Figure A.13.: BHF-01-24-B.2 plane polarized light

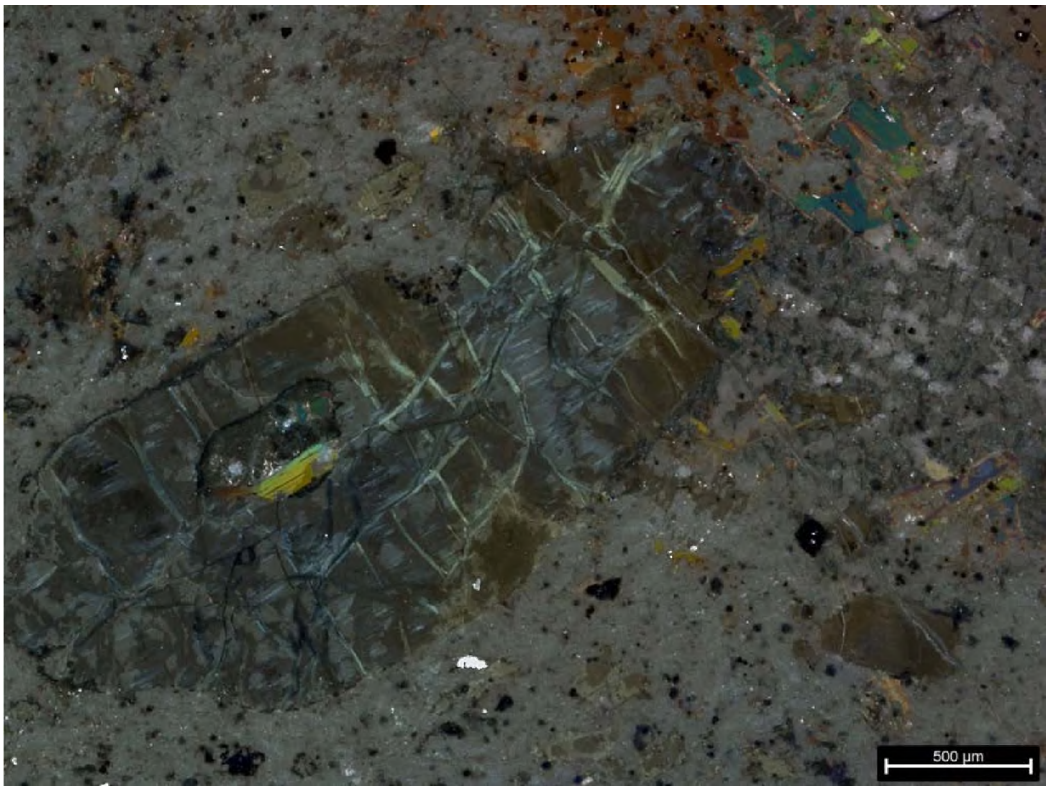

Figure A.14.: BHF-01-24-B.2 cross polarized light

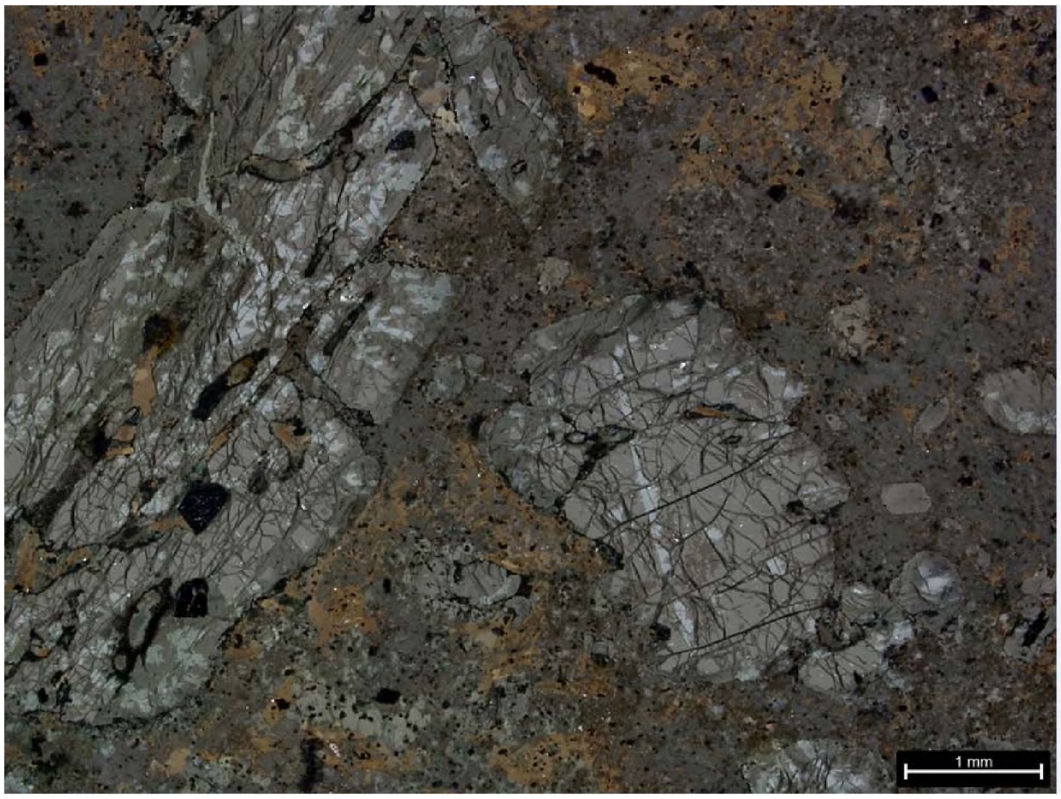

Figure A.15.: BHF-01-24-B.3 plane polarized light

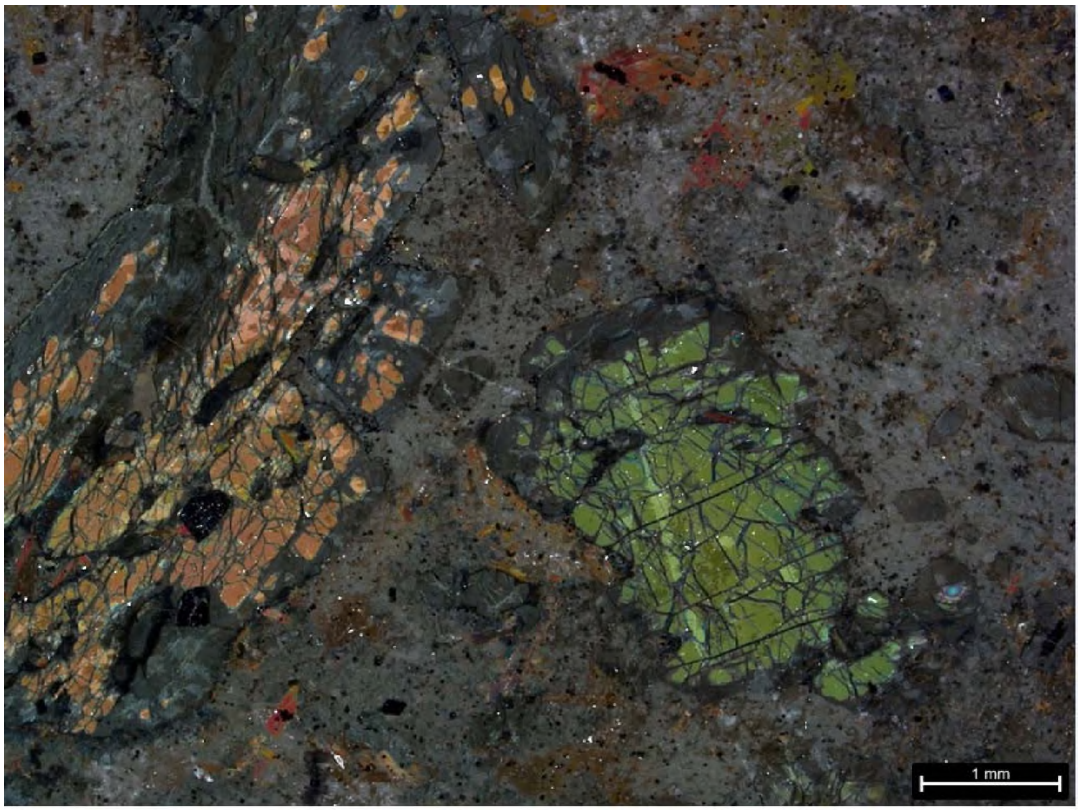

Figure A.16.: BHF-01-24-B.3 cross polarized light

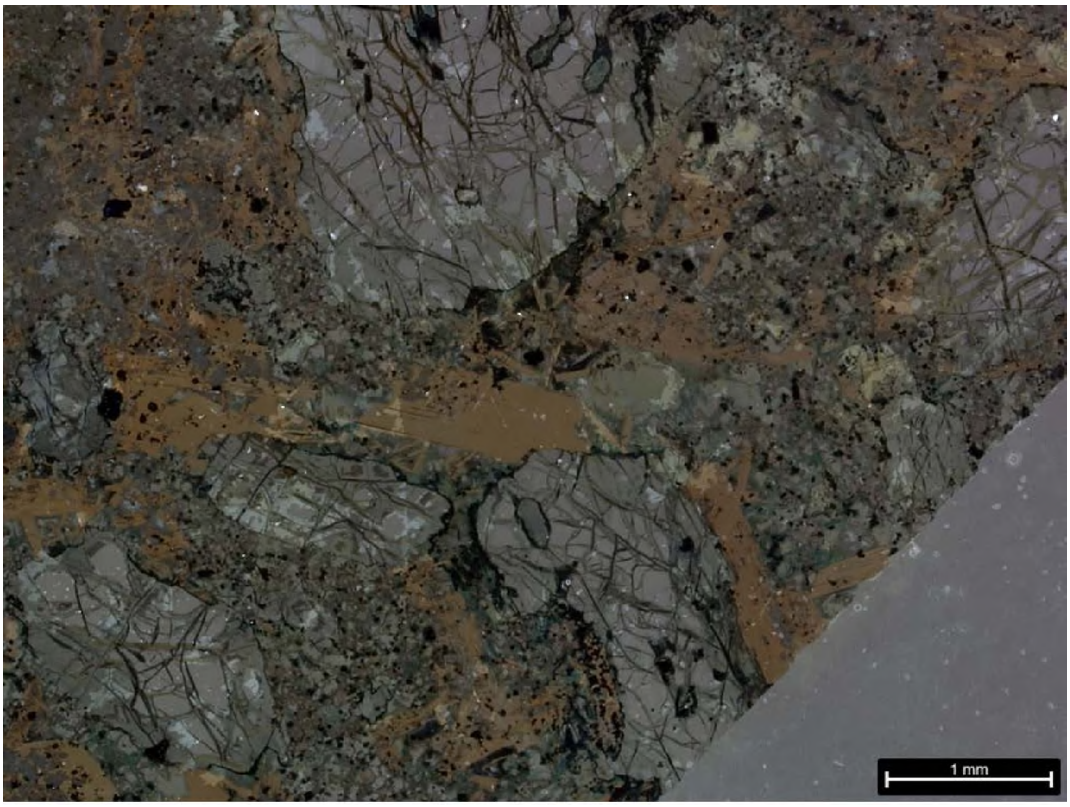

Figure A.17.: BHF-01-24-B.4 plane polarized light

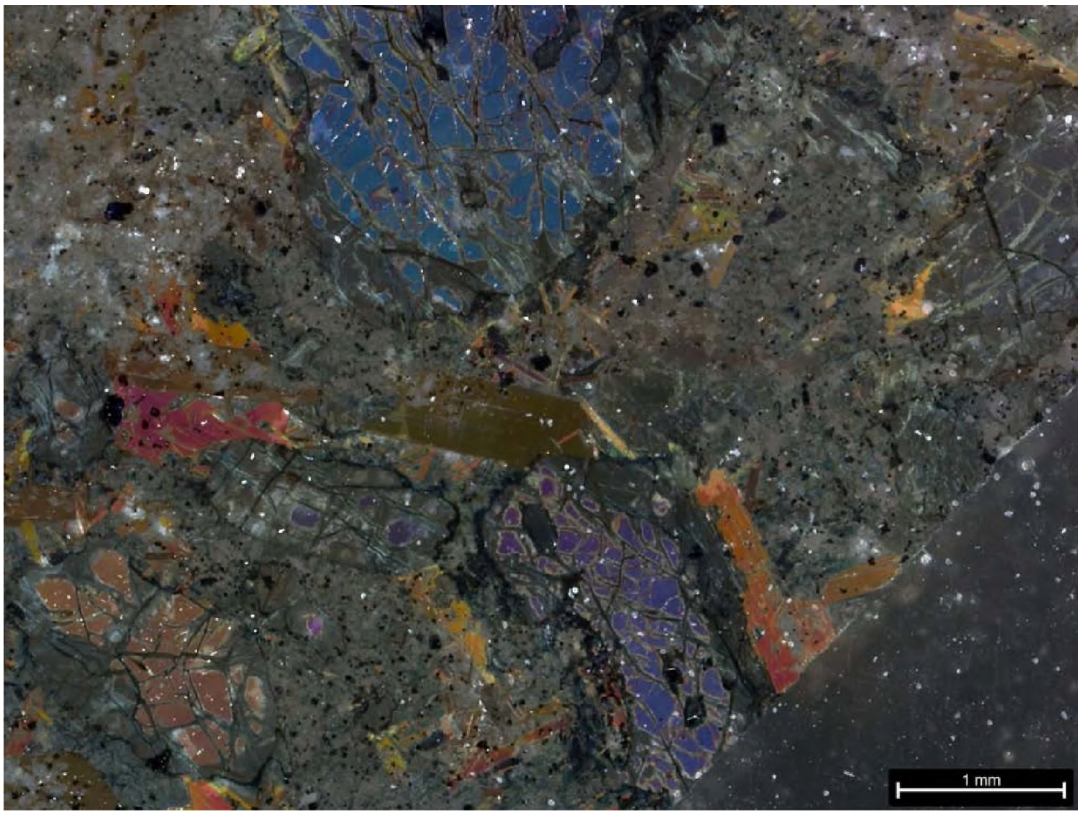

Figure A.18.: BHF-01-24-B.4 cross polarized light

Figure A.19.: BHF-01-24-C.1 plane polarized light

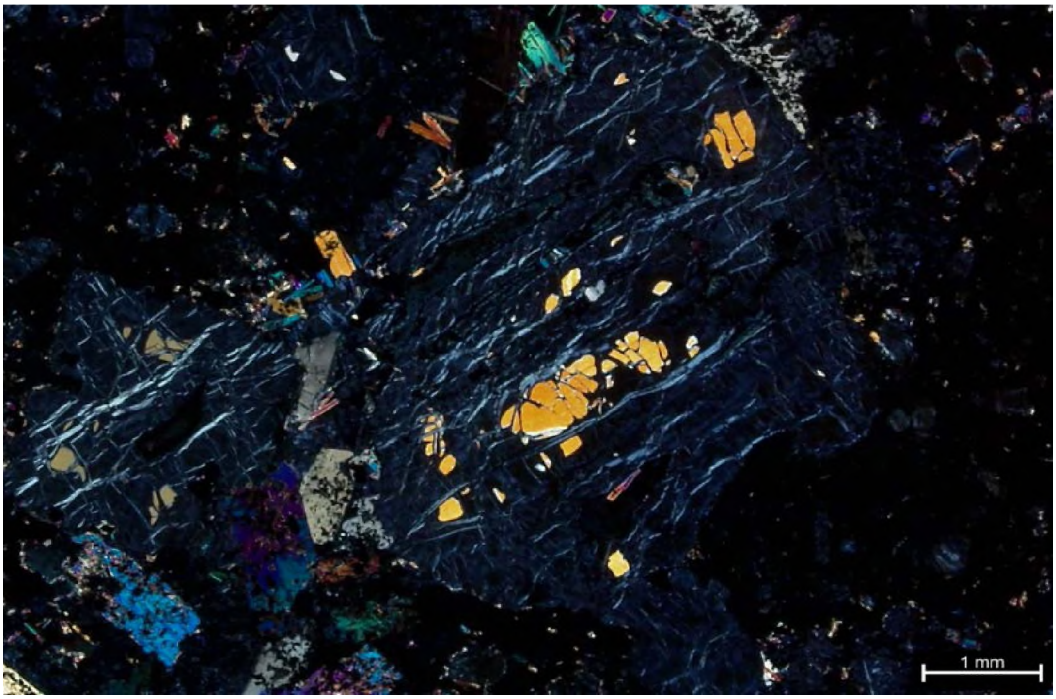

Figure A.20.: BHF-01-24-C.1 cross polarized light

Figure A.21.: BHF-01-24-C.2 plane polarized light

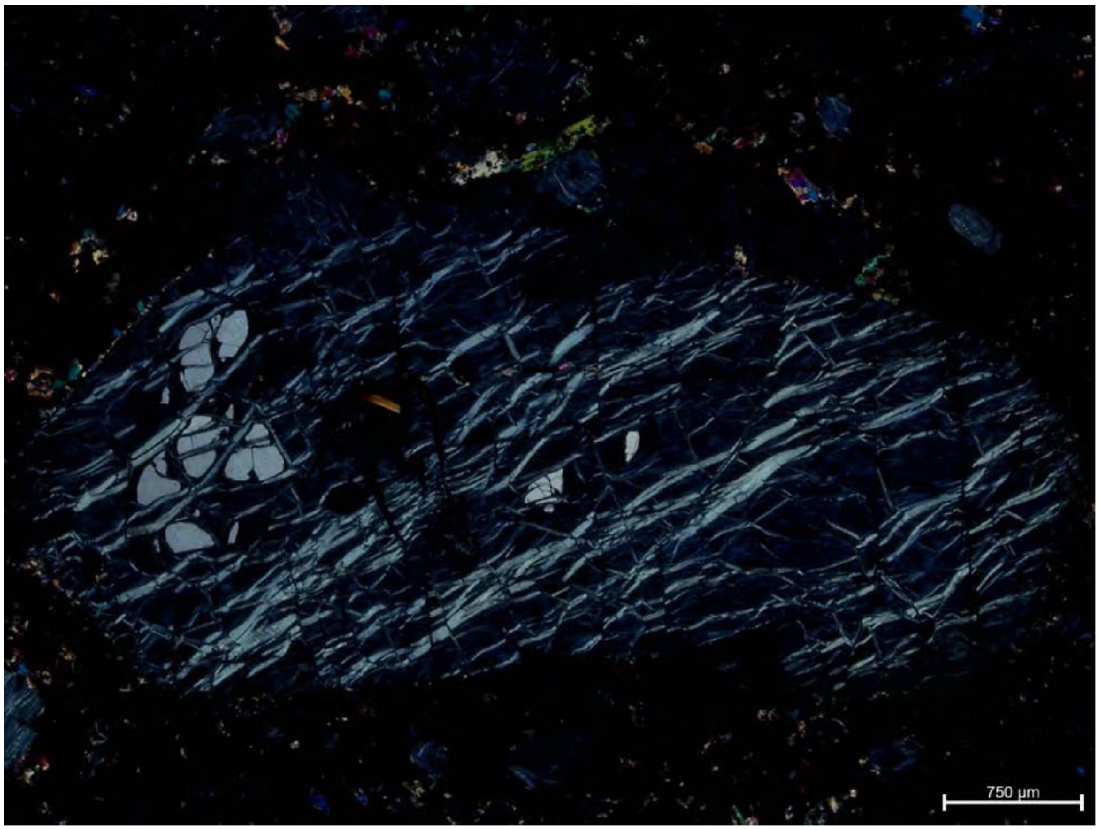

Figure A.22.: BHF-01-24-C.2 cross polarized light

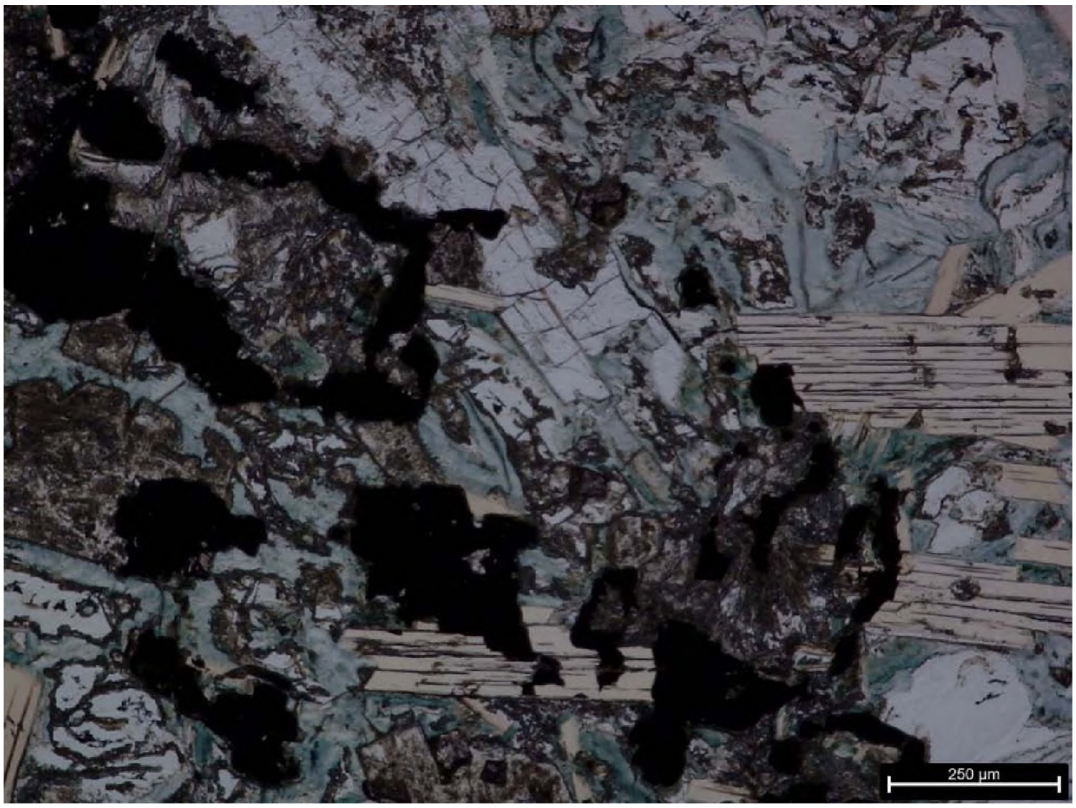

Figure A.23.: BHF-01-24-C.3 plane polarized light

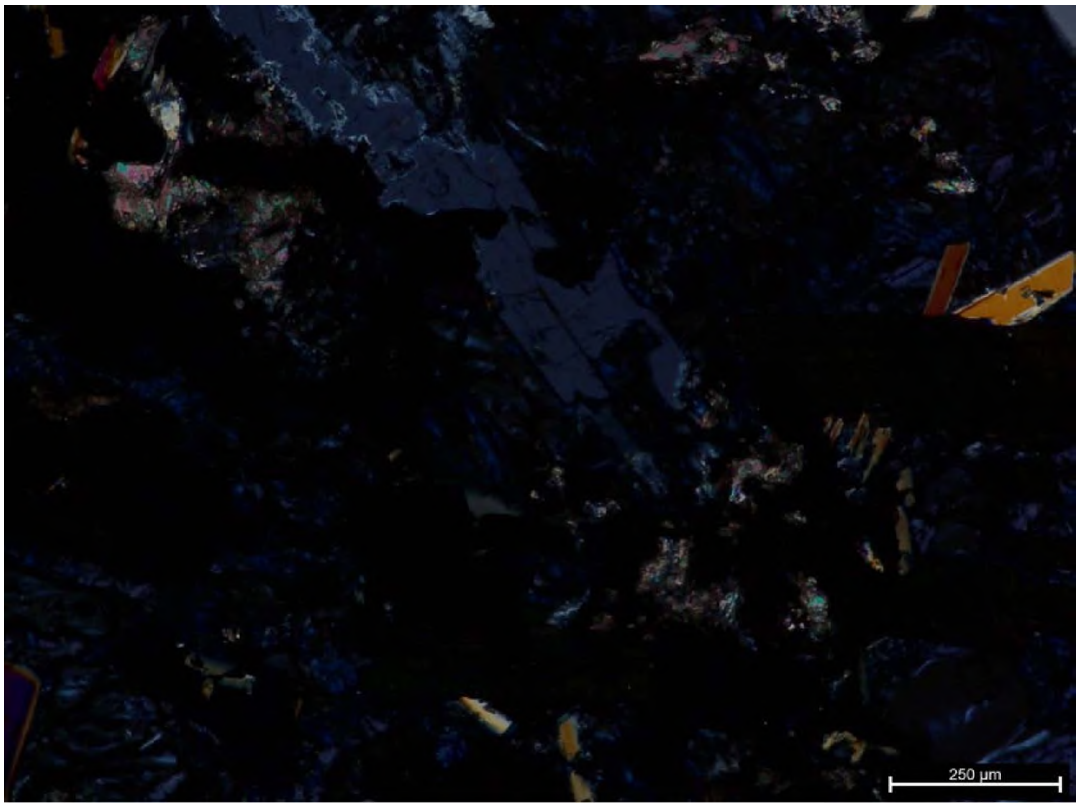

Figure A.24.: BHF-01-24-C.3 cross polarized light

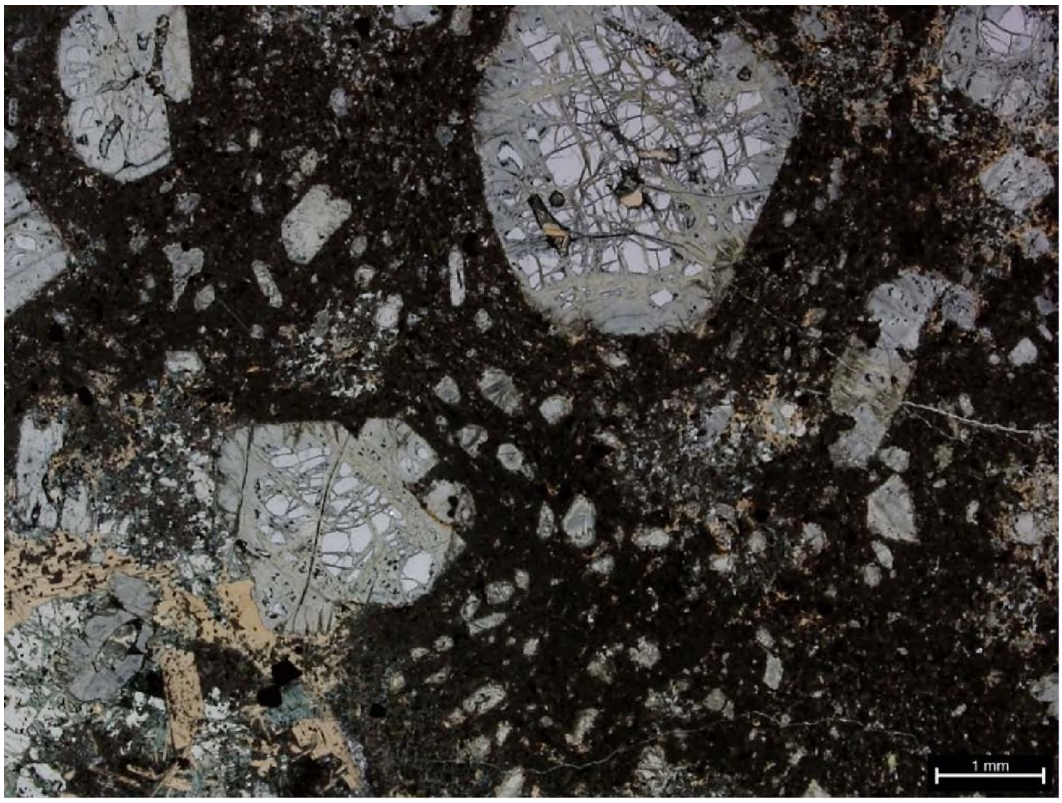

Figure A.25.: BHF-01-24-D.1 plane polarized light

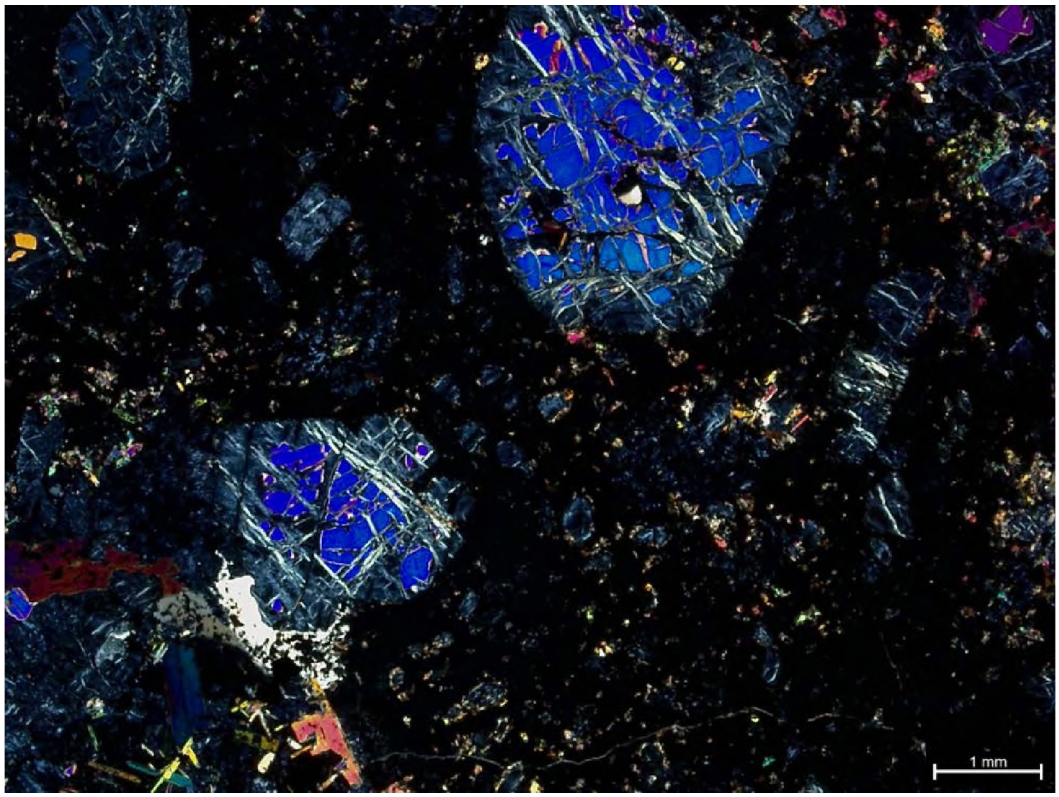

Figure A.26.: BHF-01-24-D.1 cross polarized light

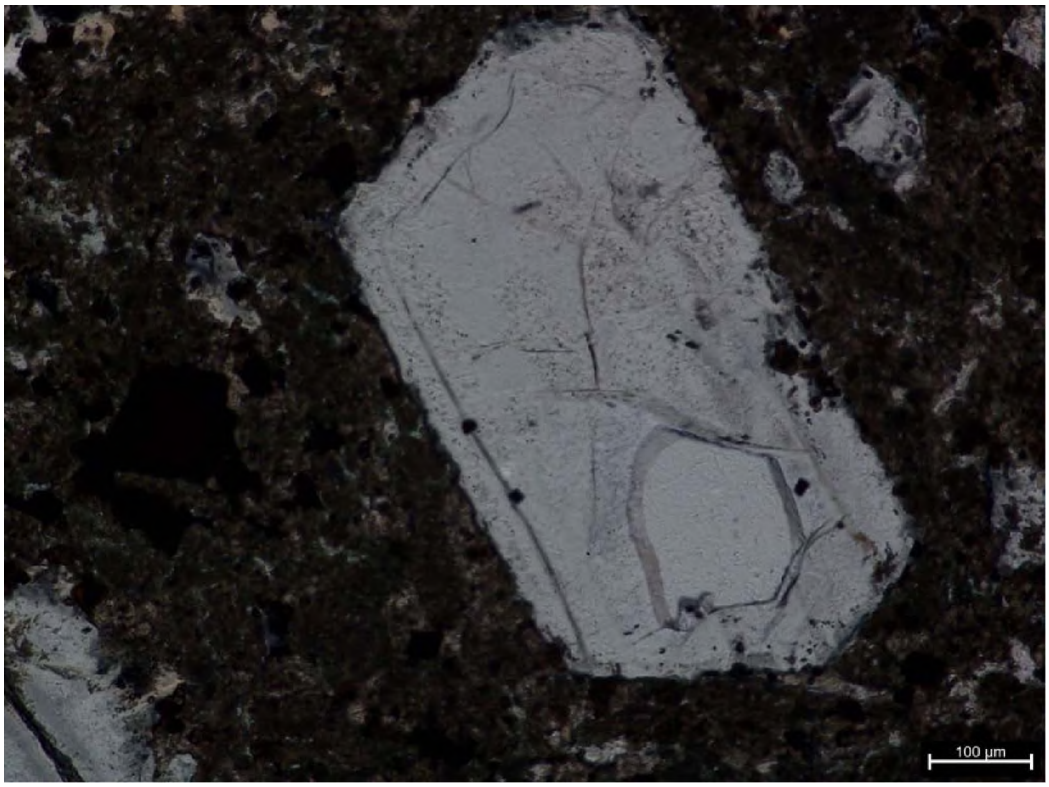

Figure A.27.: BHF-01-24-D.2 plane polarized light

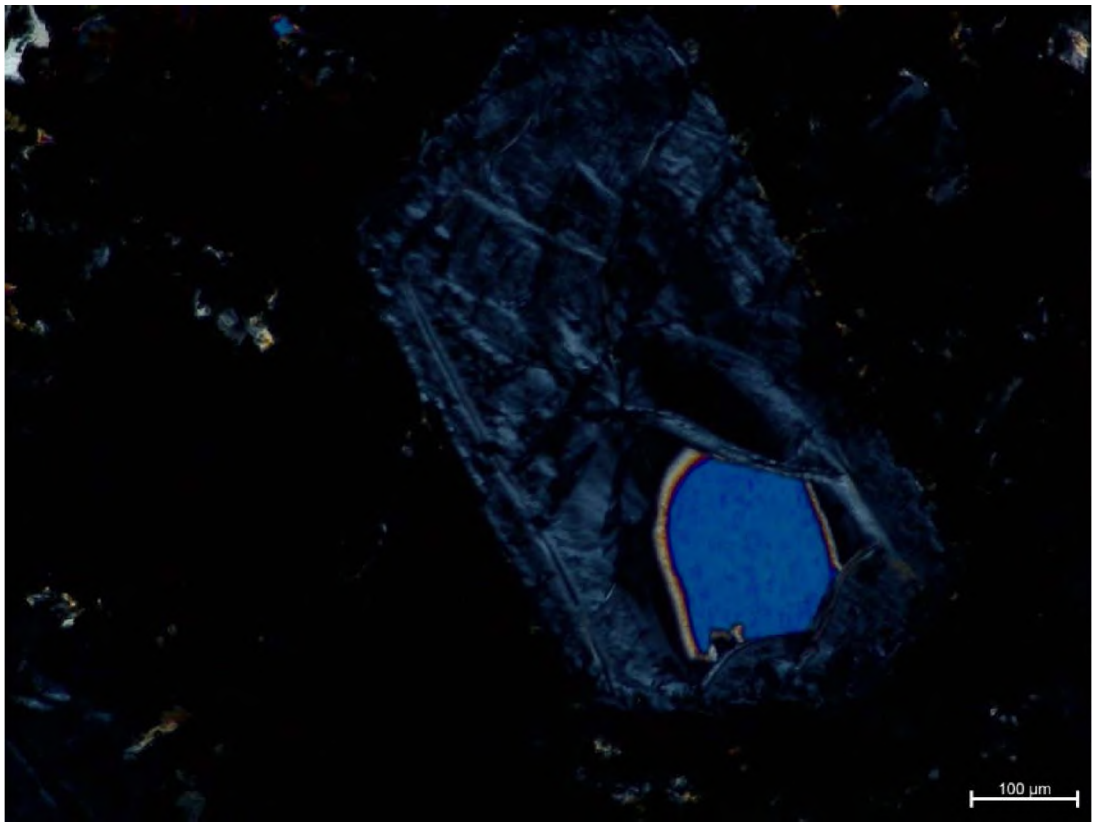

Figure A.28.: BHF-01-24-D.2 cross polarized light

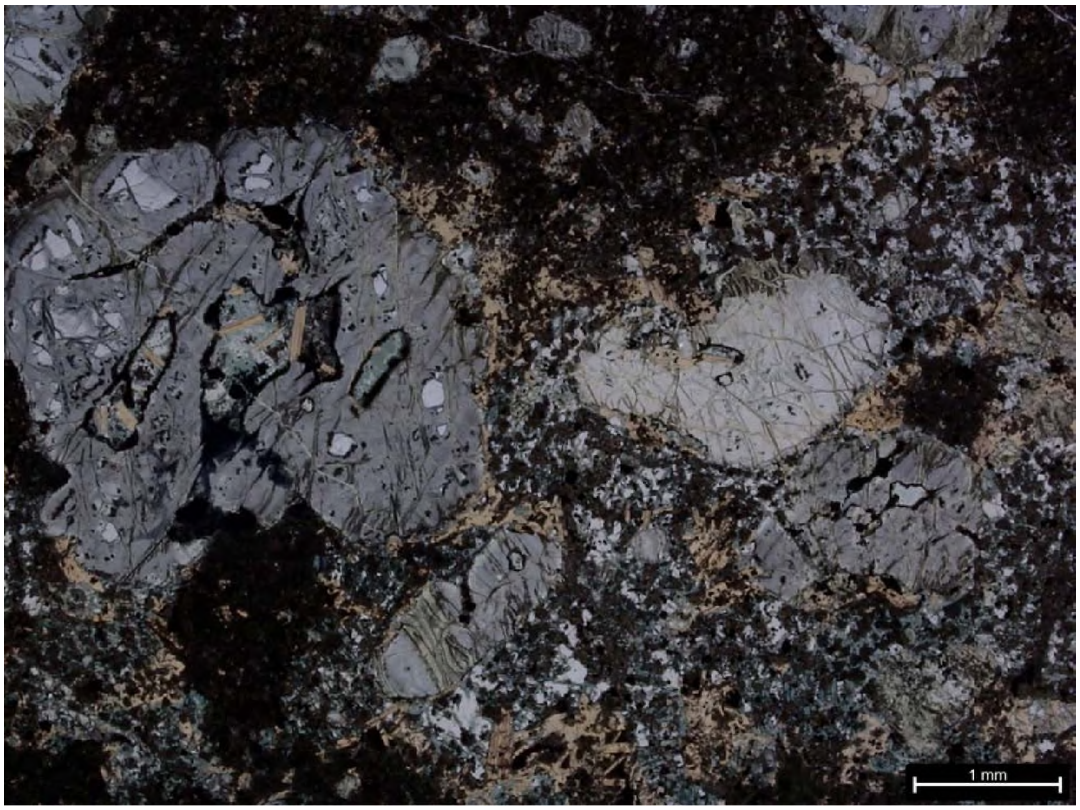

Figure A.29.: BHF-01-24-D.3 plane polarized light

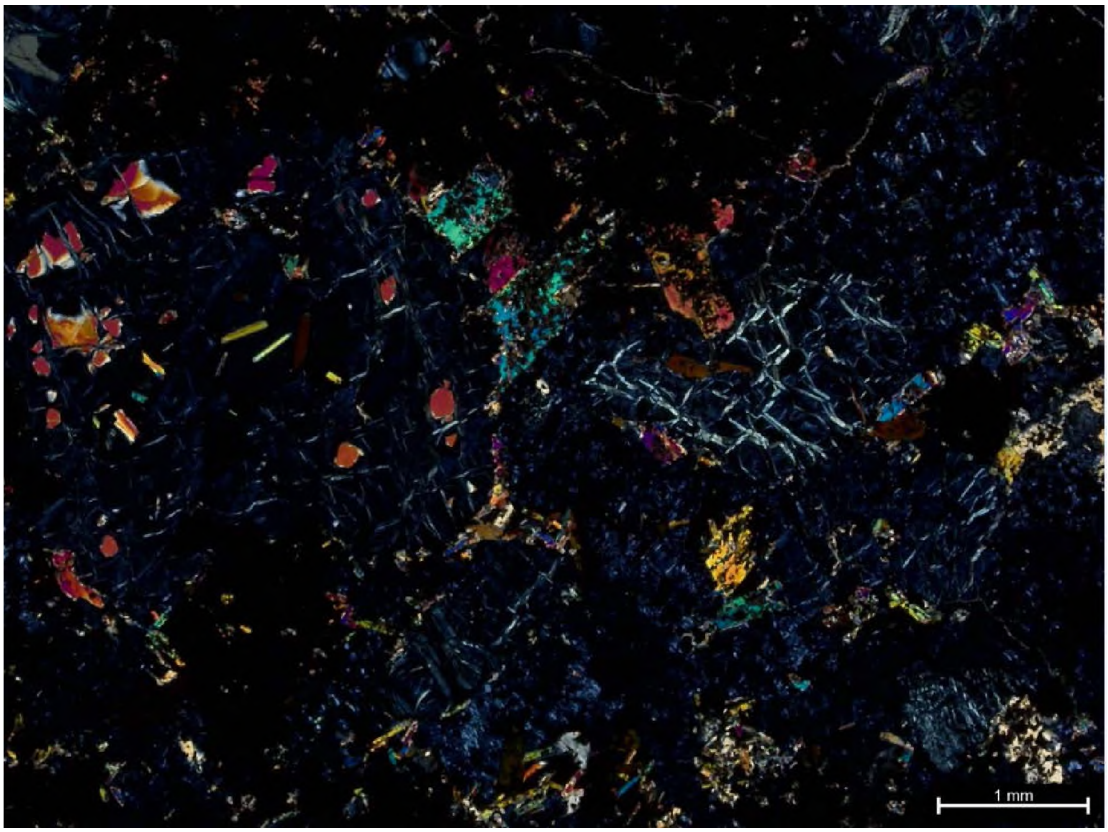

Figure A.30.: BHF-01-24-D.3 cross polarized light

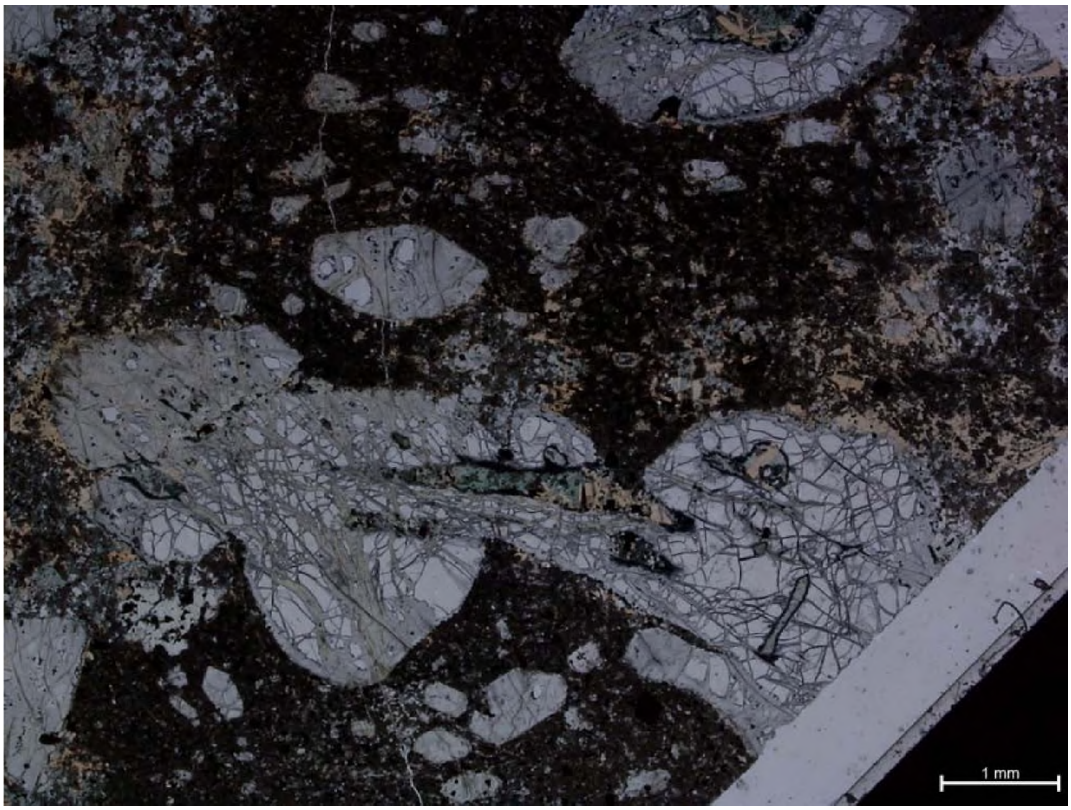

Figure A.31.: BHF-01-24-D.4 plane polarized light

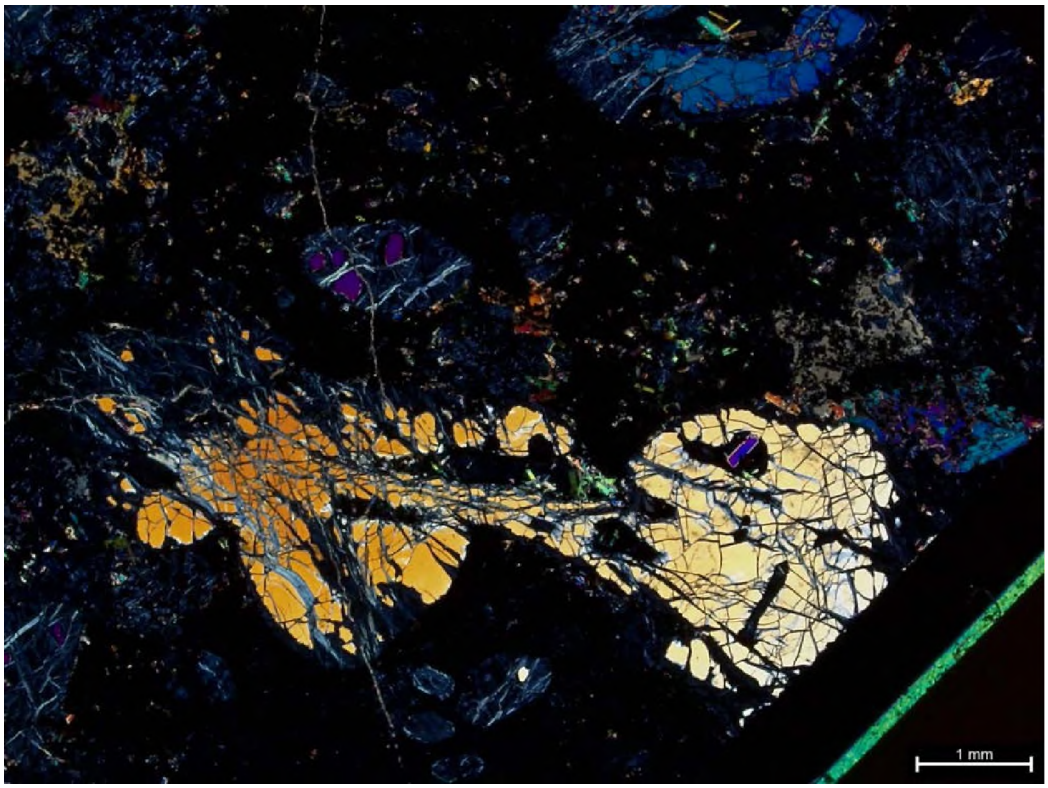

Figure A.32.: BHF-01-24-D.4 cross polarized light

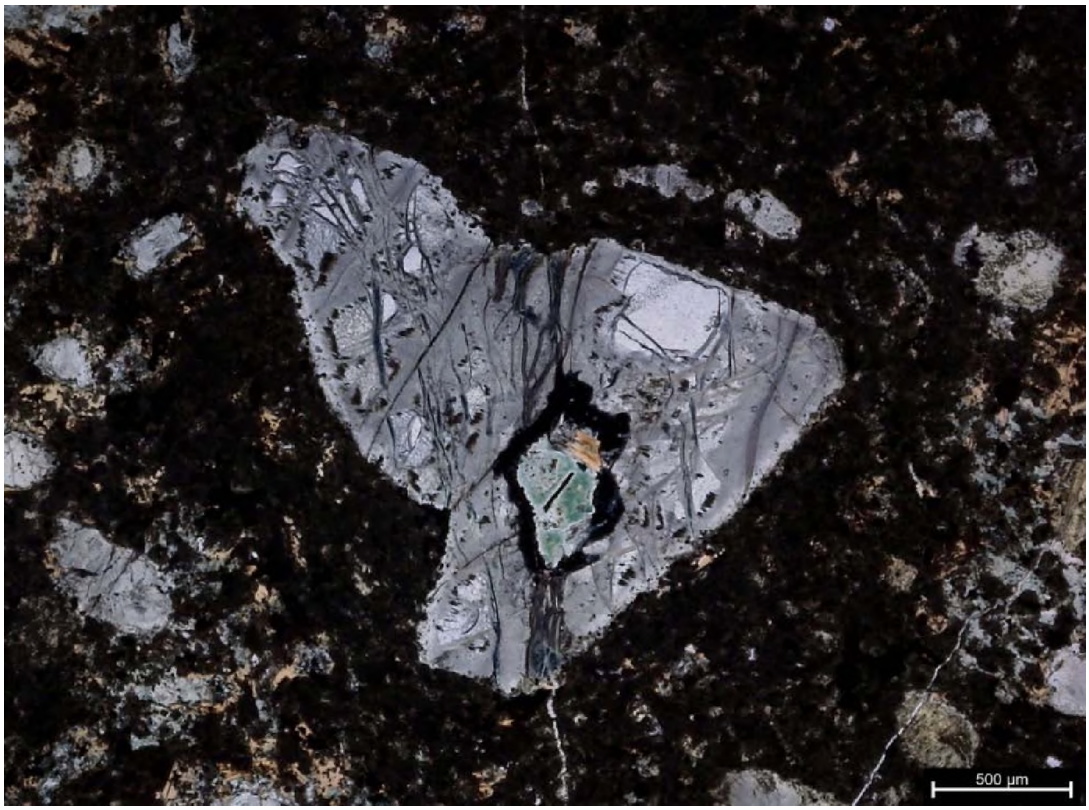

Figure A.33.: BHF-01-24-D.5 plane polarized light

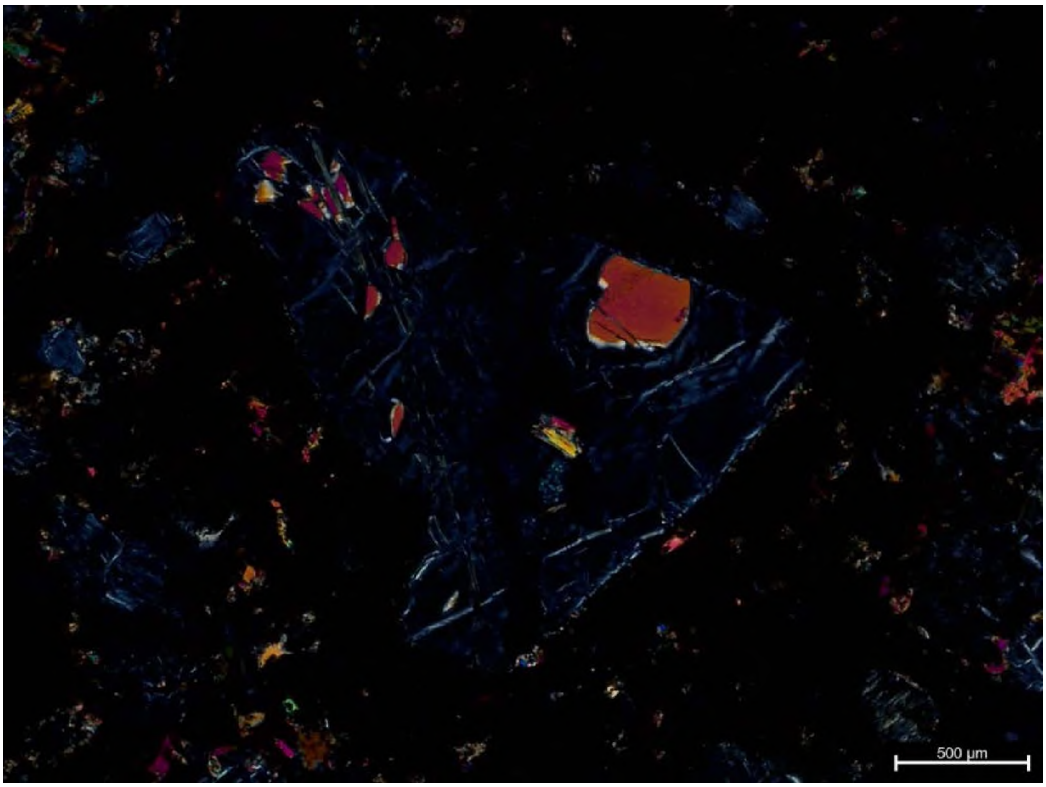

Figure A.34.: BHF-01-24-D.5 cross polarized light

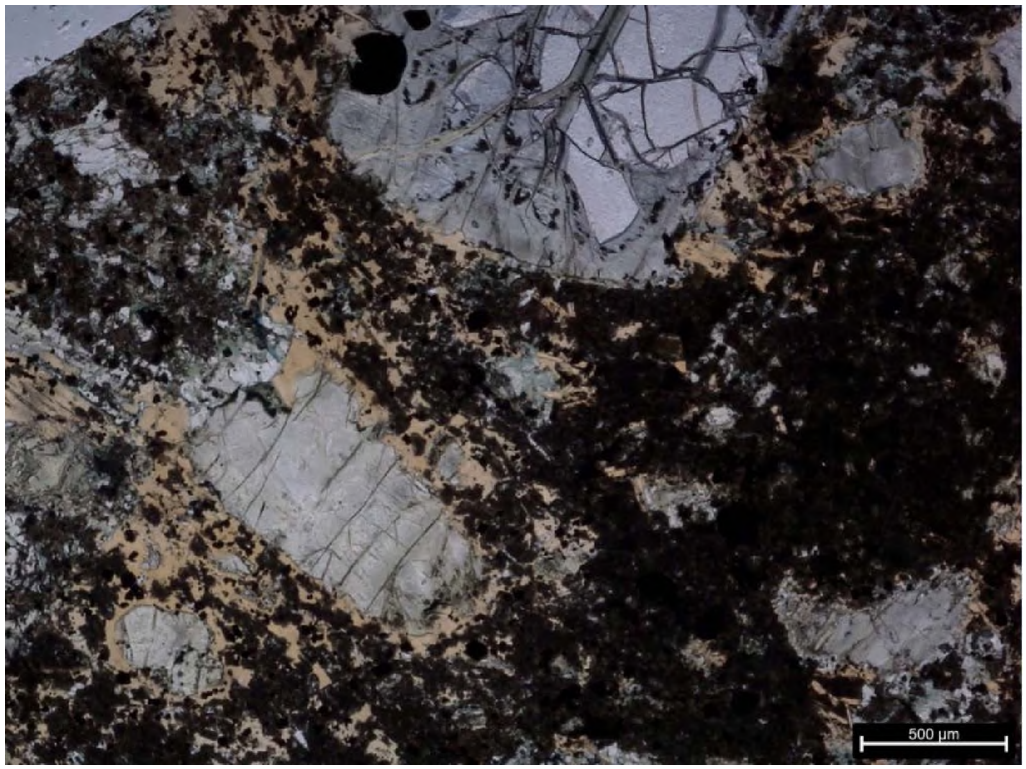

Figure A.35.: BHF-01-24-D.6 plane polarized light

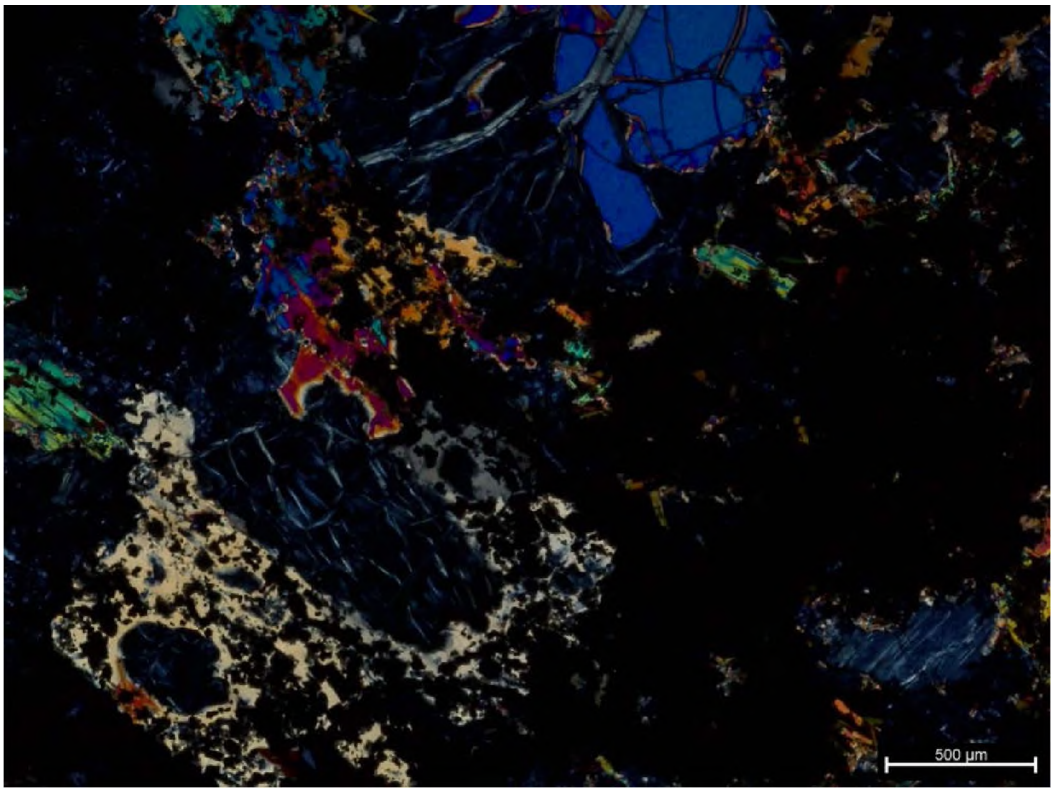

Figure A.36.: BHF-01-24-D.6 cross polarized light

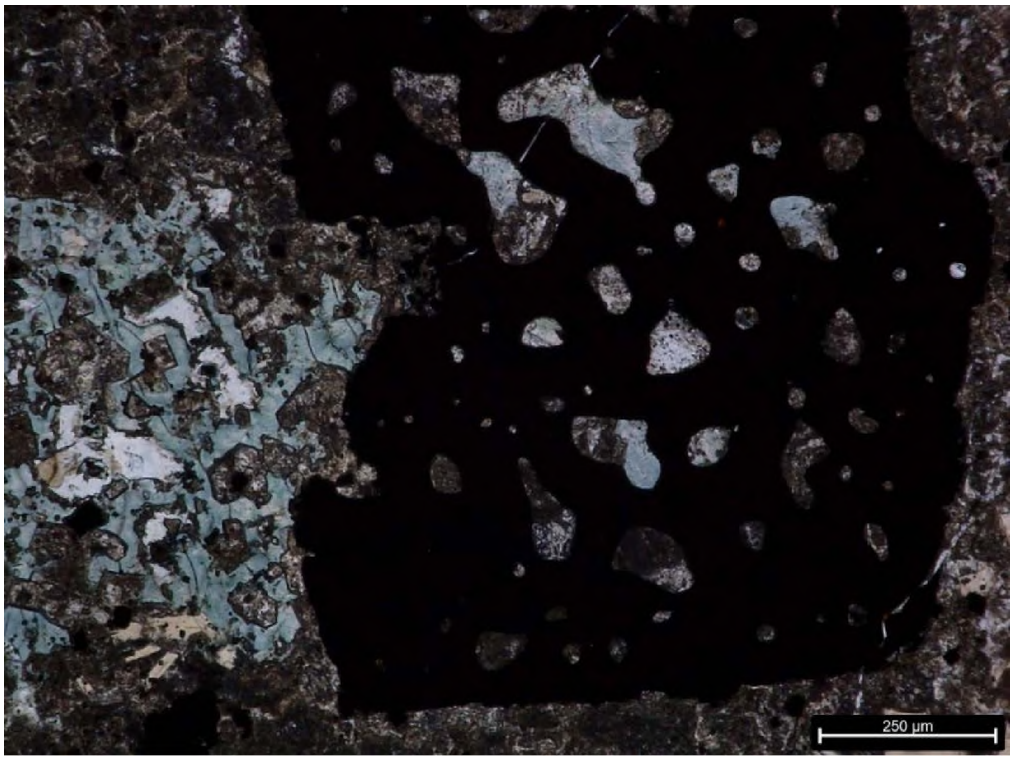

Figure A.37.: BHF-01-24-D.7 plane polarized light

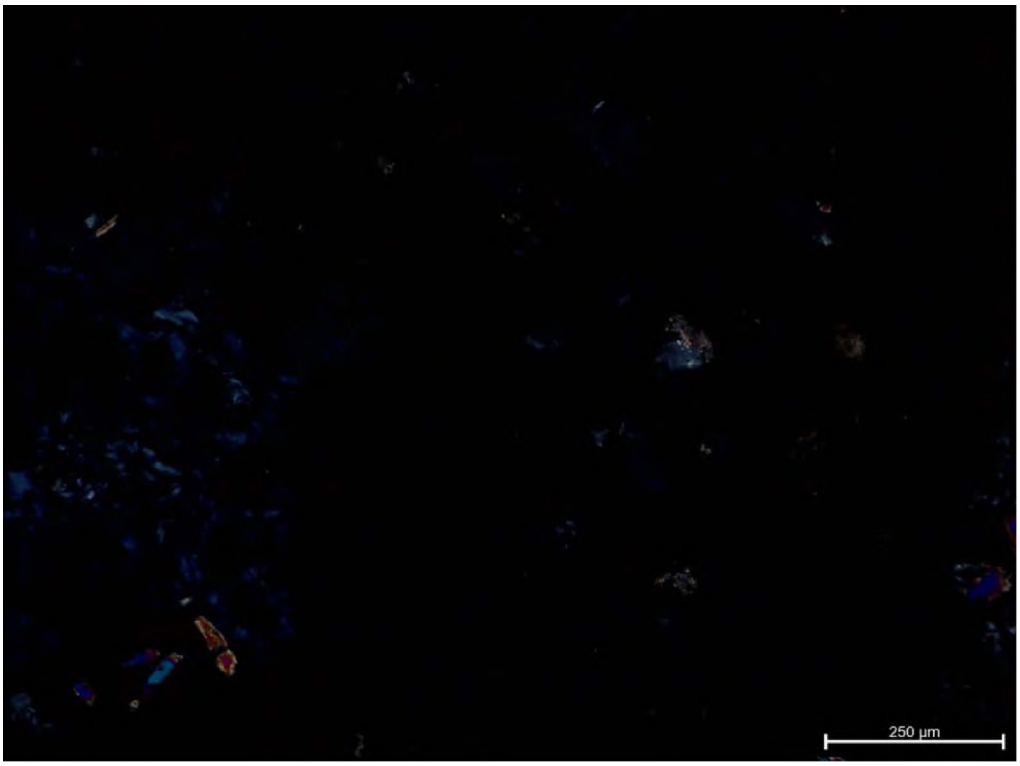

Figure A.38.: BHF-01-24-D.7 cross polarized light

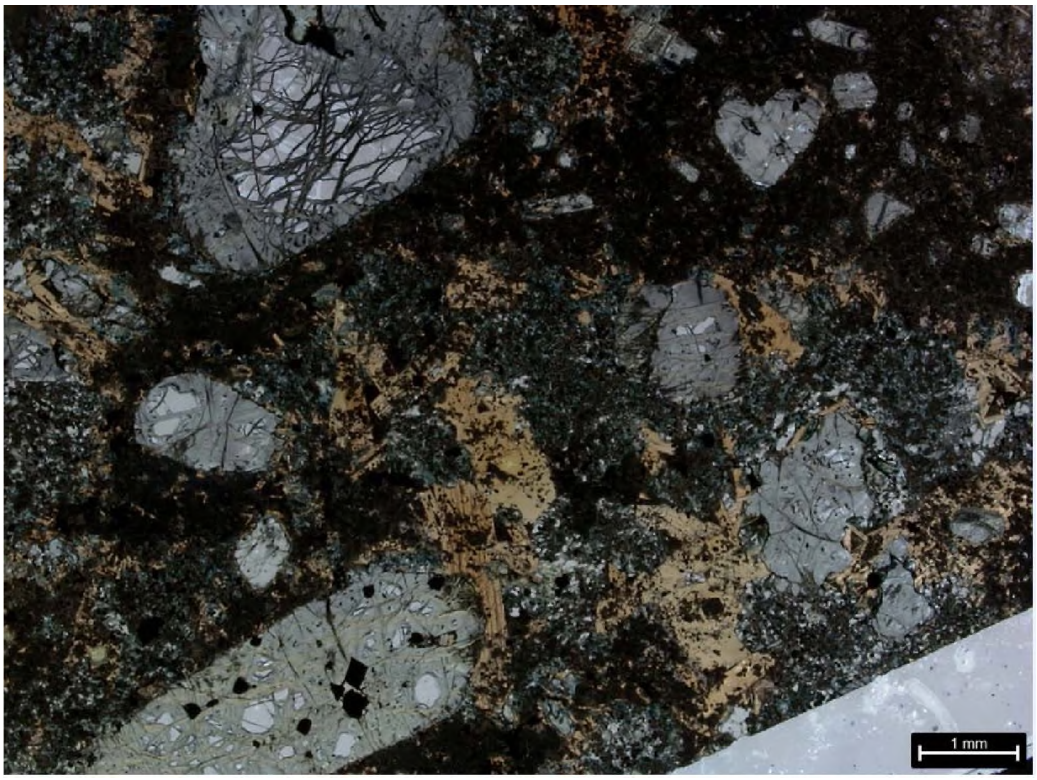

Figure A.39.: BHF-01-24-E.1 plane polarized light

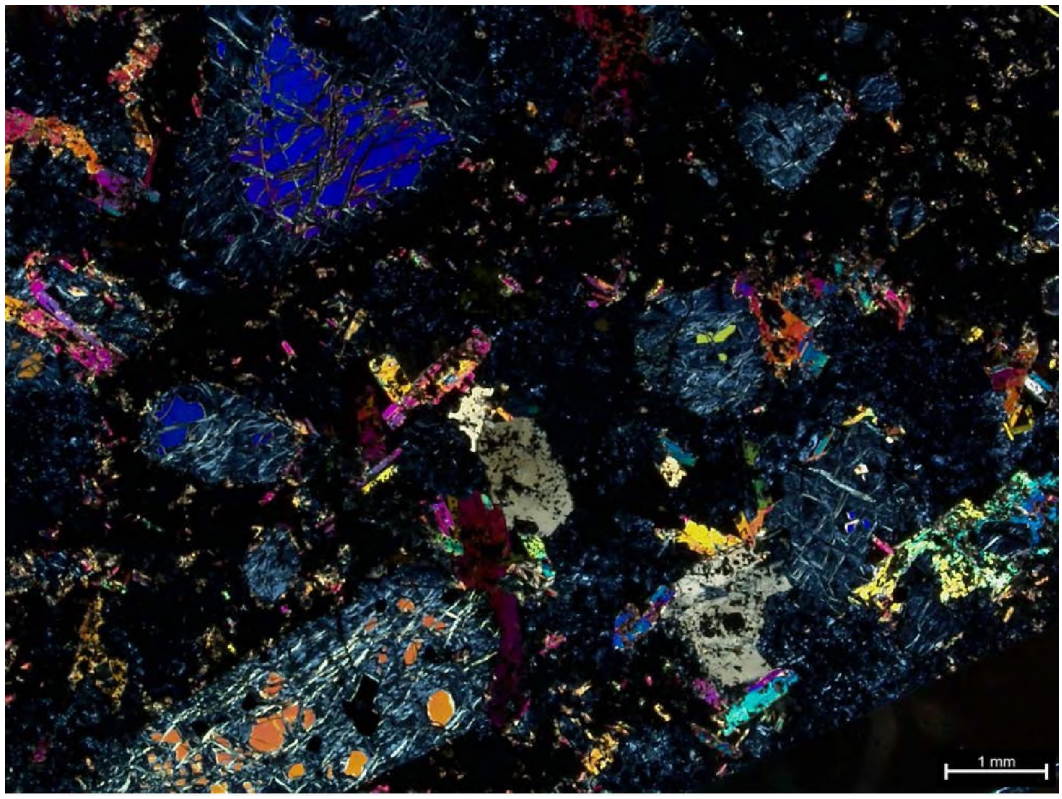

Figure A.40.: BHF-01-24-E.1 cross polarized light

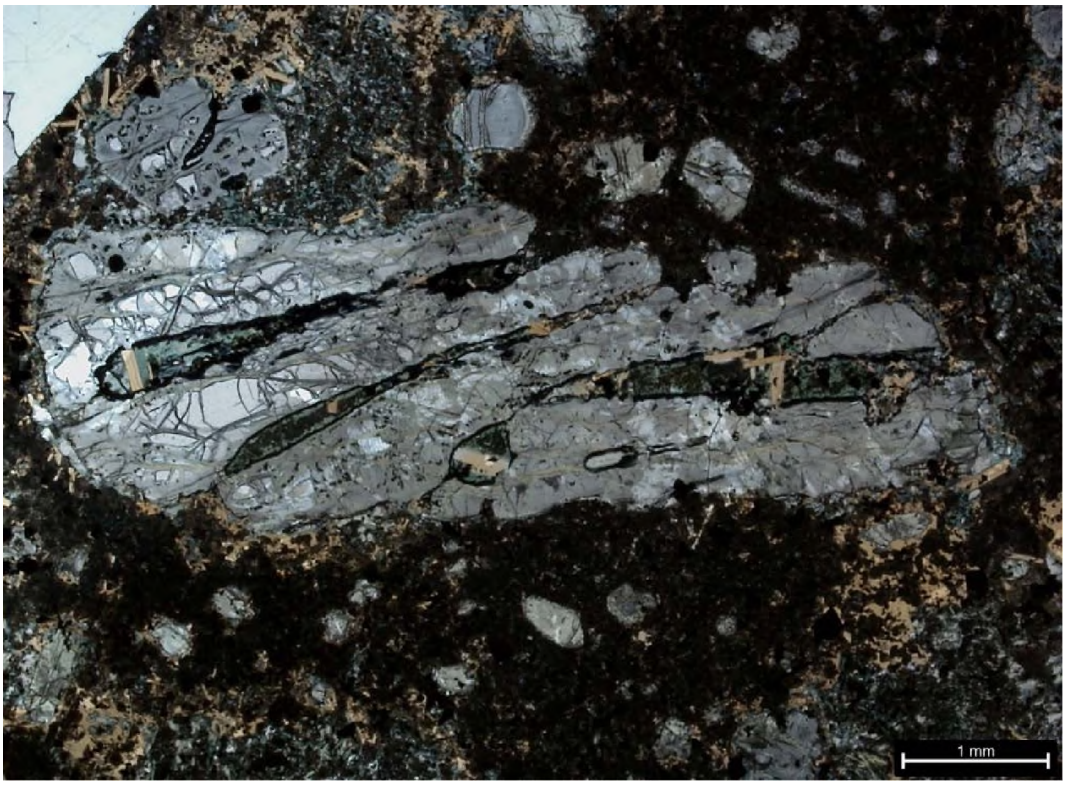

Figure A.41.: BHF-01-24-E.2 plane polarized light

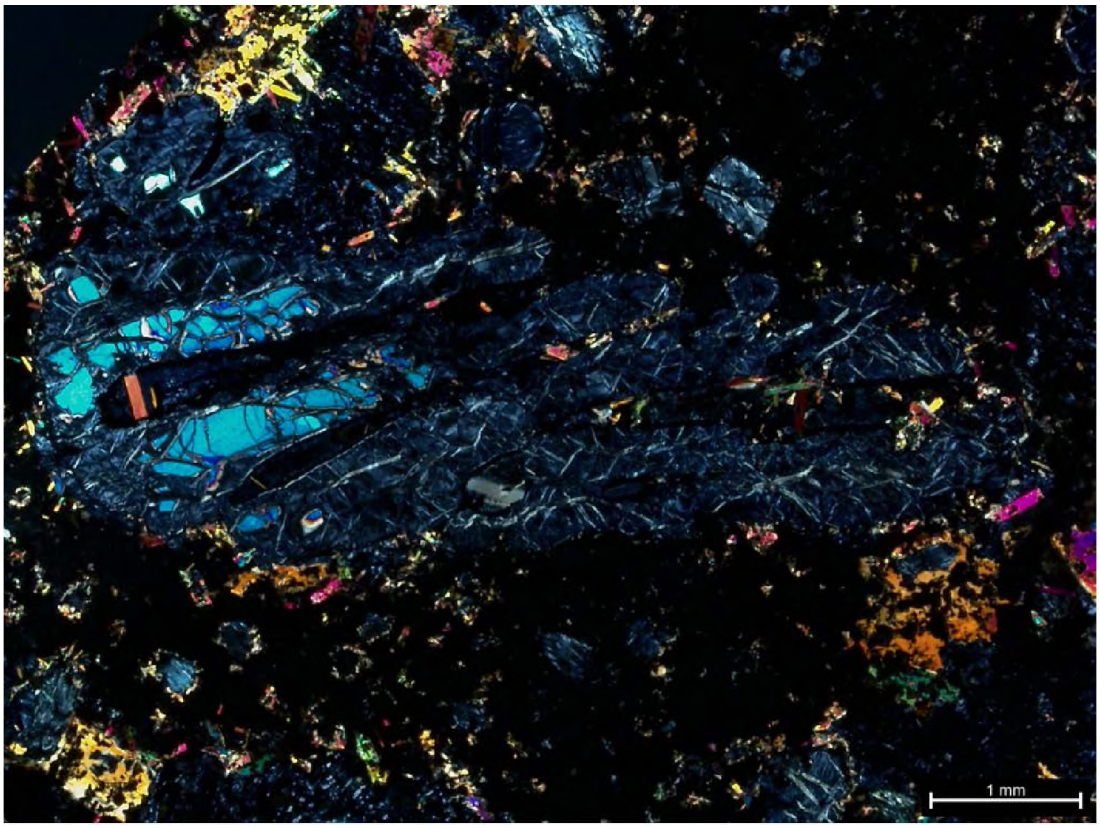

Figure A.42.: BHF-01-24-E.2 cross polarized light

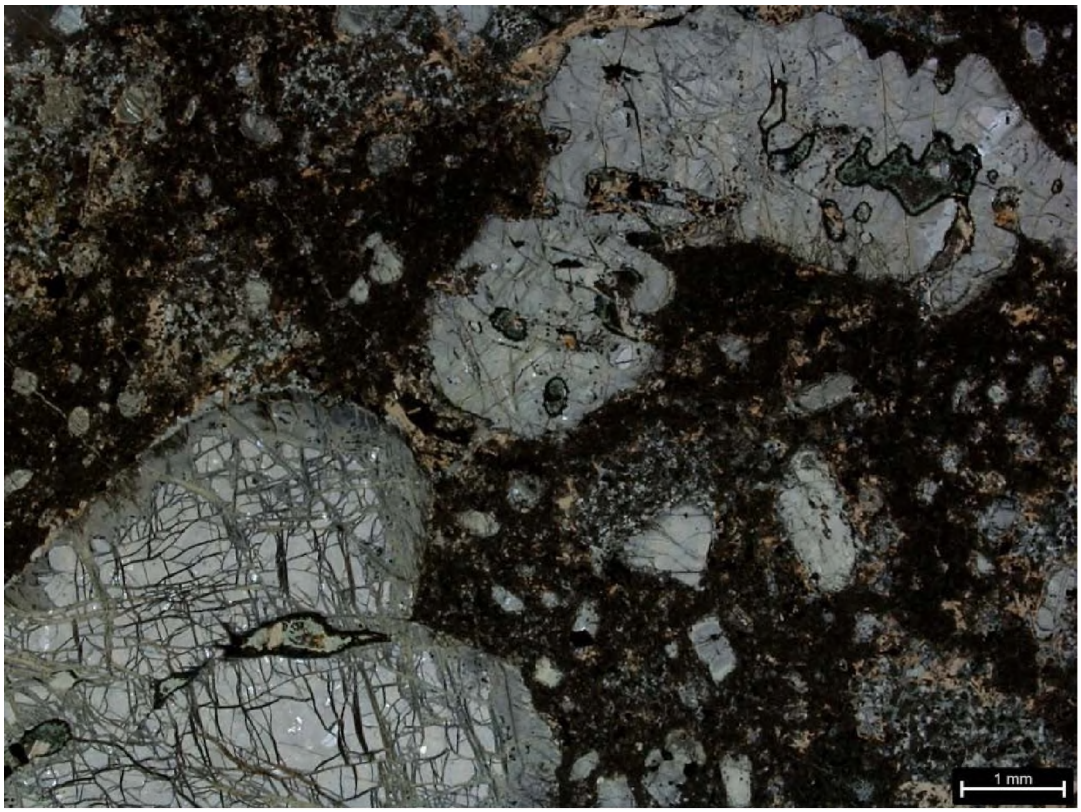

Figure A.43.: BHF-01-24-E.3 plane polarized light

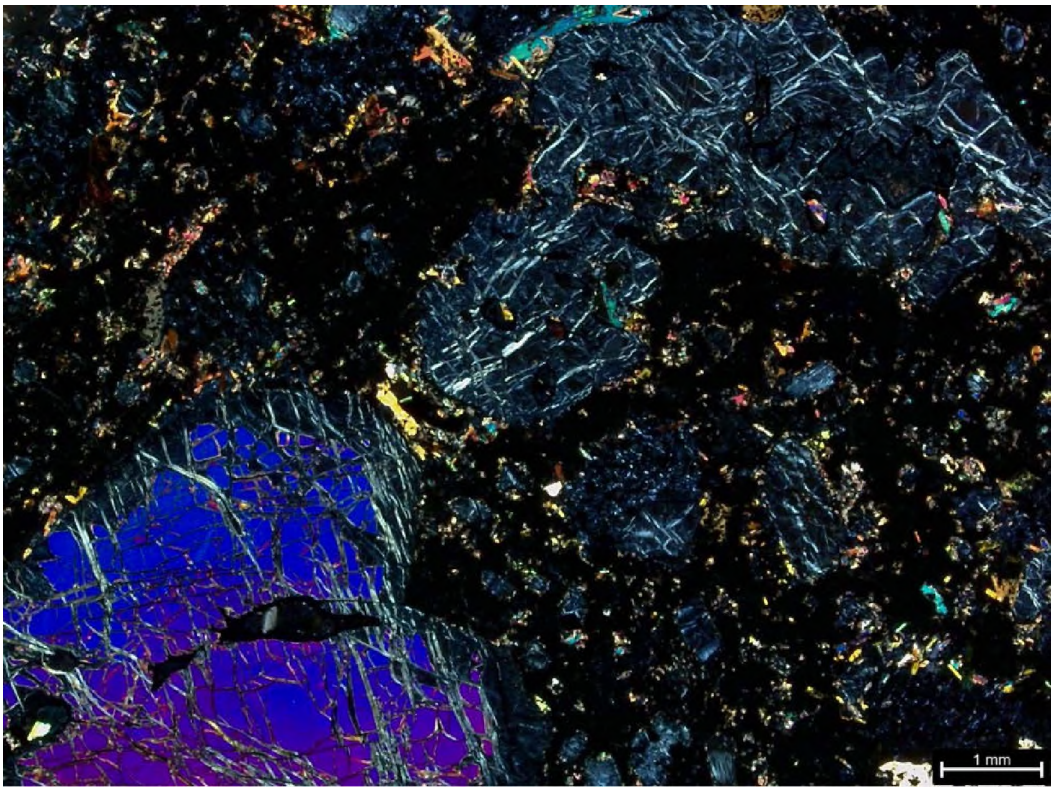

Figure A.44.: BHF-01-24-E.3 cross polarized light

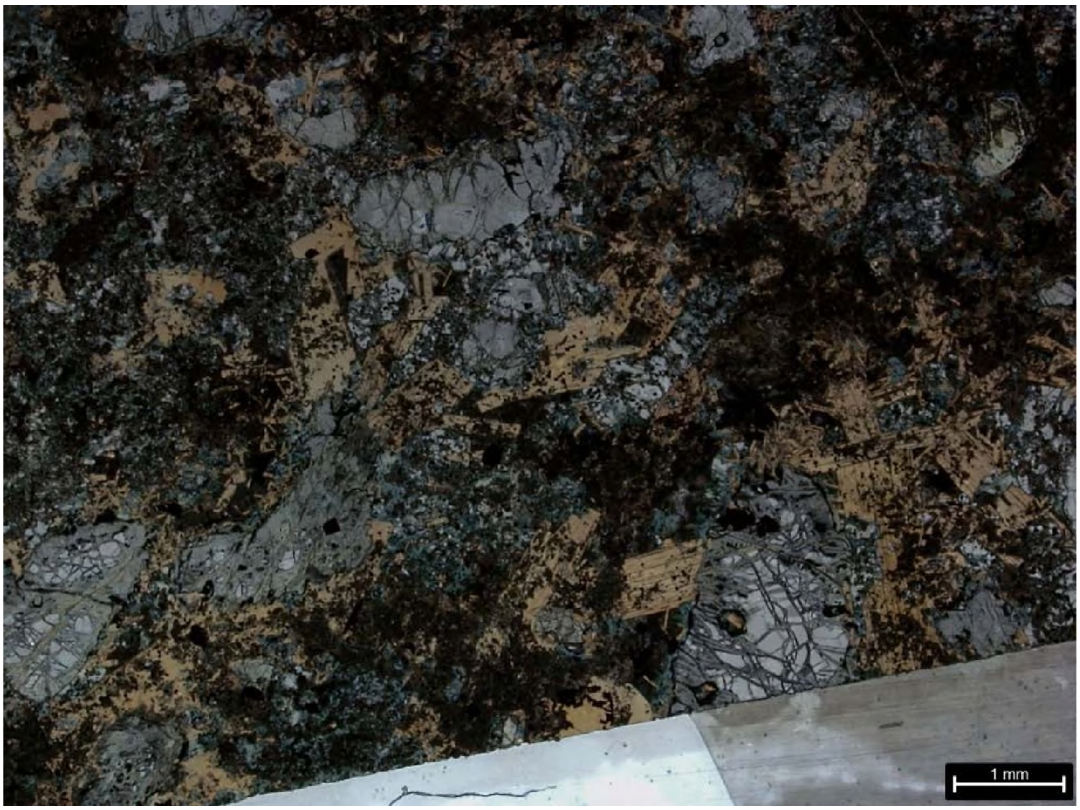

Figure A.45.: BHF-01-24-E.4 plane polarized light

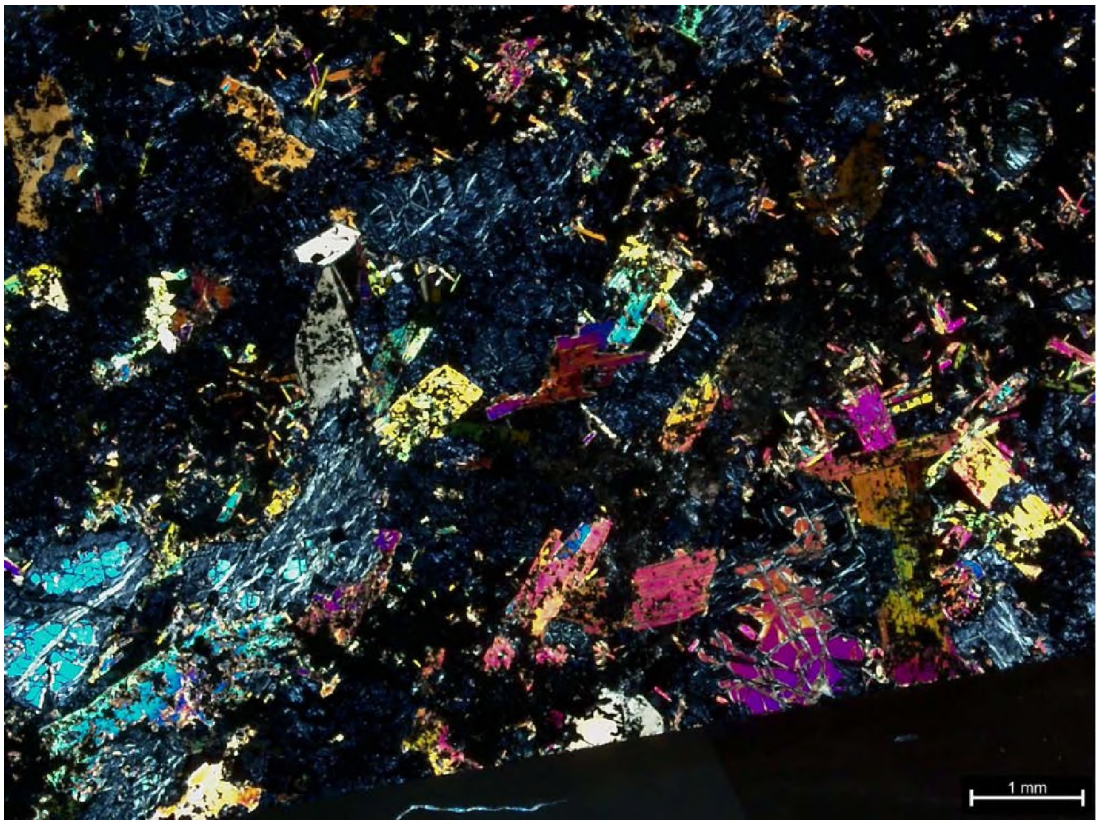

Figure A.46.: BHF-01-24-E.4 cross polarized light

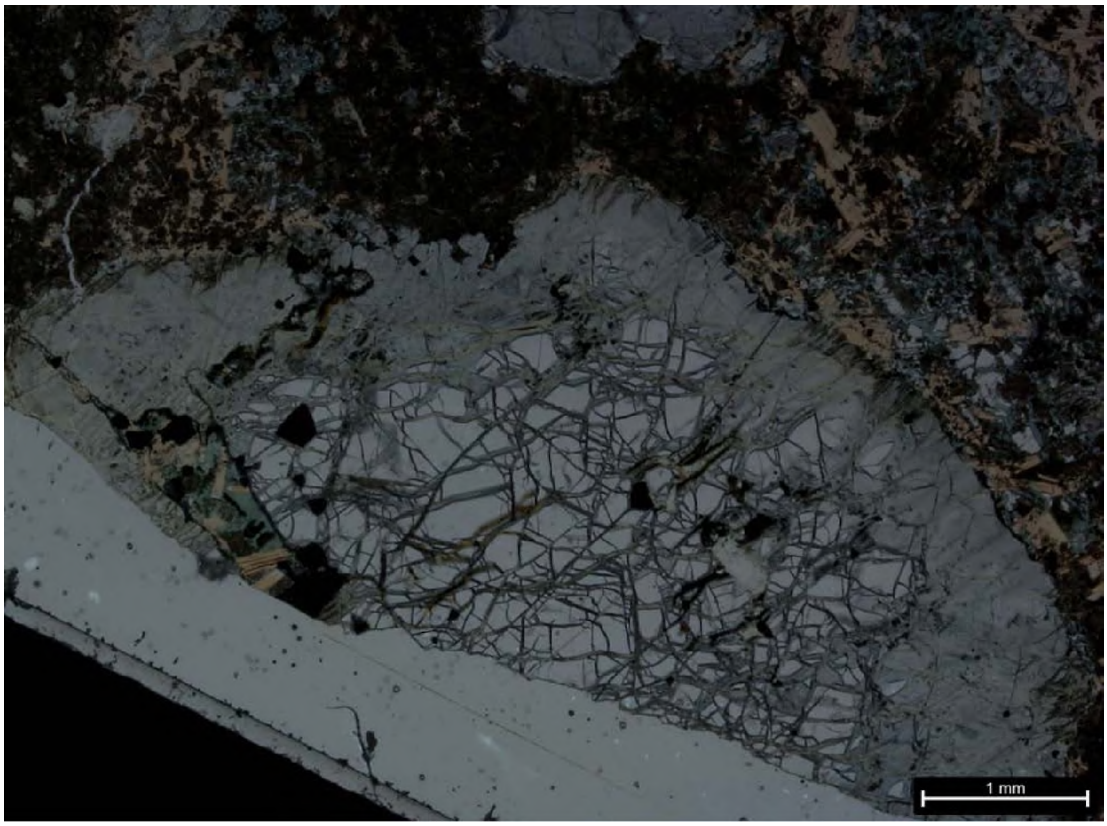

Figure A.47.: BHF-01-24-F.1 plane polarized light

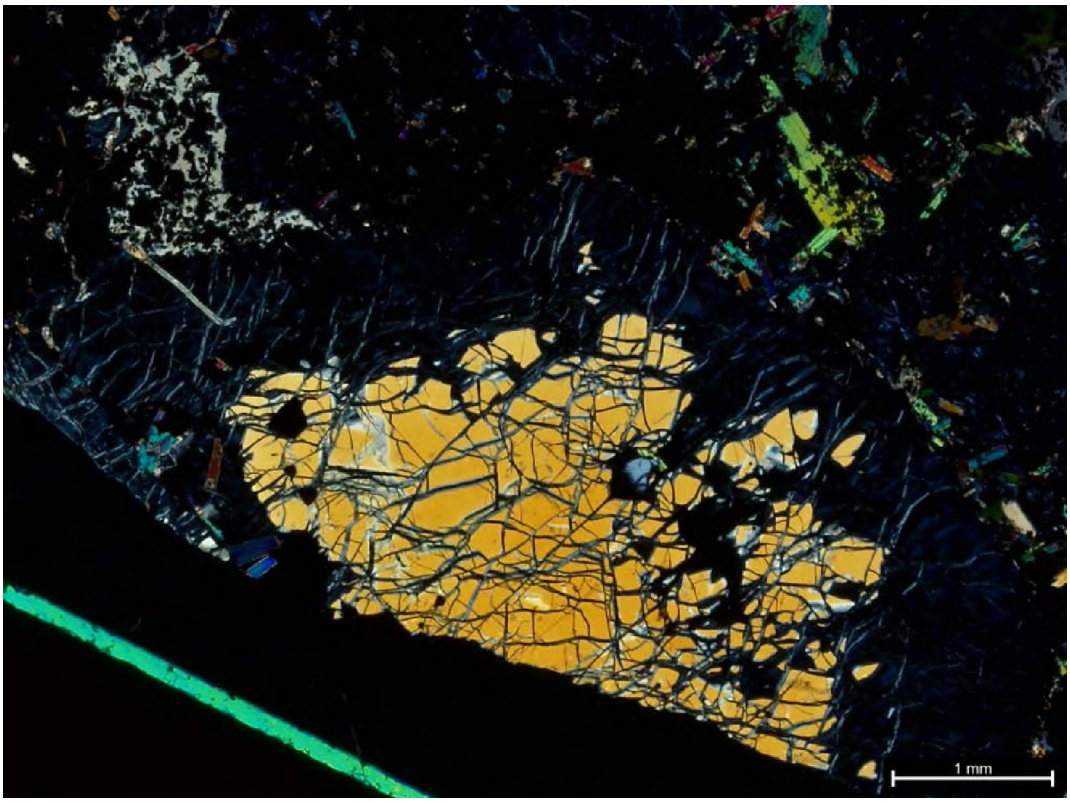

Figure A.48.: BHF-01-24-F.1 cross polarized light

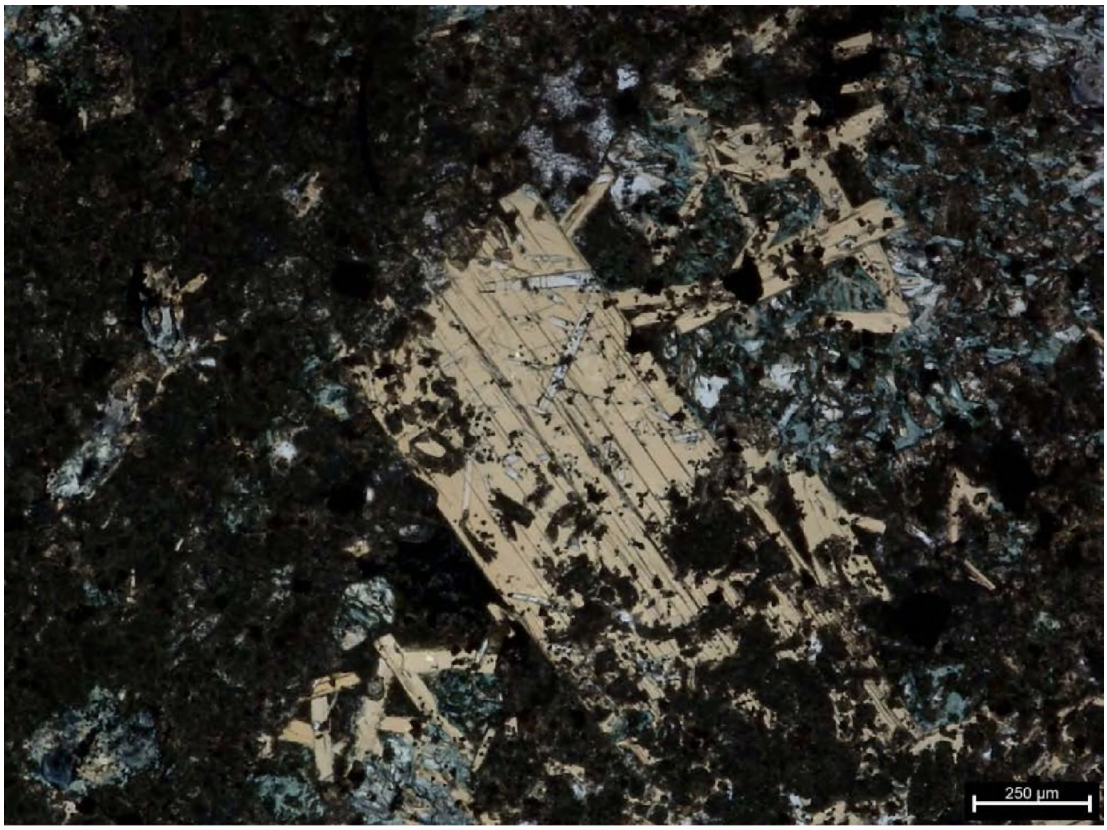

Figure A.49.: BHF-01-24-F.2 plane polarized light

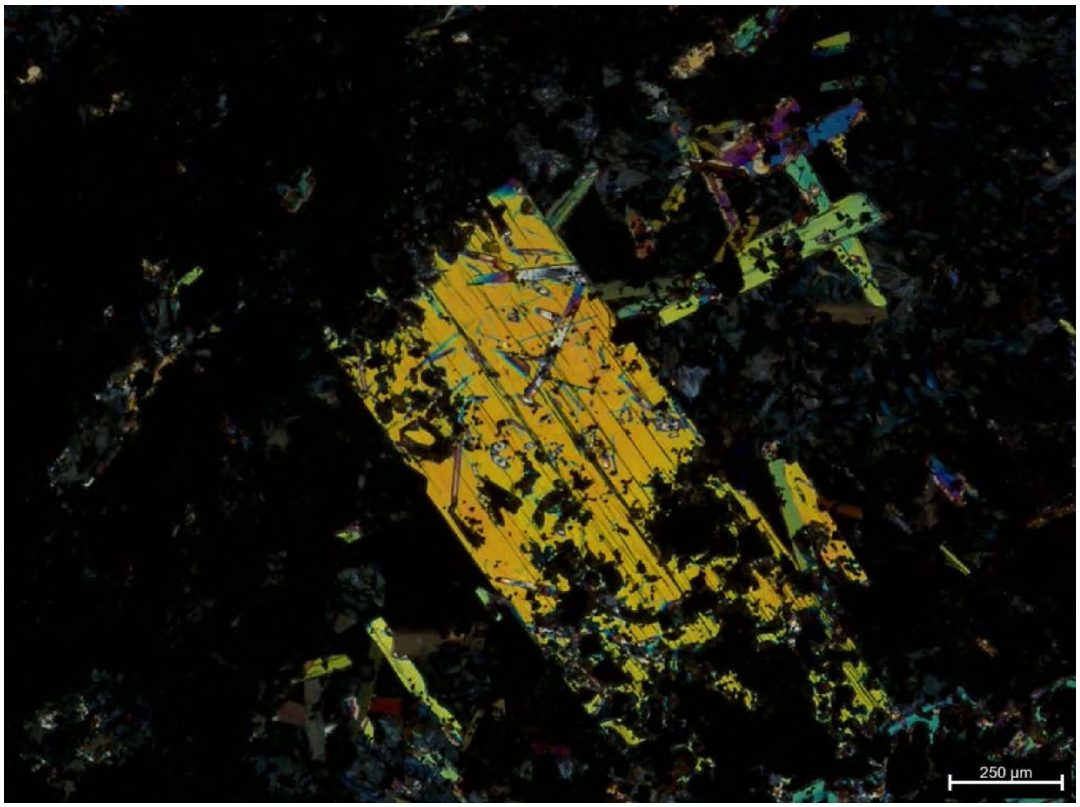

Figure A.50.: BHF-01-24-F.2 cross polarized light

Figure A.51.: BHF-01-24-F.3 plane polarized light

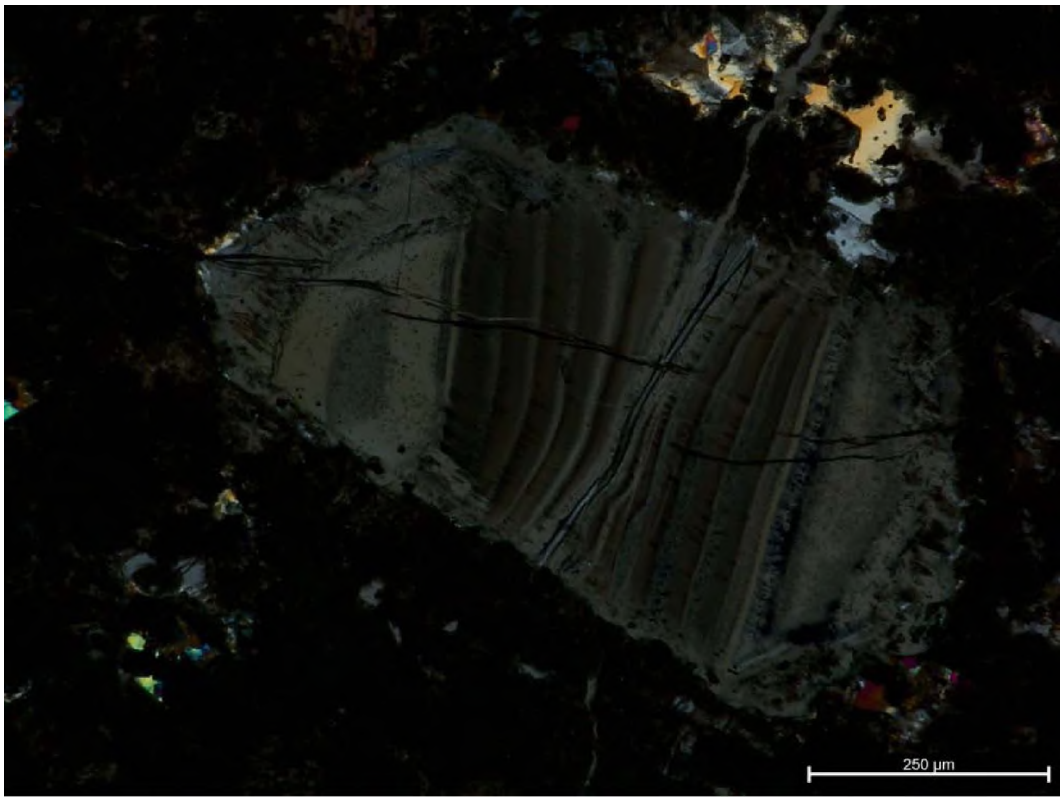

Figure A.52.: BHF-01-24-F.3 cross polarized light

APPENDIX B.

COMPREHENSIVE ELECTRON MICROPROBE ANALYSIS

Electron microscope parameters enabled for the precise collection of geochemical data and are outlined in Section 3 of the paper. Table B.1. details the standards used for each oxide analyzed in olivine and phlogopite mineral composition. Table B.2. shows the oxide abundances from a "Biotite 13" standard used as the primary standard for calibrating phlogopite EMPA data as well as abundances from a "Olivine 2566" standard used as the primary standard for calibrating olivine EMPA data. Figures B.1 and B.2 include backscatter electron images and elemental maps taken from the JEOL 8600 electron microprobe.

Table B.1.: Standards for each oxide used in EMPA

Oxide	**WDS Crystal**	**Standard(s)**
Na_2O	TAP	Amelia albite
MgO	TAP	Olivine 2566 (Forsterite)
Al_2O_3	TAP	Anorthite
SiO_2	TAP	Amelia albite for phlogopite analyses, olivine 2566 for olivine analyses
K_2O	PET	Microcline
TiO_2	PET	Ilmenite
CaO	PET	Anorthite for phlogopite analyses, wollastonite for olivine analyses
Cr_2O_3	PET	Chromite
FeO	LIF	Fayalite
MnO	LIF	P-130 garnet (alm-spe)
BaO	LIF	Barite
NiO	LIF	Nickel metal

Table B.2. Biotite 13 standard oxide abundance from EMPA (phlogopite)

Oxide (wt%)	Pt# 1	Pt# 2	Pt# 3	Pt# 4	Pt# 5	Pt# 6	Pt# 7	Pt# 8	Pt# 9
SiO_2	33.44	32.81	31.47	33.32	33.09	32.48	33.64	31.57	31.15
TiO_2	1.4139	1.3601	1.384	1.4975	1.3482	1.3228	1.3899	1.3951	1.4521
Al_2O_3	17.47	16.72	17.29	17.91	17.71	17.93	17.91	18.19	17.68
Cr_2O_3	b.d.l	b.d.l	b.d.l	b.d.l	b.d.l	b.d.l	b.d.l	b.d.l	b.d.l
FeO	31.45	31.24	32.11	32.53	31.55	30.84	31.94	31.99	32.47
MnO	0.0767	0.0329	0.0906	0.0164	0.0466	0.0684	0.0604	0	0
MgO	2.4631	2.7854	2.4695	2.854	2.7938	2.7987	2.7364	2.5536	2.7595
NiO	b.d.l	b.d.l	b.d.l	b.d.l	b.d.l	b.d.l	b.d.l	b.d.l	b.d.l
BaO	0.0846	0.124	0	0.1179	0.1521	0	0.0959	0.0281	0.0394
CaO	0.0367	0.0152	0.0328	0.0048	0.0143	0.0223	0.0287	0	0.0375
Na_2O	1.0989	0.272	0	0.118	0.224	0.0352	0.0473	0.0297	0.0894
K_2O	8.5842	8.5489	8.9492	9.1646	9.0183	8.9634	8.8537	8.531	8.9314
Total	**97.17**	**94.96**	**94.91**	**98.38**	**96.78**	**95.31**	**97.54**	**95.35**	**95.71**

Table B.3. Olivine 2566 standard oxide abundance from EMPA (olivine)

Oxide (wt%)	Pt# 1	Pt# 2	Pt# 3	Pt# 4	Pt# 5	Pt# 6	Pt# 7	Pt# 8	Pt# 9
SiO_2	40.17	39.53	40.35	40.05	38.54	40.77	39.35	37.32	38.35
TiO_2	0.0151	0	0.017	0.0387	0.0141	0.0113	0	0.018	0.0214
Al_2O_3	0	0	0.0447	0	0	0.0089	0.024	0	0.0864
Cr_2O_3	0.0298	0.0269	0.0203	0.0356	0.0225	0.0668	0.0553	0.0349	0.0478
FeO	17.03	17.21	16.95	17.29	17.05	17.2	17.27	17.27	17.13
MnO	0.3892	0.3741	0.3237	0.3125	0.3889	0.359	0.3766	0.2861	0.3584
MgO	43.48	43.17	43.61	43.31	43.4	43.48	43.86	42.65	43.58
NiO	0	0	0	0.0038	0	0.0339	0	0	0
BaO	b.d.l	b.d.l	b.d.l	b.d.l	b.d.l	b.d.l	b.d.l	b.d.l	b.d.l
CaO	0.0128	0.0271	0.0451	0.0023	0	0.0158	0.061	0	0
Na_2O	0.0288	0.029	0	0	0	0	0	0	0
K_2O	b.d.l	b.d.l	b.d.l	b.d.l	b.d.l	b.d.l	b.d.l	b.d.l	b.d.l
Total	**101.14**	**100.36**	**101.36**	**101.04**	**99.42**	**101.95**	**101**	**97.57**	**99.58**

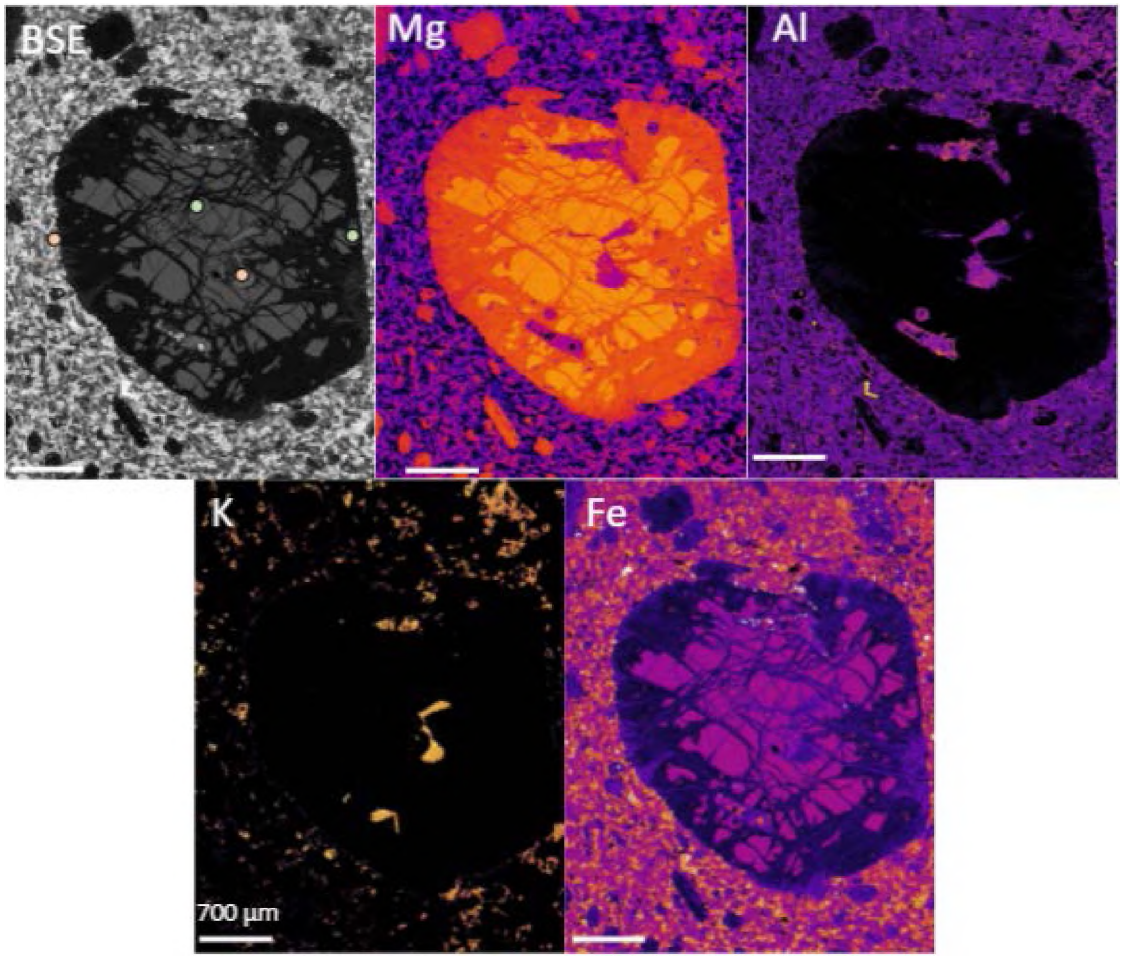

Figure B.1.: A backscatter electron image (BSE) detailing target points within an OM-I and major elemental maps (Mg, Al, K, Fe) of BHF-01-24-D.1 taken from the JEOL 8600 electron microprobe. The green circles in the BSE image indicate olivine target locations (core and rim). The pink circles in the BSE image indicate phlogopite target locations (phl-Ia, phl-Ib).

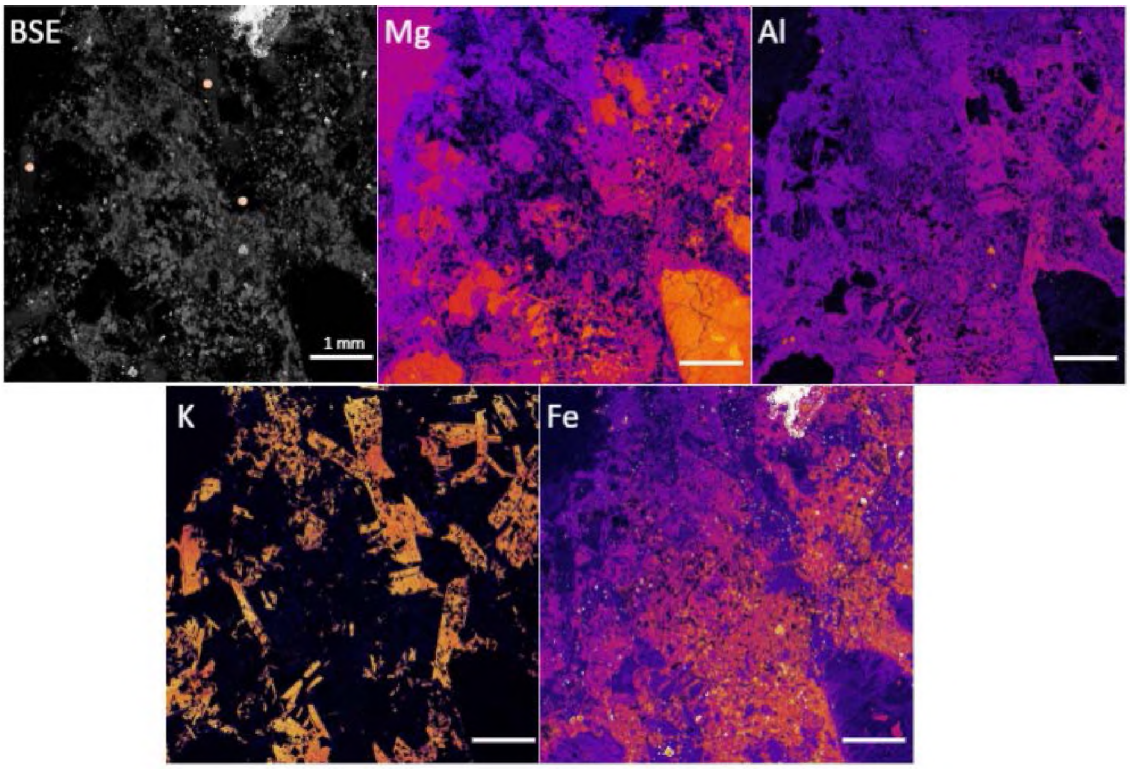

Figure B.2.: A backscatter electron image (BSE) detailing target points within phl-Ia and phl-II in matrix and major elemental maps (Mg, Al, K, Fe) of BHF-01-24-D matrix taken from the JEOL 8600 electron microprobe. The pink circles in the BSE image indicate phlogopite target locations (phl-Ia, phl-II).

APPENDIX C.

OLIVINE: ADDITIONAL COMPOSITION BIVARIATE PLOTS

Comparing elemental oxide concentrations through bivariate plots can be an effective way to visually show distinctions and similarities in the geochemical signatures of minerals, allowing for more in-depth analyses and interpretation of geologic phenomenon within the context of one or more geochemical systems. Included in this section are K-24 relict olivine geochemical bivariate plots not included in the main paper.

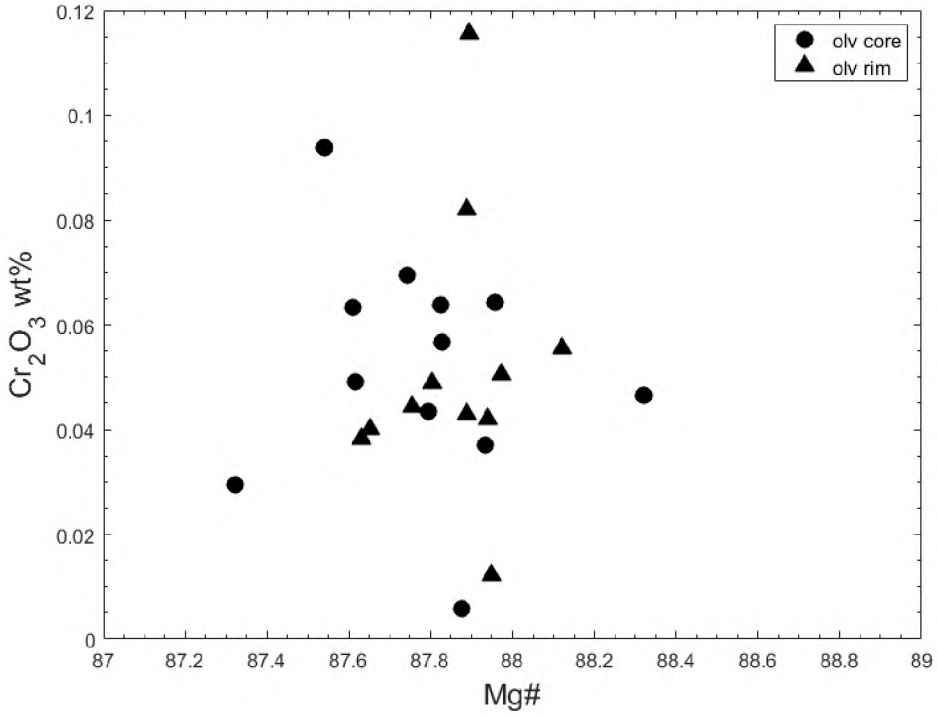

Figure C.1.: Olivine bivariate plot comparing Cr_2O_3 wt% to Mg#

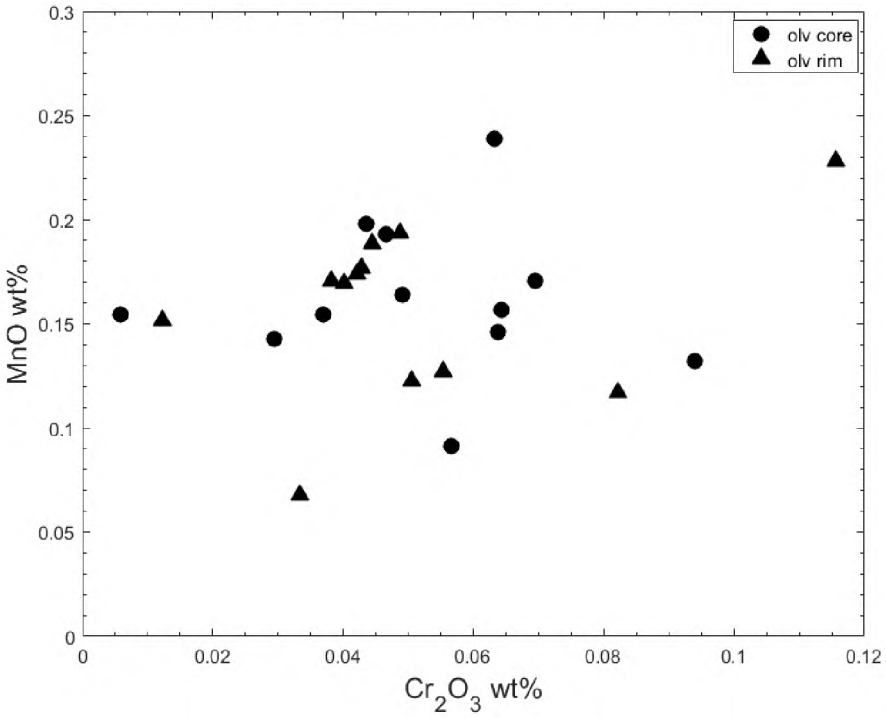

Figure C.2: Olivine bivariate plot comparing MnO wt% to Cr_2O_3 wt%

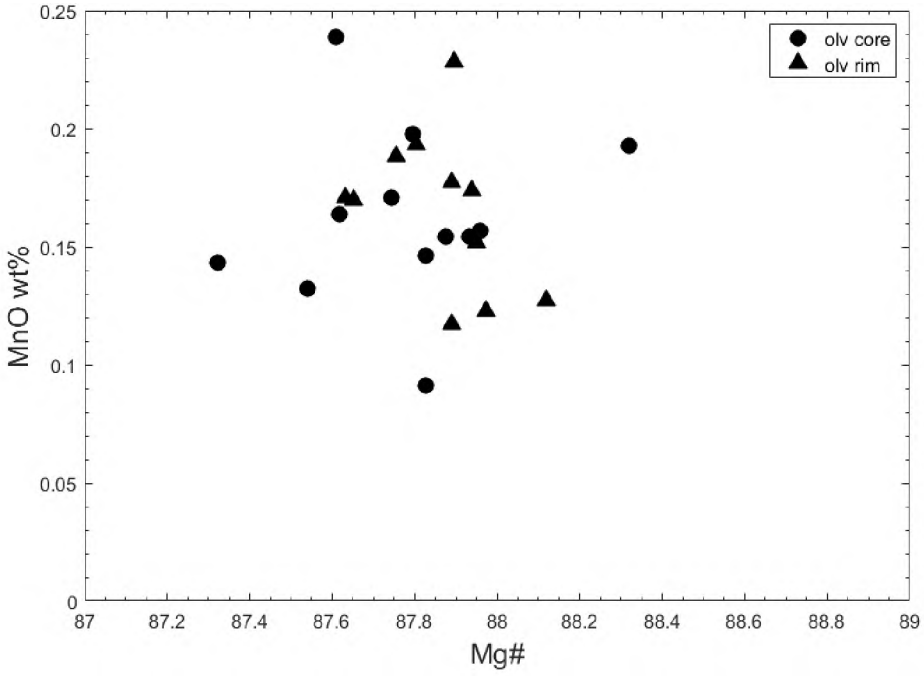

Figure C.3: Olivine bivariate plot comparing MnO wt% to Mg#

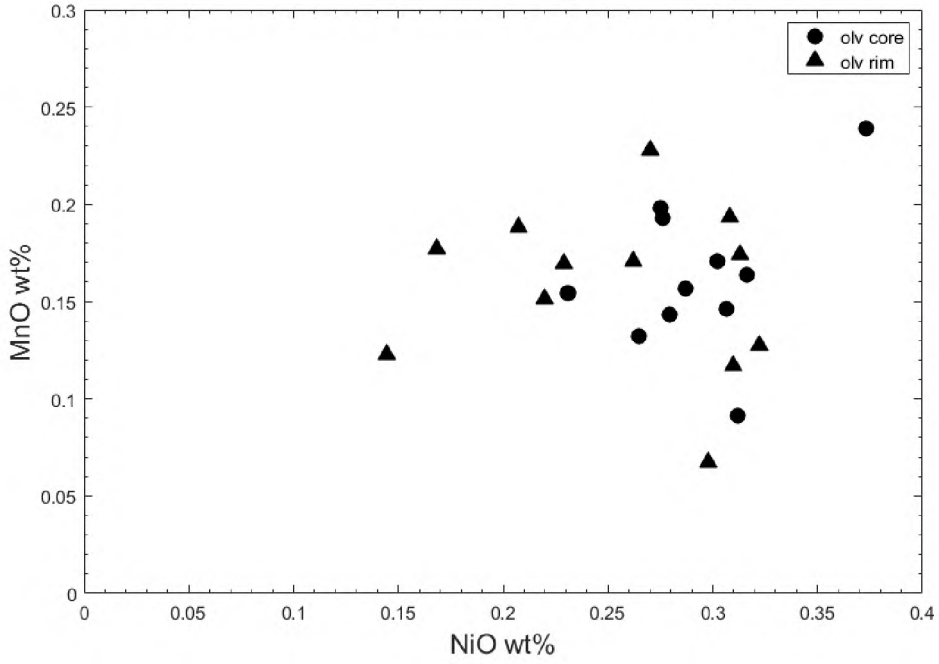

Figure C.4: Olivine bivariate plot comparing MnO wt% to NiO wt%

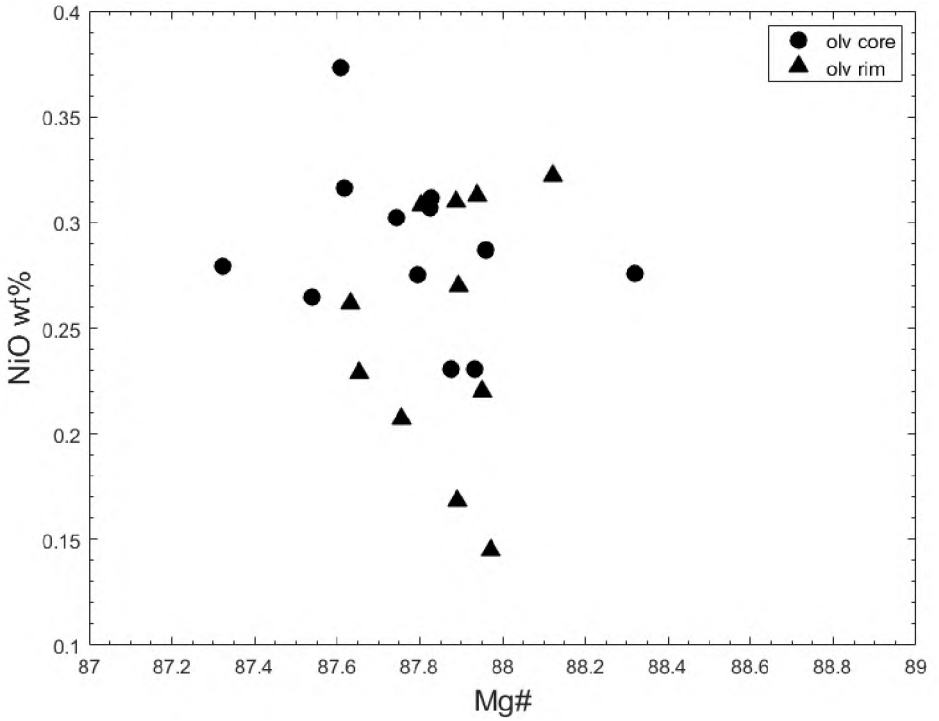

Figure C.5: Olivine bivariate plot comparing NiO wt% to Mg#

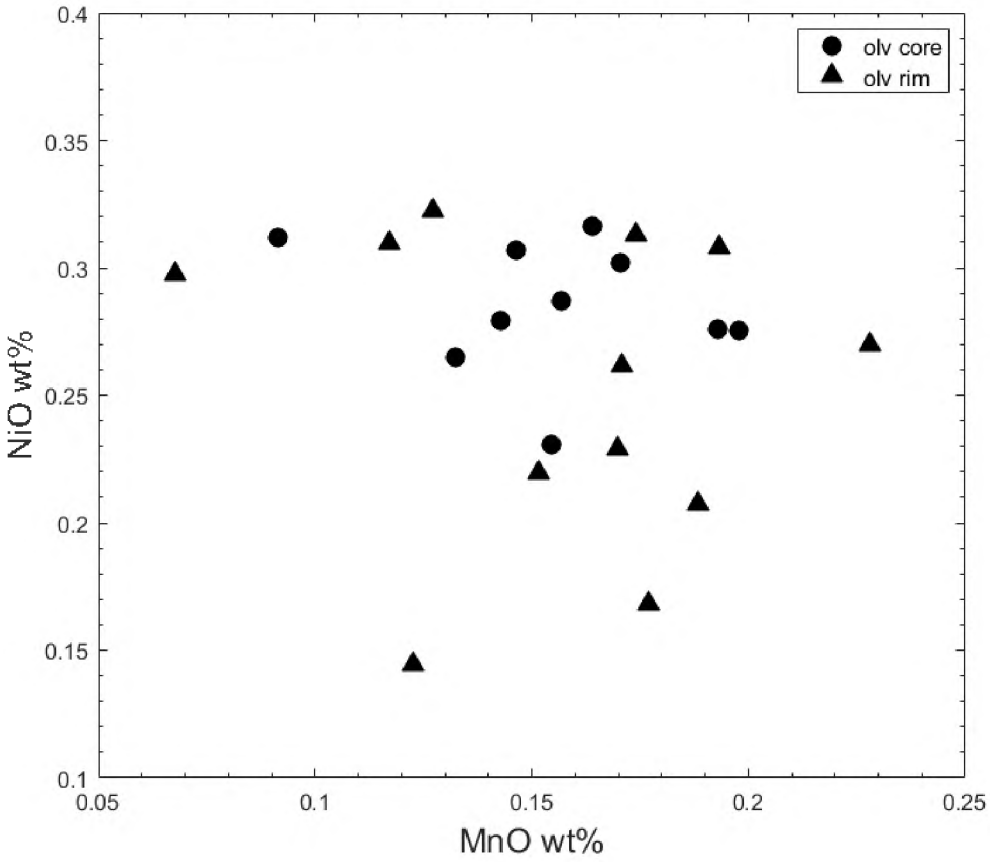

Figure C.6: Olivine bivariate plot comparing NiO wt% to MnO wt%

APPENDIX D.

PHLOGOPITE: ADDITIONAL COMPOSITION BIVARIATE PLOTS

Comparing oxide and atoms per fractional unit elemental abundances through bivariate plots can be an effective way to visually show distinctions and similarities in the geochemical signatures of minerals, allowing for more in-depth analyses and interpretation of geologic phenomenon within the context of one or more geochemical systems. Included in this section are K-24 phlogopite geochemical bivariate plots not included in the main paper.

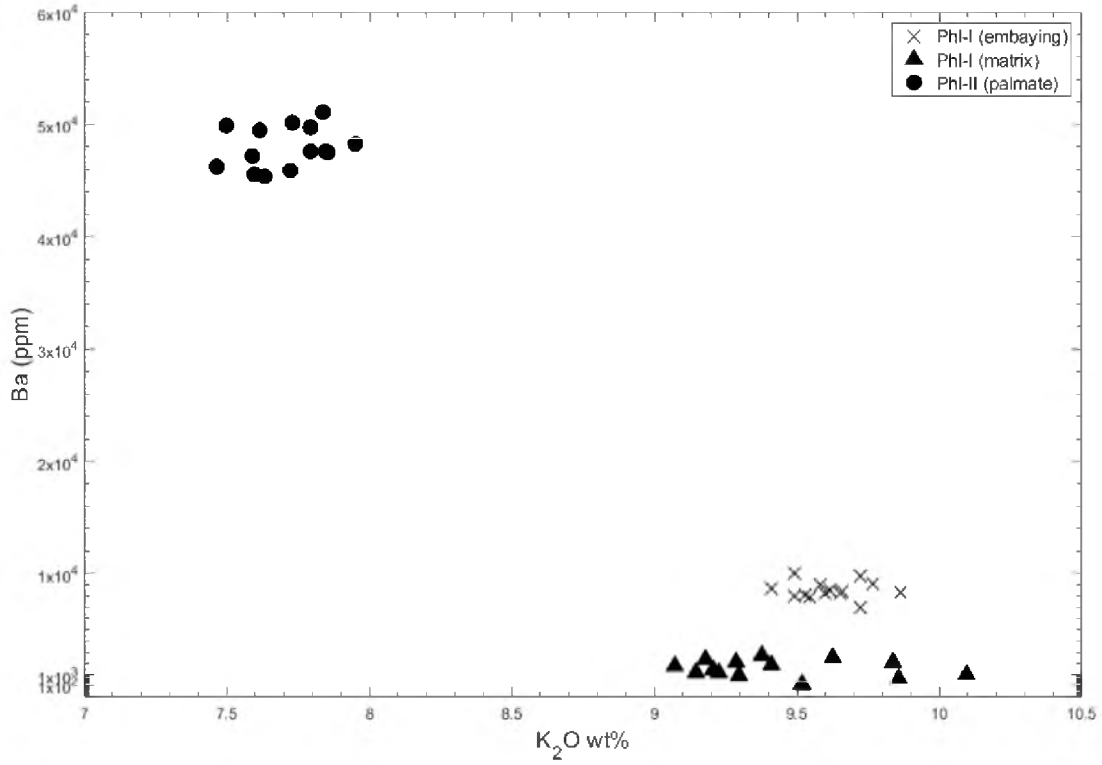

Figure D.1.: Phlogopite bivariate plot comparing Ba(ppm) to K_2O wt%

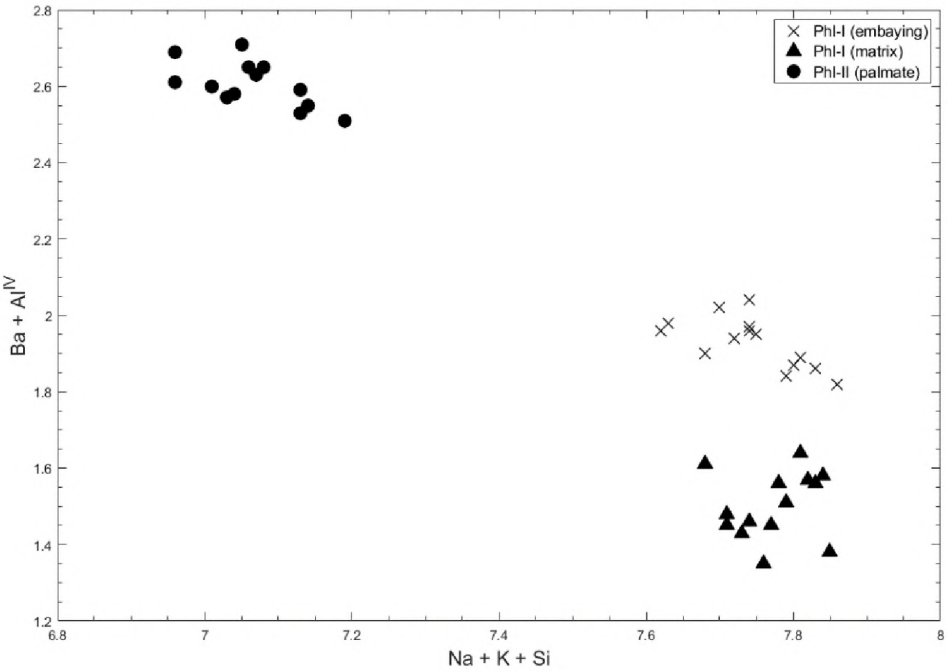

Figure D.2.: Phlogopite bivariate plot comparing enrichment ion substitution pairs ($Ba+Al^{IV}$ to Na+K+Si)

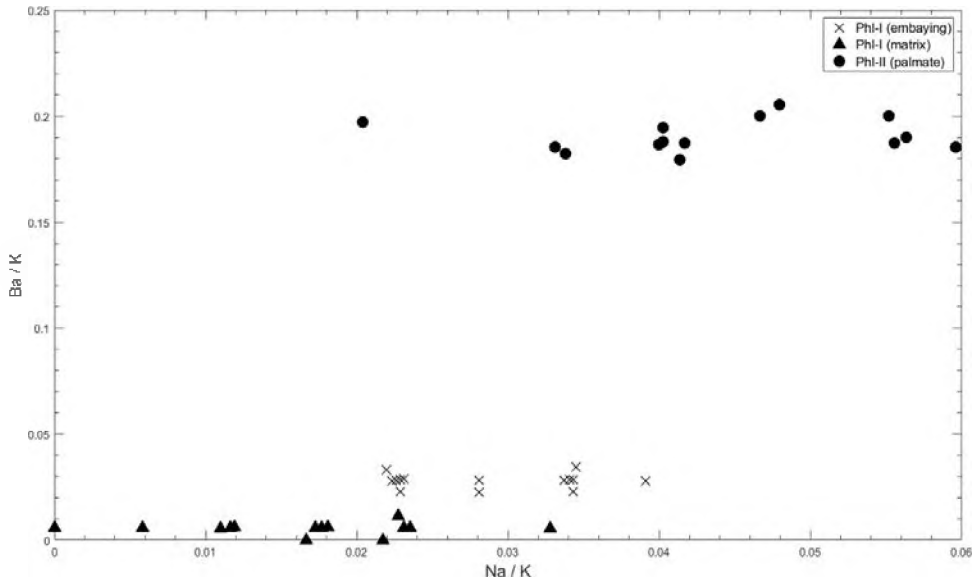

Figure D.3.: Phlogopite bivariate plot comparing Ba/K to Na/K

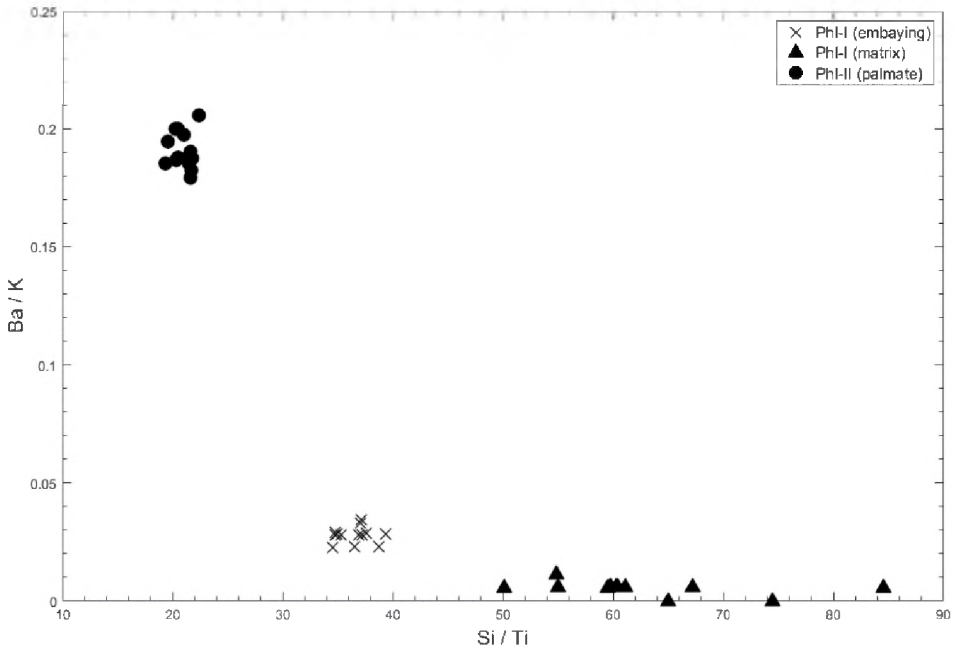

Figure D.4.: Phlogopite bivariate plot comparing Ba/K to Si/Ti

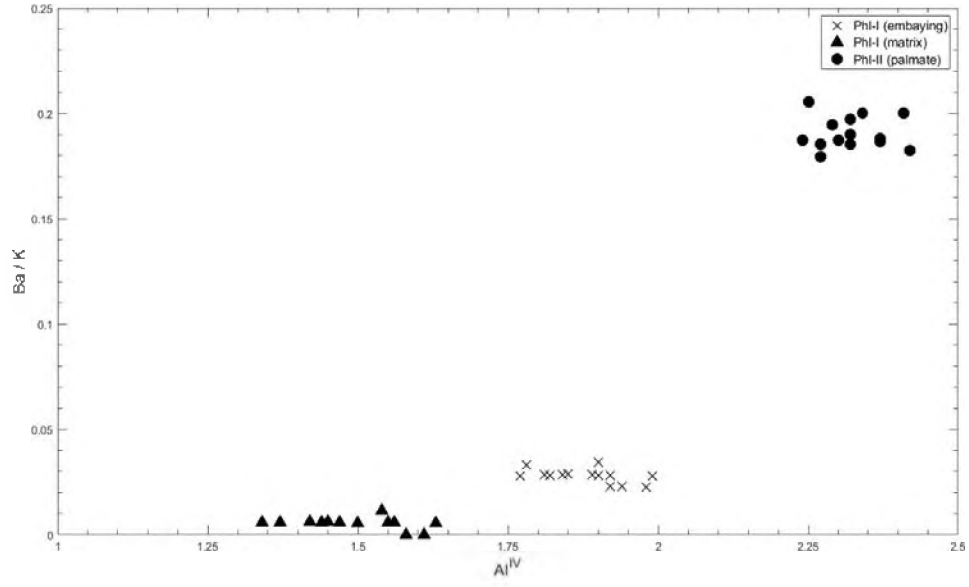

Figure D.5.: Phlogopite bivariate plot comparing Ba/K to Al^{IV}

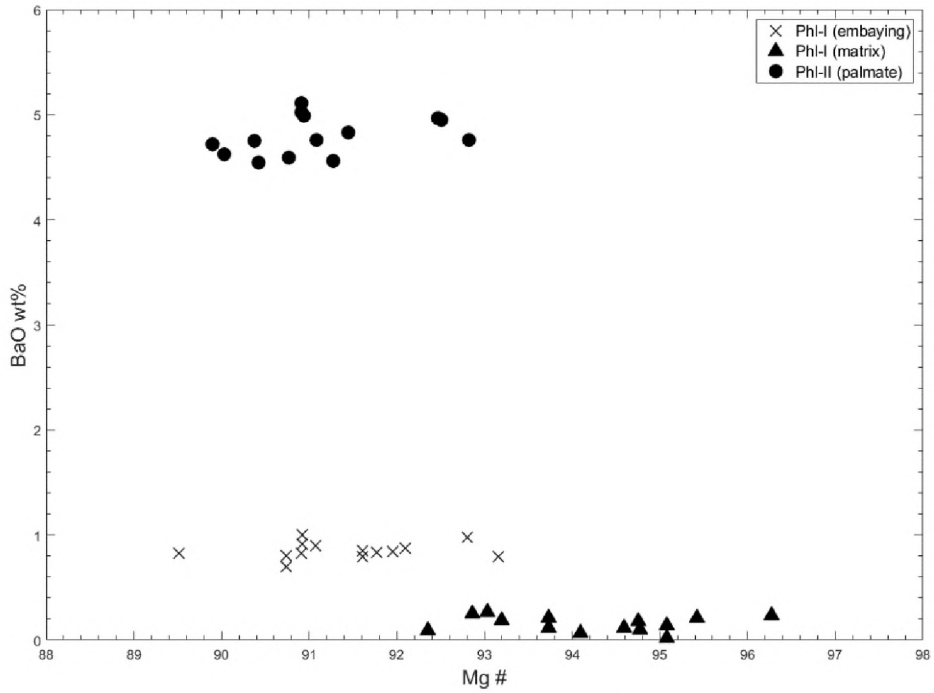

Figure D.6.: Phlogopite bivariate plot comparing BaO wt% to Mg#

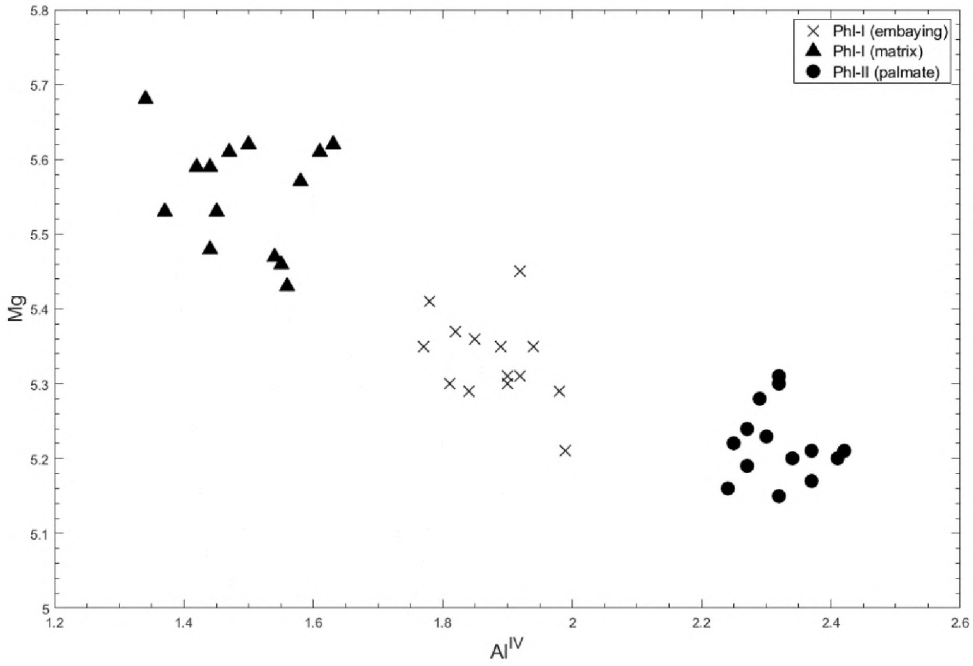

Figure D.7.: Phlogopite bivariate plot comparing Mg to Al^{IV}

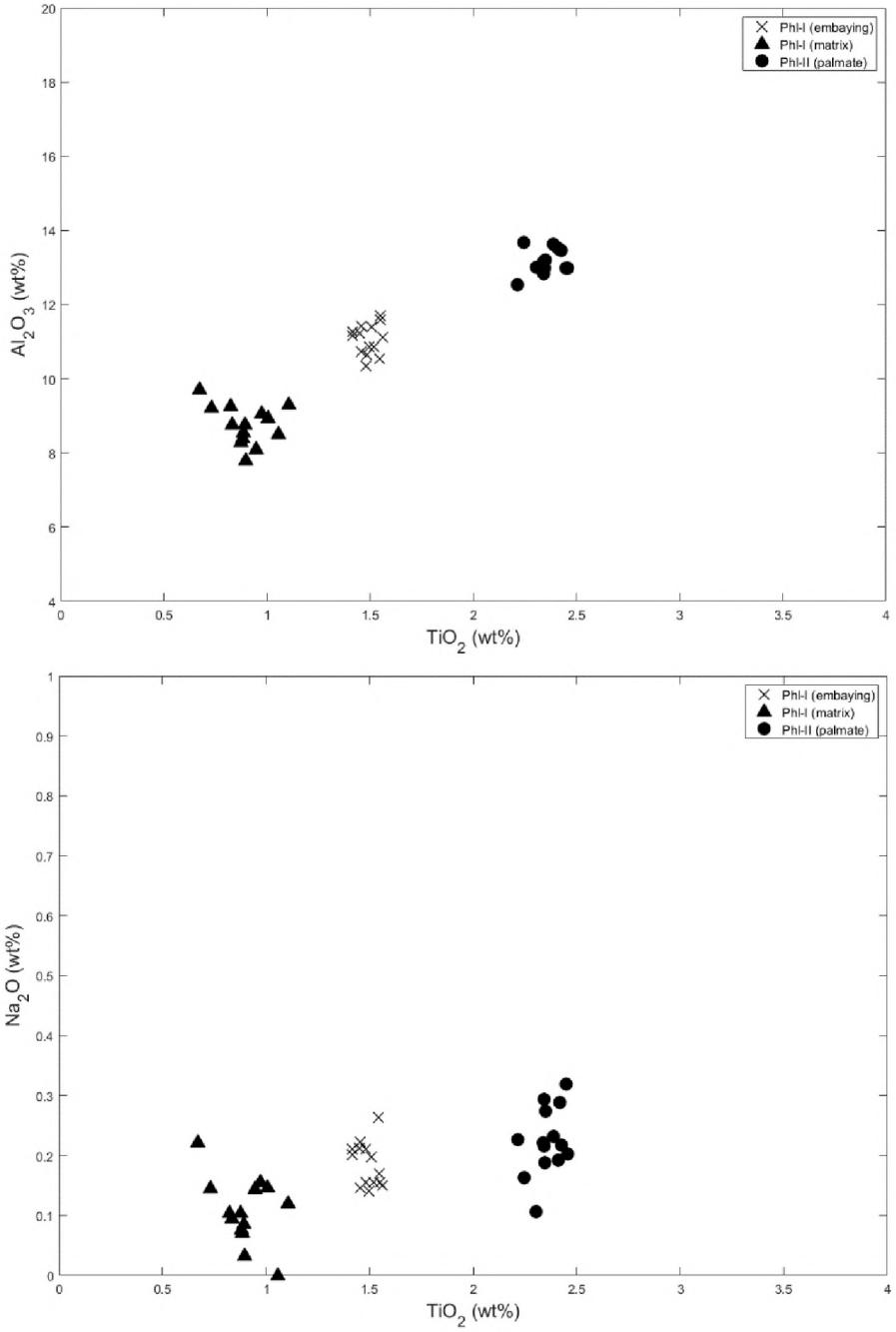

Figure D.8.: Phlogopite bivariate plot comparing TiO_2 wt% to Al_2O_3 wt% and Na_2O wt%

BIBLIOGRAPHY

Brooker, R.A., Kjarsgaard, B.A., 2011. Silicate-carbonate liquid immiscibility and phase relations in the system SiO2-Na2O-Al2O3-Cao-Co2 at 0.1-2.5 GPa with applications to carbonatite genesis. J. Petrol. 52, 1281–1305.

Currie, C.A., Beaumont, C., Are diamond-bearing Cretaceous kimberlites related to low-angle subduction beneath western North America? *Earth and Planetary Science Letters* (2011), 303, 1-2, pg. 59-70.

Freeman, Z.W., "Avon Alkaline Igneous Province, Missouri: Characterization of subcontinental mantle source and evolution via chemical analysis of olivine" (2016). Masters Theses. 7737.

Gernon, T.M., Brown, R.J., Tait, M.A., Hincks, T.K., The origin of pelletal lapilli in explosive kimberlite eruptions. Nat Commun 3, 832 (2012).

Kidwell, A. L. (1947), Post-Devonian Igneous Activity in Southeastern Missouri, edited by M. D. o. B. a. Administration, Jefferson City, MO

Kostrovitsky, S. I., *Physical Conditions, Hydraulics and Kinematics of Emplacement of Kimberlite Pipes* 1–95 (Nauka, Novosibirsk, 1976)

Lorenz, V., (2003) Maar-diatreme volcanoes, their formation, and their setting in hard-rock or soft-rock environments. Geolines 15, 72–83.

Mansker, W.L., 1973. Petrology of a Southeastern Missouri Ultramafic Pipe. University of Missouri.

Marshak, S., Paulsen, T., 1996; Midcontinent U.S. fault and fold zones: A legacy of Proterozoic intracratonic extensional tectonism?. *Geology* ; 24 (2): 151–154.

Menuge, J.F., Brewer, T.S., Seeger, C.M., Petrogenesis of metaluminous A-type rhyolites from the St Francois Mountains, Missouri and the Mesoproterozoic evolution of the southern Laurentian margin. (2002) Precambrian Research. vol. 113, 3-4. pg 269-291.

Mitchell, R.H., Kimberlites: Mineralogy, Geochemistry, and Petrology. Plenum Press, London & New York (1986).

Morgavi D., Arienzo I., Montagna C., Perugini D., Dingwell D.B. (2017) Magma Mixing: History and Dynamics of an Eruption Trigger. In: Gottsmann J., Neuberg J., Scheu B. (eds) Volcanic Unrest. Advances in Volcanology. Springer, Cham. ISBN: 978-3-319-58412-6

Murphy, J. & Keppie, John. (2005). The Acadian Orogeny in the Northern Appalachians. International Geology Review. 47. 663-687.

Potter, N.J., Kamenetsky, V.S., Simonetti, A., Goemann, K., Different types of liquid immiscibility in carbonatite magmas: A case study of the Oldoinyo Lengai 1993 lava and melt inclusions. *Chemical Geology* (2017), 455, 376-384

Russell, J.K., Porritt, L.A., Lavallée,Y., Dingwell, D.B., Kimberlite ascent by assimilation-fuelled buoyancy. Nature, 481 (7381) (2012), pp. 352-356

Singewald, J. T., and Milton, C., 1930, An alnöite pipe, its contact phenomena, and ore deposition near Avon, Missouri: The Journal of Geology, vol. 38, p. 54-66

Shavers, E.J., Ghulam, A., Encarnacion, J., Bridges, D.L., Luetkemeyer, P.B., Carbonatite associated with ultramafic diatremes in the Avon Volcanic District, Missouri, USA: Field, petrographic, and geochemical constraints (2016) Lithos, 248-251, pp. 506-516.

Shavers, E.J., Ghulam, A., Hartling, S., Emplacement of ultramafic-carbonatite intrusions along reactivated North American mid-continent rift structures (2017) Tectonophysics, 712-713

Sparks, R.S.J., Kimberlite Volcanism. *Annual Review of Earth and Planetary Sciences* (2013), Vol. 41:497-528

Wilson, L., Head III, J. An integrated model of kimberlite ascent and eruption. *Nature* 447, 53–57 (2007).

Zartman, R.R., Brock, M.R., Heyl, A.V., and Thomas H.H., K-Ar and Rb-Sr ages of some Alkalic Intrusive Rocks from the Central and Eastern United States. American Journal of Science, 1967, 265 (10) 848-870

VITA

Nathan Gregory Limbaugh graduated from the Missouri University of Science and Technology in Rolla, MO with a Bachelor of Science in Geology and Geophysics with an emphasis in geochemistry in May 2020. During his undergraduate career, Nathan was active in leadership positions in Student Council, Delta Sigma Phi fraternity, and served as president of Sigma Gamma Epsilon during their re-charter in 2019. Nathan was involved in undergraduate research and was awarded the Mines & Metallurgy Academy Scholar Award in 2020. Nathan received his Master of Science degree in Geology and Geophysics from the Missouri University of Science and Technology in July 2021. Starting in the fall of 2021, Nathan began the pursuit of a PhD in meteorite geology and geochemistry at the University of Alabama in Tuscaloosa, AL.